LEGIBILITY NOTICE

A major purpose of the Technical Information Center is to provide the broadest dissemination possible of information contained in DOE's Research and Development Reports to business, industry, the academic community, and federal, state and local governments.

Although a small portion of this report is not reproducible, it is being made available to expedite the availability of information on the research discussed herein.

1

ORNL/M--890

DE89 016457

Engineering Technology Division

HIGH-TEMPERATURE FLAW ASSESSMENT PROCEDURE

INTERIM REPORT

M. B. Ruggles
Oak Ridge National Laboratory

Y. Takahashi
Central Research Institute of Electric Power Industry

R. A. Ainsworth
Central Electricity Generating Board

Date Published - August 1989

NOTICE: This document contains information of a preliminary nature. It is subject to revision or correction and therefore does not represent a final report.

Prepared for the
Electric Power Research Institute
[Research Project 2658-21 (DOE-ERD-86-586)]
As a part of the
Liquid Metal Fast Breeder Reactor EPRI/CRIEPI/CEGB Joint Study
on High-Temperature Flaw Assessment Procedure

Prepared by the
OAK RIDGE NATIONAL LABORATORY
Oak Ridge, Tennessee 37831-6285
operated by
MARTIN MARIETTA ENERGY SYSTEMS, INC.
for the
U.S. DEPARTMENT OF ENERGY
under contract DE-AC05-84OR21400

CONTENTS

		Page
1.	INTRODUCTION	1
2.	AUXILIARY FUNDAMENTAL TESTS (CRIEPI/CEGB)	1
	2.1 INVESTIGATION OF BASIC STRESS-STRAIN CHARACTERISTICS - CRIEPI	1
	2.1.1 CYCLIC DEFORMATION TESTS	1
	2.1.2 CREEP DEFORMATION TESTS	2
	2.2 FUNDAMENTAL CRACK GROWTH EXPERIMENTS	2
	2.2.1 CYCLIC DISPLACEMENT DATA FOR TYPE 321 STAINLESS STEEL — CEGB	2
	2.2.2 CONSTANT LOAD DATA FOR TYPE 316 STAINLESS STEEL — CEGB	3
	2.2.3 TYPE 316 STAINLESS STEEL CREEP-FATIGUE CRACK GROWTH DATA — CEGB	3
	2.2.4 TYPE 304 STAINLESS STEEL CYCLIC CRACK GROWTH TESTS — CRIEPI	4
	2.2.5 TYPE 304 STAINLESS STEEL CREEP CRACK GROWTH TESTS — CRIEPI	5
3.	SUBCRITICAL CRACK GROWTH. EXPLORATORY TESTS	6
	3.1 CREEP-FATIGUE CRACK GROWTH TESTS UNDER MECHANICAL LOADING — CRIEPI	6
	3.1.1 THROUGH-WALL CRACK GROWTH TESTS	6
	3.1.2 SURFACE CRACK GROWTH TESTS	7
	3.2 CREEP-FATIGUE CRACK GROWTH TESTS UNDER REPEATED THERMAL TRANSIENT CONDITIONS — EPRI/CRIEPI	8
	3.2.1 THERMAL SHOCK TESTS OF PREFLAWED THICK-WALLED CYLINDERS — EPRI	8
	3.2.2 THERMAL SHOCK TESTS OF PREFLAWED CYLINDERS — CRIEPI	8
	3.3 CREEP-FATIGUE CRACK GROWTH TESTS UNDER DISPLACEMENT CONTROLLED CYCLING — CEGB	9
	3.3.1 METALLOGRAPHY	10
	3.3.2 CYCLIC LOAD-DISPLACEMENT BEHAVIOR	11
	3.3.3 CREEP-FATIGUE ENDURANCE CURVES	11
	3.3.4 CRACK GROWTH CORRELATIONS	12
	3.3.5 ANALYSIS PROCEDURE	12
	3.3.6 CREEP-FATIGUE CRACK GROWTH	14
	3.3.7 INITIAL LOAD	15
	3.3.8 LOAD RELAXATION	16
	3.3.9 ANALYTICAL RESULTS FOR LIFETIME AND CYCLIC RESPONSE	16

CONTENTS (Continued)

		Page
4.	SUBCRITICAL CRACK GROWTH MODELING	16
4.1	IDENTIFICATION OF THE POTENTIAL CREEP-FATIGUE CRACK GROWTH MODEL — CRIEPI/CEGB	16
4.1.1	SIMPLIFIED METHODS — CEGB	16
4.1.2	CYCLIC CRACK GROWTH MODELING — CRIEPI	20
4.1.3	CREEP-FATIGUE CRACK GROWTH MODELING — CRIEPI	22
4.1.4	FINITE ELEMENT ANALYSES OF SIMPLE GEOMETRIES — CEGB	23
4.1.5	FINITE ELEMENT ANALYSIS OF SURFACE CRACK GROWTH — CRIEPI	25
5.	EXPLORATORY FAILURE TESTS — EPRI	26
5.1	INTERNAL PRESSURIZATION TESTS OF PREFLAWED PIPES — EPRI	26
5.2	THERMAL SHOCK TESTS OF PREFLAWED THIN-WALLED CYLINDERS — EPRI	26
	REFERENCES	27
	TABLES	30
	FIGURES	34

1. INTRODUCTION

The current program represents a joint effort between the Electric Power Research Institute (EPRI) in the USA, the Central Research Institute of Electric Power Industry (CRIEPI) in Japan, and the Central Electricity Generating Board (CEGB) in the UK. The goal is to develop an interim high-temperature flaw assessment procedure for high-temperature reactor components. This is to be accomplished through exploratory experimental and analytical studies of high-temperature crack growth. The state-of-the-art assessment and the fracture mechanics database for both types 304 and 316 stainless steels, completed in 1988, serve as a foundation for the present work.

Work in the three participating organizations is progressing roughly on schedule. Results to-date are presented below. Fundamental test results are discussed in Section 2. Section 3 focuses on results of exploratory subcritical crack growth tests. Progress in subcritical crack growth modeling is reported in Section 4. Exploratory failure tests are outlined in Section 5.

2. AUXILIARY FUNDAMENTAL TESTS (CRIEPI/CEGB)

2.1 INVESTIGATION OF BASIC STRESS-STRAIN CHARACTERISTICS — CRIEPI

The objective of this task is to study the fundamental deformation characteristics of the test material. The material was austenitic type 304 stainless steel, annealed at 1,100°C for 30 min. Basic material properties are given in Table 1.

2.1.1 Cyclic Deformation Tests

Cyclic deformation tests were conducted using tensile specimens (10 mm in diameter in the gauge section) at 200, 400, 550, and 650°C. Experimental strain range step-up procedure is schematically shown in Fig. 1. A summary of tests is presented in Table 2. Specimens were subjected to axial strain-controlled cyclic loading with the strain rate of 10^{-3} s^{-1} and zero mean strain. The stress range ultimately attained for each strain range was used to construct a cyclic stress-strain curve. The stress range — strain range curves for the four temperatures under consideration are plotted in Fig. 2. Also given in Fig. 2 are the Ramberg-Osgood (R-O) type approximations of the experimental data at each temperature. Large cyclic hardening can be observed, particularly in the intermediate temperature range.

2.1.2 Creep Deformation Tests

Creep deformation tests, conducted at four different constant stress levels at 550 and 650°C, are summarized in Table 3. Variations of creep strain with time at 550 and 650°C are given in Figs. 3 and 4, respectively. Predictions obtained with the EPICC creep equation (with the coefficient a_r fitted to the test data) are plotted in Figs. 3 and 4 as well. Calculated and experimental results agree fairly well. Results presented here are expected to aid in evaluating the creep-fatigue crack growth data.

2.2 FUNDAMENTAL CRACK GROWTH EXPERIMENTS — CRIEPI/CEGB

2.2.1 Cyclic Displacement Data for Type 321 Stainless Steel — CEGB

Creep-fatigue crack growth data have been produced for both base and simulated HAZ type 321 stainless steel at 650°C in air and reported by Gladwin et al[1]. Prior to testing, the type 321 stainless steel was aged for 200 h at 750°C. Further heat treatment was used to produce simulated HAZ material. Following heat treatment, compact tension specimens of two thicknesses (12.5 mm and 12 mm) were machined from the plate material. Pure fatigue, fully reversed displacement-controlled tests with constant displacement tensile hold periods, and constant load tests were performed. Detailed measurements of load and crack length during each cycle were made so that the total crack growth could be separated into cyclic and hold period (creep) components.

The crack growth rate data are correlated in Fig. 5 with the values of C^* deduced from the experimentally measured rates of load drop during the hold periods. Also included in Fig. 5 are data from the constant load tests. It can be seen that there is some scatter in the data. However, no systematic difference between the base material and the simulated HAZ, or between the cyclic and static data was observed. The data can be fitted by the equation

$$\dot{a} = 0.005(C^*)^{0.9} , \tag{1}$$

where $\dot{a}$ is measured in mh^{-1} and C^* is measured in $MPa\text{-}mh^{-1}$. This equation is in reasonable agreement with data presented by Ohtani et al[2] on type 321 stainless steel at ˀ50°C and 700°C, as noted by Gladwin et al[1].

2.2.2 Constant Load Data for Type 316 Stainless Steel — CEGB

Tests on solution treated type 316 stainless steel at 600°C have been performed by Bolton[3]. Compact tension specimens of various thicknesses (1.5 in, 2 in, and 2.5 in) were tested to examine size dependence. The crack growth rate data are correlated with the values of C^* deduced from the experimentally measured displacement rates given in Fig. 6. The data are well fitted by the equation

$$\dot{a} = 0.005(C^*)^{0.85} , \tag{2}$$

where $\dot{a}$ is measured in mh^{-1} and C^* is measured in MPa mh^{-1}. The data do not show any dependence on specimen size. It may be noted that Eqn. (2) is similar to the Eqn. (1) obtained for type 321 stainless steel.

2.2.3 Type 316 Stainless Steel Creep-Fatigue Crack Growth Data — CEGB

The creep-fatigue crack growth tests on type 316 stainless steel will complement the constant load tests described in Section 2.2.2. Displacement-controlled cycles will run into compression with a load ratio of approximately -1 and have tensile hold periods ranging from 0.5 h to 192 h. Base line fatigue data will be collected on 1 in. compact tension specimens. Creep-fatigue data will be collected on geometrically similar compact tension specimens of various thicknesses (1, 1.5, 2, and 2.5 in). Each individual test will have a duration of approximately 1,000 h.

Design and manufacture of speciemens, test apparatus, and extensometry have been completed and a trial test has been performed. Creep-fatigue testing of the type 316 stainless steei is currently underway.

2.2.4 Type 304 Stainless Steel Cyclic Crack Growth Tests — CRIEPI

Thin-walled tubular specimens shown in Fig. 7 were used in fundamental crack growth tests (presented in Sections 2.2.4 and 2.2.5) and in exploratory subcritical crack growth tests (presented in Section 3.1.1). A crack starter, namely a 0.8 mm diameter hole, was machined in the gauge section of each specimen.

Standard cyclic crack growth tests were performed to obtain the fundamental crack growth characteristics of the test material under cyclic loads. All tests were stress-controlled, with the frequency of 0.5 Hz. Test conditions are summarized in Table 4.

Specimen elongation was measured along the 10 mm gauge length, and then used in the experimental evaluation of the J-integral type fracture mechanics parameters. Crack length was measured on the outer surface of the specimen by inspection under a microscope. Crack propagation rate was calculated by numerically differentiating the plots of the crack length vs the number of cycles. Data points used in the evaluation were those produced for the half crack length values between 1.6 and 2.6 mm.

Crack growth rates were correlated with the elastic J-integral range, ΔJ_e, given by:

$$\Delta J_e = \frac{\Delta K_{eff}^2}{E}, \tag{3}$$

where ΔK_{eff} and E are effective stress intensity factor range and Young's modulus, respectively. ΔK_{eff} was evaluated using a secant formula for center cracked specimens:

$$\Delta K_{eff} = \left(\frac{\Delta P_{eff}}{w\,t}\right)(\pi a)^{0.5}\left(\sec\left(\frac{\pi a}{w}\right)\right)^{0.5}. \tag{4}$$

Here ΔP_{eff} is the difference between the maximum load and the crack opening load estimated from load-displacement curves, w is the circumferential length at mid-thickness of the specimen, t is the thickness, and a is the half crack length measured at mid-thickness. For the present test conditions ΔP_{eff} is approximately equal to the total load range, ΔP. The graphs of crack growth rate vs ΔJ_e at 200, 400, 550, and 650°C are shown Fig. 8. Comparison of the data obtained at different temperatures for the same stress conditions indicates that the large scatter in Fig. 8 is primarily due to the temperature dependence.

Elastic-plastic fatigue J-integral range ΔJ_f was calculated as a sum of elastic and plastic contributions ΔJ_e and ΔJ_p. As shown in Fig. 9, the value of ΔJ_p was computed from the load-displacement curve with the method originally proposed by Rice et al[4] for center crack specimens. Correlation between the crack growth rate and ΔJ_f is presented in Fig. 10 for all test conditions. All data fall within a narrow band. No temperature dependence (akin to that demonstrated in Fig. 8) is observed. The following power-law relation between the crack growth rate and ΔJ_f was proposed:

$$\frac{da}{dN} = 0.0015 \Delta J_f^{1.6} , \qquad (5)$$

It is seen in Fig. 10 that Eqn. (5) approximates experimental results fairly well. It was also ascertained that the scatter of data presented here is no greater than that of the data reported by Ohtani[5] for various metallic materials and different specimen geometries.

2.2.5 Type 304 Stainless Steel Creep Crack Growth Tests — CRIEPI

Two creep crack growth tests were carried out at 550°C. Test conditions are given in Table 5. Results demonstrated that crack growth was accompanied by an unmanageably large inelastic deformation of the specimen. Experiments yielded no significant data. A different experimental approach needs to be developed.

3. SUBCRITICAL CRACK GROWTH. EXPLORATORY TESTS

3.1 CREEP-FATIGUE CRACK GROWTH TESTS UNDER MECHANICAL LOADING — CRIEPI

3.1.1 Through-Wall Crack Growth Tests

Stress-Controlled Creep-Fatigue Loading

Stress-controlled fully reversed cyclic tests were conducted at 550°C. Each cycle included hold periods at both maximum and minimum stress levels, which ranged from 10 min to 5 h. Test conditions are summarized in Table 6.

Test results are presented in Fig. 11, where crack growth rates are plotted vs hold time for three different crack lengths. As the hold time increases from zero to 10 min, a decrease in the crack growth rate can be observed. At present the reasons for such behavior are unclear. For hold times greater than 10 min, crack growth rate per cycle consistently increases. The crack growth rates produced for the 5 h hold period are approximately one order of magnitude larger than those produced for zero hold time.

Creep J-integral range, ΔJ_c, was used to correlate creep-fatigue crack growth. This parameter can be obtained from the load-displacement curves in a manner similar to that for evaluating ΔJ_f. The method for experimental determination of creep J-integral range is schematically depicted in Fig. 12. An increase in the crack growth rate with the hold time was plotted vs ΔJ_c in Fig. 13. The relationship between these two quantities appears to be quasi-linear. Comparison of the current test results to the data reported by Ohtani[5] demonstrates that the experimental data presented here fall in the upper region of the scatter band of the reference data[5].

Displacement-Controlled Creep-Fatigue Loading

Displacement-controlled tests at 550°C are summarized in Table 7. Total strain range was 0.8%. Three different tests used strain rates of 10^{-3}, 1.67×10^{-5}, and 1.67×10^{-6} s^{-1} on the tensile portion of the cycle. A strain rate of 10^{-3} s^{-1} was used on the compressive portion of the cycle in all experiments.

The graph in Fig. 14 presents the crack growth rate as a function of the fatigue J-integral range, ΔJ_f, for displacement-controlled tests, together with the data band produced in stress-controlled cyclic crack propagation experiments described above. It is seen that in displacement-controlled tests the crack growth rate increases as the crack continues to propagate. However, only slight changes in ΔJ_f are observed. The data points produced in tests, where the strain rate was 10^{-3} s^{-1} in both tension and compression, fall within the data band generated in stress-controlled tests. Conversely, the data points produced in tests, where the strain rate was 1.67×10^{-6} s^{-1} in tension and 10^{-3} s^{-1} in compression, are approximately by a factor of two higher than those produced at $\dot{\varepsilon} = 10^{-3}$ s^{-1} in both tension and compression.

3.1.2 Surface Crack Growth Tests

Surface crack growth tests were performed at 550°C. The test apparatus and test specimen are shown in Figs. 15 and 16, respectively. Electric discharge method was used to produce three initial surface flaws on both sides of the plate. A bending moment was applied through the arms attached to the two ends of the specimen. Strain range, measured in the gauge section (see Fig. 16), was kept close to 0.4%. This was accomplished by controlling stroke. For a certain number of cycles, 30 min hold periods were introduced at the maximum and minimum stroke levels. Cyclic loading of the smaller amplitude was periodically imposed at room temperature to produce "beachmarks" on the fracture surface. The loading history is schematically shown in Fig. 17.

Development of crack B (see Fig. 16 for definition of cracks A, B, and C), obtained by replication of the specimen surface, is shown in Fig. 18. A number of microcracks emanating from the "main" crack can be seen. Fracture surfaces of the cracks A, B, and C are shown in Figs. 19, 20, and 21, respectively. Variation in crack width and depth with the number of cycles is shown in Fig. 22 for crack B. Due to the nature of the bending load, the crack aspect ratio (depth/width) tends to decrease as the cycling progresses.

3.2 CREEP-FATIGUE CRACK GROWTH TESTS UNDER REPEATED THERMAL TRANSIENT CONDITIONS — EPRI/CRIEPI

3.2.1 Thermal Shock Tests of Preflawed Thick-Walled Cylinders — EPRI

The purpose of this effort is to investigate slow stable crack growth at elevated temperatures. Thermal shock tests on preflawed thick-walled cylinders combine repeated thermal and sustained axial load (σ_{max} = 160 MPa). Thermal shock cycle is schematically shown in Fig. 23. Test duration will be 90 days or until failure, whichever occurs first. Tests will be interrupted for inspection.

The thick-walled cylindrical test specimen is shown in Fig. 24. One circumferential flaw was machined on the outer surface in the gauge section of each specimen. It should be noted that the gauge section is not located directly in the middle of the specimen. Such arrangement makes it possible to move the induction heating coil and to inspect the flawed area without removing the specimen from the grips and thus violating specimen allignment. Two types of flaw geometries (see Fig. 25) are employed to assess the effect of the flaw shape on subcritical crack growth. Flaws are manufactured by the electric discharge method.

The testing facility was constructed by combining an existing thermal shock facility (see Fig. 26) with the axial load capability. The complete assembly is presented in Fig. 27.

3.2.2 Thermal Shock Tests of Preflawed Cylinders — CRIEPI

Thermal shock tests of preflawed cylinders are currently underway. At present only preliminary results are available. The experimental apparatus is shown schematically in Fig. 28. Repeated thermal shocks are applied to the outer surface of the specimens by moving the chamber with the hot and cold plena along the vertical axis. In addition, axial mechanical loading is imposed. The plena contain liquid metal similar to solder. Temperatures in the hot and cold plena are kept at 550 and 150°C, respectively. The two types of thermal transients applied to the outer surface of the specimen in the vicinity of the preflawed sections are presented in Fig. 29.

Cylindrical specimens with an outside diameter of 160 mm and a thickness of 15 mm are used in experiments. Circumferential flaws of various sizes and shapes are machined by electric discharge method on both the inner and outer surfaces of the specimen (as shown in Figs. 30 and 31). Distances between individual flaws are believed to be sufficiently large to preclude any significant crack interactions, at least until considerable crack growth takes place.

Variations with time of temperature, mechanical axial strain, and position of the chamber are presented in Fig. 32. Temperature and mechanical axial strain are measured at the center of the inner surface of the specimen. Crack growth, originating at the flaw of least depth in Section B-B' at the outer surface of the specimen, is shown in Fig. 33. It is seen in Fig. 33 that cracks grow from the corners of the flaw.

3.3 CREEP-FATIGUE CRACK GROWTH TESTS UNDER DISPLACEMENT CONTROLLED CYCLING — CEGB

The creep-fatigue tests on austenitic fillet welded features are nearing completion. Results to-date are presented below in the form of endurance curves and crack growth data. A creep-fatigue crack growth analysis is performed on the specimens to predict the numbers of cycles to failure. The approach taken is based on the approximate reference stress methods of analysis described in Section 4.1.1.

Two geometries were tested, each consisting of a flat strip of AISI type 321 stainless steel, a 2 mm thick fillet, welded with AISI type 347 filler metal to a flat strip of AISI type 321 stainless steel 3.25 mm thick. The geometries, termed "cantilever" and "wishbone" arrangements, are shown schematically in Fig. 34. These are designed so that failure occurs in the region of the weld in the "cantilever" geometry and in the thinner strip in the "wishbone" geometry. After manufacture, the weld features were given an accelerated aging treatment at 750°C for 200 h.

Creep-fatigue tests were carried out at 650°C in air by fully reversed bending of the long arms of the specimens (Fig. 34) over a fixed displacement range. The displacement was held constant at the maximum (+δ, see Fig. 34) for periods of either 10, 30, or 300 min. During several tests on the "cantilever" arrangement, displacement was held constant at the minimum (-δ) for 30 min. In addition, three tests with no displacement hold periods were performed. The fatigue cycles were sinusoidal in all cases. Three creep-fatigue tests of the "wishbone" type specimens were interrupted at intervals, and the extent of crack growth at the surface was optically measured after polishing one surface of the specimens. All the tests were continued beyond the point where the maximum load during the cycle fell to half of its original value.

To provide additional data to check the analytical predictions, load relaxation tests were carried out on both "cantilever" and "wishbone" specimens. A "cantilever" specimen was loaded in tension by displacing the moment arm by approximately 3.5 mm. This displacement was held constant and the relaxed loads were measured at intervals during the 500 h test period. Similarly, a "wishbone" specimen was loaded in tension by displacing the moment arm by approximately 6 mm. Relaxed loads were measured over a period of 100 h. After the hold period, one fully reversed fatigue cycle was performed and load relaxation from the new load level was recorded for approximately 1,000 h.

3.3.1 Metallography

"Cantilever" Arrangement

The majority of "cantilever" specimens failed by creep-fatigue crack growth along the heat affected zone (HAZ) close to the weld fusion boundary. The specimens subjected to tensile hold periods initiated intergranular cracks during the hold time at the unfused area, close to the weld root. The specimens subjected to compressive hold periods initiated intergranular cracks during the hold time at the weld toe. Transgranular fatigue cracks, which were observed to propagate from the opposite side to the creep-fatigue cracks, also tended to follow the fusion boundary. The specimen tested under pure fatigue cycling cracked in the weld metal.

"Wishbone" Arrangement

The majority of "wishbone" tests failed by creep-fatigue crack growth across the thin base metal strip (AISI type 321 stainless steel). During the displacement hold multiple cracking was observed on the surface held in tension. (As many as ten intergranular regularly spaced cracks were recorded). Transgranular fatigue cracks propagated on the side held in compression. The pure fatigue tests failed by transgranular cracking on both sides of the thinner strip. Again, multiple fatigue cracks were observed.

3.3.2 Cyclic Load-Displacement Behavior

The applied loads at maximum and minimum displacement were measured and plotted vs the number of cycles in Fig. 35. In the "cantilever" tests with the tensile hold period (Fig. 35a), the maximum load falls off gradually over the duration of testing and the minimum load remains approximately constant until a late stage in life. The load-displacement hysteresis loops display a marked change in compliance in the compressive quadrant due to crack closure (Fig. 36a). The crack closure effect is enhanced by the abutment of the heel of the displaced strip at the weld root against the relatively stiff short strip (see Fig. 34). The hysteresis loops obtained for a "cantilever" specimen subjected to loading with compressive hold periods are shown in Fig. 36b. Crack closure is observed in the tensile quadrant and abutment closure, in the compressive quadrant. In these tests the major creep-fatigue crack propagates inwards from the weld toe at the outer surface.

In the "wishbone" tests with tensile hold periods, the maximum and minimum loads remain approximately constant for a large fraction of life before abruptly falling towards the failure point (Fig. 35b). As the load falls rapidly in the "wishbone" specimens, the shape of the cyclic load-displacement loop suddenly changes due to crack closure (Fig. 36c). Crack closure is not evident until this late stage in the life of the "wishbone" specimens.

3.3.3 Creep-Fatigue Endurance Curves

Results of all tests reported here are summarized in Fig. 37. The number of cycles to failure, N_f^{exp}, is defined as the number of cycles required for the maximum load to fall to half of its original value. The equivalent nominal elastic strain range is calculated by assuming a completely elastic applied displacement range. The ASME Code Case N-47[6] curve T-1420, with design factors removed to produce a material failure curve, is presented in Fig. 37 as well.

A significant scatter is observed in the endurance data obtained for the tests with displacement hold time. There appeared to be no difference between results produced for "cantilever" type specimens subjected to tensile and compressive hold periods. The tests with the 300 min tensile hold period yielded results, which were at the bottom of the scatter band produced for the tests with the 30 min hold periods.

3.3.4 Crack Growth Correlations

Three "wishbone" creep-fatigue tests were interrupted for crack length measurements at intervals of about 80 cycles. The major crack length vs number of cycles data was fitted with a quadratic function, and the rate of crack growth per cycle, da/dN, was determined at each of the measurement stations. The elastic stress intensity factor range, ΔK, was calculated using an expression for SENB specimens. The effective stress intensity factor range, ΔK_{eff}, was calculated using the approach described in Section 4.1.1. Since q_0 could not be measured experimentally until the crack became very deep, the value $q_0 = 0.84$ was taken from the result of Section 4.1.1.

The correlation between the crack growth rates and ΔK_{eff} is shown in Fig. 38 for the two "wishbone" type specimens subjected to the creep-fatigue loading. It should be noted that the crack growth rates in Fig. 38 are the total rates. Because the total crack length was measured optically, it was not possible to separate the creep and cyclic components as done in Section 4.1.1. However, the 30 min hold period is believed to be insufficient to cause a large increase in the growth rate due to fatigue.

3.3.5 Analysis Procedure

For the purposes of analysis, the specimens are idealized as collections of beams built-in where they are welded to the rigid mounting block (Fig. 34). The lateral displacement imposed upon the uncracked beam, δ^{uc}, is related to the curvature along the beam by standard relationships. The additional displacement due to the presence of a single crack is written in terms of the elastic-plastic rotation due to the crack, Θ^{c}_{ep}:

$$\delta^c = \Theta^c_{ep} l_1 \qquad \text{"cantilever" specimen,} \qquad (6)$$

$$\delta^c = \Theta^c_{ep} l_2 \qquad \text{"cantilever" specimen,} \qquad (7)$$

Reference stress approximations are used to analyze the plastic response and the creep behavior of the uncracked and the cracked beam. The elastic-plastic curvature for the fatigue cycle is approximated by:

$$\kappa_{ep} = \kappa_e \frac{\varepsilon_{ep}(\sigma_r^{uc})}{\varepsilon_e(\sigma_r^{uc})} , \tag{8}$$

where κ_e is the elastic curvature and $\sigma_r{}^{uc}$ is the uncracked body reference stress for a bending beam, given by:

$$\sigma_r^{uc} = \frac{4M}{w^2} . \tag{9}$$

Here M is the calculated maximum moment per unit width, ε_{ep} and ε_e are the elastic-plastic and elastic contributions to strain, determined from constitutive relations for AISI type 321 stainless steel and taken from the full range cyclic stress-strain curve. During the hold period, the creep curvature rate may be computed as:

$$\dot{\kappa} = \dot{\kappa}_e + \dot{\kappa}_c = \dot{\kappa}_e + \kappa_o \frac{\dot{\varepsilon}_c(\sigma_r^{uc})}{\varepsilon_e(\sigma_r^{uc})} , \tag{10}$$

where $\dot{\varepsilon}_c(\sigma_r^{uc})$ is the creep strain rate in relaxation for AISI type 321 stainless steel.

The uncracked ligament is assumed to be in plane strain and is modelled as a line spring embedded in the beam. Additional elastic rotation due to the presence of a single crack is given by (Ewing[7]):

$$\Theta_e^c = 2\frac{(1-\nu^2)}{E}\alpha_b\left(\frac{a}{w}\right)\frac{6M^*}{w^2} , \tag{11}$$

where $\alpha_b(a/w)$ is a non-dimensional compliance integral for bending and M^* is the moment at the ligament. Elastic-plastic rotation from the reference stress approximation is:

$$\Theta_{ep}^c = \Theta_e^c \frac{\varepsilon_{ep}(\sigma_r^c)}{\varepsilon_e(\sigma_r^c)} , \tag{12}$$

where the cracked body reference stress is:

$$\sigma_r^c = \frac{4M^*}{m(a/w)(w-a)^2} , \tag{13}$$

and the plane strain, Tresca limit load function m(a/w) is given in Miller[8]. Cyclic stress-strain curve for aged material was used to compute Θ^c_{ep}.

During the hold period, rotation due to one crack is approximated by:

$$\dot{\Theta}^c = \dot{\Theta}^c_e + \dot{\Theta}^c_c = \dot{\Theta}^c_e + \Theta^c_e \frac{\dot{\varepsilon}_c(\sigma_r^c)}{\varepsilon_e(\sigma_r^c)} , \tag{14}$$

3.3.6 Creep-Fatigue Crack Growth

The amount of crack growth per cycle was calculated as the sum of fatigue and creep (hold period) contributions, in accordance with Eqn. (16) of Section 4.1.1 below. The procedure is outlined in a flow chart in Fig. 39. In the analysis no allowance was made for creep crack initiation. Fatigue crack growth per cycle was calculated from Eqn. (17) of Section 4.1.1. Values of the coefficient C and the exponent l used in Eqn. (17) were determined for the material in which the cracking occurred (either the AISI type 347 stainless steel weld metal or the AISI type 321 stainless steel base metal).

For the symmetrical load cycle considered here, the stress intensity factor range was determined from twice the calculated maximum bending moment per unit thickness. Effects of plasticity were included by using the full range cyclic stress-strain curve for the aged AISI type 321 stainless steel in the reference stress J estimates.

The creep crack growth during the hold periods was determined from Eqn. (19) of Section 4.1.1. During the fatigue cycle, which is assumed to be symmetrical throughout the lifetime of the specimens, the maximum load P is found by solving the following non-linear relation for the known displacement δ:

$$\delta = \delta^{uc} + \gamma\delta^c , \tag{15}$$

where γ is the number of assumed cracks along the thinner strip length in the "wishbone" type specimens ($\gamma = 3$ for the "wishbone" specimens and $\gamma = 1$ for the "cantilever" specimens). Sensitivity of the predictions to the value of γ was examined and found not to be unduly strong. The initial crack length was assumed to be equal to one grain diameter (a_0=0.05 mm) for the "wishbone" specimens and for the "cantilever" specimens which were held with the notch root in compression. For the "cantilever" specimens subjected to tensile hold periods, the initial crack length was taken as the measured notch depth at the weld root. Results obtained for the "wishbone" specimens appeared to be reasonably insensitive to the assumed initial crack length.

Given the load and the instantaneous crack length, the effective equivalent stress intensity range was determined and hence the increment in the cyclic crack growth contribution was found.

During the dwell period, the displacement was held constant at its maximum value, and the equation governing load drop rate was solved simultaneously with the creep crack growth law.

The calculations were continued by incrementing the crack length at each step in the numerical solutions, until the predicted maximum load dropped to half of its initial value, consistent with the definition of failure adopted in the experimental procedure.

3.3.7 Initial Load

As a check on the beam/line spring model, independent of the crack growth laws, the initial measured and calculated loads were compared. Although the total applied displacement range was controlled accurately, it was not necessarily applied symmetrically as the central zero was difficult to set. Therefore, the mean of the measured tensile and compressive loads were used for the comparison with the calculated loads. Figure 40 shows good agreement between the measured and calculated loads. It should also be noted that the "wishbone" specimens had a significant amount of plasticity in the deforming beam.

3.3.8 Load Relaxation

Load relaxation as a function of time is shown in Fig. 41 for the two geometries. Calculations were based on the assumption that the displacement was both applied and measured instantaneously. This results in overestimating the initial load. The calculated relaxation rate tends to be overestimated as well.

3.3.9 Analytical Results for Lifetime and Cyclic Response

The number of cycles to failure calculated from the reference stress analysis outlined above are compared with the experimental data in Fig. 42. Both calculated and experimental results yield a faster fall off in load at the end of life for the "wishbone" specimens than for the "cantilever" ones (Fig. 35). A comparison between the predicted and measured semi-load ranges obtained for the "wishbone" specimen W9 is presented in Fig. 43. Results in Fig. 44 demonstrate good agreement between the measured and predicted total crack growth for the "wishbone" specimen W9. Predicted cyclic and creep crack growth contributions to the predicted total crack growth are shown in Fig. 44 as well .

4. SUBCRITICAL CRACK GROWTH MODELING

4.1 INDENTIFICATION OF THE POTENTIAL CREEP-FATIGUE CRACK GROWTH MODEL — CRIEPI/CEGB

4.1.1 Simplified Methods — CEGB

Within the CEGB, simplified methods for calculating creep-fatigue crack growth are currently being developed as part of the R5 assessment procedure for the high temperature response of structures. The procedure separates the total crack growth per cycle into fatigue and creep components:

$$\frac{da}{dN} = \left(\frac{da}{dN}\right)_f + \left(\frac{da}{dN}\right)_c , \tag{16}$$

The fatigue component is described by a modified Paris law:

$$\left(\frac{da}{dN}\right)_f = C(\Delta K_{eff})^l, \tag{17}$$

where C and l are constants. The effective stress intensity factor range, ΔK_{eff}, represents the opening part of the total stress intensity factor range as depicted in Fig. 45. In the simplified approach it is expressed as a fraction of the total stress intensity factor range, ΔK, as follows:

$$\Delta K_{eff} = q_0 \Delta K, \tag{18}$$

The fraction q_0 is a function of the ratio of the minimum and maximum stress intensity factors during the cycle as shown by the line in Fig. 46. This line is an approximation based on data collected on a wide range of ferritic and austenitic steels. This was confirmed as a conservative representation by the results on type 321 stainless steel described in Section 2.2.1. Experimental values of q_0 are compared to the analytical line in Fig. 47.

Although Eqn. (17) is a simple representation of fatigue crack growth data, it is found that the constants C and l are dependent on the hold time in the cycle. This is because the crack is expected to grow through material which has seen significant creep damage during the dwell time. The effect of total time on fatigue crack growth data for the type 321 stainless steel is shown in Fig. 48. However, only the crack growth during the fatigue part of the cycle is shown in Fig. 48. The creep crack growth component has been separated and was presented in Fig. 5.

As creep crack growth rates follow Eqn. (1), the creep contribution to the total crack growth in Eqn. (16) can be represented as

$$\left(\frac{da}{dN}\right)_c = \int_0^{t_h} AC^{*q}\,dt, \tag{19}$$

where t_h is the total time in the cycle, and A and q are constants in the creep crack growth equation.

A difficulty with the C^* approach in Eqn. (19) is that C^* has to be evaluated for cracks in complex geometries. Within the CEGB, approximate reference stress methods have been developed to provide estimates of C^*. The approximation is

$$C^* = \sigma_{ref}\dot{\varepsilon}^c_{ref}R, \tag{20}$$

where the reference stress σ_{ref} is defined by

$$\sigma_{ref} = P\frac{\sigma_Y}{P_L(\sigma_Y, a)}, \tag{21}$$

and R' is a length parameter

$$R = \frac{K^2}{\sigma^2_{ref}}, \tag{22}$$

Here P is the magnitude of the applied load and P_L is the corresponding plastic collapse load for a yield stress σ_Y and crack size a. K is the value of the elastic stress intensity factor at the load P and $\dot{\varepsilon}^c_{ref}$ is the creep strain rate from uniaxial creep data at the reference stress level.

The reference stress approach is useful for practical applications because:

(1) In Eqn. (20) it is necessary to calculate only the stress intensity factor and the limit load. Such solutions are widely available because of their use in low temperature fracture assessment procedures such as R6.

(2) Eqn. (20) is not restricted to secondary creep described by a simple power law. It allows realistic creep data, including primary, secondary, and tertiary stages to be incorporated in the creep strain rate at the reference stress. The effect of cyclic hardening or softening on the material creep data can also be readily included.

(3) Strain hardening rules may be used to allow for the increase in stress levels as a crack grows, by interpreting the creep strain rate as the strain rate at the current reference stress and at the creep strain accumulated under the reference stress history.

The validity of using realistic creep laws in applying strain hardening rules has been checked for a range of materials by comparing Eqn. (20) with the test data, for which C^* can be estimated from experimental displacement rate measurements or experimental load drop measurements. In Fig. 49 the predictions of Eqn. (20) are compared with the experimental data described in Section 2.2.2 for type 316 stainless steel. A plane stress reference stress has been used to evaluate C^*_{ref}. Several double-edge-notched tension specimens were tested as well. In this case C^*_{ref} is compared to C^* ($\dot{a}_{DENT}$). The values of C^* ($\dot{a}_{DENT}$) are obtained by entering Fig. 6 at the experimentally measured crack growth rates ($\dot{a}_{DENT}$) for the DENT specimens and reading off the corresponding values of C^* according to the fit of Eqn. (2). The good agreement in Fig. 49 indicates that the use of the reference stress estimate of C^* in conjunction with data, $\dot{a}(C^*)$, derived from CT specimens, provides a good estimate of crack growth in other geometries (in this case, the DENT geometry).

Under cyclic displacement loading it is necessary to include the variation of creep strain rate during the dwell period as the stress levels relax in Eqn. (20). It has been found that the rate at which the reference stress falls may be represented as:

$$\dot{\sigma}_{ref} = -E\frac{\dot{\varepsilon}^{c}_{ref}}{\mu}, \tag{23}$$

where μ is a factor estimated from the elastic and creep compliances ($\mu \cong 2$ for the CT specimens). Predictions of Eqn. (20) for the cyclic data given Fig. 5 are shown in Fig. 50. It is seen that the reference stress predictions are close to the experimental data points.

In the reference stress predictions shown in Fig. 50, it should be noted that creep data were obtained from stress relaxation tests on the cyclically hardened material. Had creep data from constant load tests on virgin material been used, the good agreement in Fig. 50 would not have been obtained. Results similar to those shown in Fig. 50 have been obtained for austenitic weld metals and for ferritic steels. These suggest that the reference stress methods developed for constant load can be extended in a simple manner to predict crack growth under cyclic conditions. The effect of the creep-fatigue interaction appears to be reflected in the effect of the total cycle time on the fatigue crack growth, as illustrated in Fig. 48.

4.1.2 Cyclic Crack Growth Modeling — CRIEPI

GE/EPRI Method[9,10]

Graphs in Fig. 10 demonstrate that the experimentally determined fatigue J-integral range, ΔJ_f, correlates crack growth under rapid cycling fairly well. It is therefore important to establish a method for analytically evaluating ΔJ_f. Two of such analytical procedures are considered here.

The first method uses nonlinear finite element solutions tabulated in a nondimensional form for typical specimen geometries. These fully plastic solutions were produced by GE/EPRI[9,10] for ductile fracture analysis. However, they can also be used to estimate ΔJ_f as long as the cyclic stress-strain relation is represented by the Ramberg-Osgood equation of the following form:

$$\Delta\varepsilon = \frac{\Delta\sigma}{E} + \alpha(\Delta\sigma)^n , \tag{24}$$

where $\Delta\varepsilon$ and $\Delta\sigma$ are the strain and stress ranges at steady-state cycling, E is Young's modulus, a and n are temperature-dependent material constants. Results presented in Fig. 2 indicate that for a range of temperatures Eqn. (24) approximates the behavior of the test material fairly well.

Like the J-integral in the elastic-plastic monotonic fracture analysis, the fatigue J-integral range can be represented as the sum of elastic and plastic contributions:

$$\Delta J_f = \Delta J_e + \Delta J_p , \tag{25}$$

For a center cracked panel:

$$\Delta J_e = \frac{\Delta K^2}{E} , \tag{26}$$

$$\Delta J_p = \alpha a\left(\frac{c}{b}\right)h_1\left(\frac{a}{b},n\right)\left(\frac{\Delta P}{2ct}\right)^{n+} , \tag{27}$$

where a, b, c, and t represent half crack length, half specimen width, half ligament length, and specimen thickness, respectively; and h_1 is the nondimensionalized fully plastic solution for the J-integral tabulated as a function of a/b and n[10]. To apply these equations to the tubular specimen employed in the present study, the following substitution was made:

$$b = \pi r , \tag{28}$$

where r represents the mean radius of the specimen. For relatively short cracks considered here this approximation should not introduce significant error into ΔJ_f.

Values of ΔJ_f calculated with Eqn. (25) were compared to those determined from the experimental load-displacement relations. Results presented in Fig. 51 demonstrate excellent agreement except for small stress ranges, where ΔJ_f is overestimated. A possible explanation for this discrepancy is that the cyclic stress-strain relation in the present study was established based on the strain range step-up tests, and therefore may not truly represent the steady-state behavior.

Reference Stress Method

The reference stress method was developed as a tool for evaluating the inelastic deformation of structures based on results of elastic analysis[11]. According to the reference stress method, ΔJ_f can be represented as follows:

$$\Delta J_f = \frac{E\Delta\varepsilon_{ref}}{\Delta\sigma_{ref}}\Delta J_e , \tag{29}$$

where $\Delta\sigma_{ref}$ is the reference stress given by

$$\Delta\sigma_{ref} = \frac{\Delta P}{2ct} , \tag{30}$$

and $\Delta\varepsilon_{ref}$ is the strain range corresponding to $\Delta\sigma_{ref}$ on the material cyclic stress-strain curve. $\Delta\varepsilon_{ref}$ can be obtained by substituting $\Delta\sigma_{ref}$ for $\Delta\sigma$ in Eqn. (24):

$$\Delta\varepsilon_{ref} = \frac{\Delta\sigma_{ref}}{E} + \alpha\left(\Delta\sigma_{ref}\right)^{n} \cdot \tag{31}$$

It should be noted that this technique requires neither the fully plastic solutions, nor the approximation of the cyclic stress-strain relation by a Ramberg-Osgood type equation. It can therefore be applied in cases where only linear elastic solutions exist and the Ramberg-Osgood approximation is not suitable. However, since this method relies on certain assumptions of structural behavior in the inelastic range, proper definition of the reference stress is necessary to assure an accurate solution[12].

Values of ΔJ_f calculated with Eqn. (29) were compared to those obtained with the GE/EPRI method (see Fig. 52). Results in Fig. 52 show that the reference stress method yields somewhat lower values of ΔJ_f than the GE/EPRI method. This trend becomes more pronounced as the stress range and plastic contribution to ΔJ_f increase. Such behavior can be explained by the dependence of the function h_1 on the hardening exponent n. The agreement between the two methods can be improved by modifying the reference stress equation[12].

4.1.3 Creep-Fatigue Crack Growth Modeling — CRIEPI

In recent years the creep J-integral range, ΔJ_c, proved effective in modeling the creep-fatigue crack growth under creep dominant conditions. However, ΔJ_c is usually determined from the experimental load-displacement curves. So far, methods for analytical evaluation of ΔJ_c have not been well established.

In the present study an attempt was made to develop a simplified analytical procedure for evaluating ΔJ_c. Assuming steady-state conditions, ΔJ_c can be represented as a simple product of the C^* integral and the hold time t_h. The C^* integral can be determined with the GE/EPRI method as:

$$C^* = \kappa a\left(\frac{c}{b}\right)h\left(\frac{a}{b}, m\right)\left(\frac{P}{2ct}\right)^{m+1} , \tag{32}$$

where k and m are material constants representing the dependence of the steady-state creep strain rate $\dot{\varepsilon}^s$ on the applied stress σ:

$$\dot{\varepsilon}^s = k\sigma^m \ . \tag{33}$$

Then ΔJ_c becomes:

$$\Delta J_c = C^* t_h \ . \tag{34}$$

Values of ΔJ_c calculated with Eqns. (32-34) were compared with those determined from experimental records for three different hold times (see Fig. 53). Comparison demonstrated that the experimental values were considerably higher than the analytical ones. To improve the agreement between experimental and analytical results, it is necessary to account for the transient behavior during the stress hold period, which can be attributed to (1) presence of non steady-state creep, or (2) non instantaneous transition of the stress field from the elastic-plastic state to the steady-state creep state. Thus transient creep behavior and the effect of reverse plastic straining under cyclic loading must be considered. In addition to that, in order to investigate transition of the stress field from the elastic-plastic to the steady-state creep state, it is necessary to consider exponents governing both types of deformation. Methods based on the assumption of the steady-state conditions tend to underpredict deformations occurring during the transient period. Therefore a more detailed study on this subject is warranted.

4.1.4 Finite Element Analyses of Simple Geometries — CEGB

The finite element program BERSAFE has been used to produce results for C(t) for both compact tension and single edge notch geometries. Following initial elastic loading, creep analyses were performed under constant load for the creep law

$$\dot{\varepsilon}^c = A\sigma^n \ , \tag{35}$$

with n = 5. Results are presented in terms of a dimensionless time

$$\tau = EC^* \frac{t}{K^2} , \tag{36}$$

where $E' = E/(1-\nu^2)$, E is Young's modulus, and ν is Poisson's ratio. Finite element results suggest that the steady state has essentially been reached at time $\tau = 1$.

Computed steady-state values of C^* are in good agreement with those given by Kumar et al[9] for the compact tension specimen and Shih and Needleman[13] for the single edge notched geometries. Graphic representation of C(t) is given in Fig. 54 for the compact tension specimens and for the single edge notch geometry under tension and bending. Results in Fig. 54 are compared with the estimate of Ehlers and Riedel[14]

$$C(\tau) = C^*\left(1 + \frac{1}{(n+1)\tau}\right), \tag{37}$$

which is the sum of the long-time limit and the short-time limit of Riedel and Rice[15]. Also shown is the more recent estimate of Ainsworth and Budden[16]

$$C(\tau) = C^* \frac{(1+\tau)^{n+1}}{(1+\tau)^{n+1} - 1}, \tag{38}$$

which is based on summation of long- and short-time limits of J.

Although Eqn. (38) appears to be more complex than Eqn. (37), it is more convenient to integrate and results in the approximate estimate

$$\int_0^t C(t)^{\frac{n}{n+1}} dt \cong C^{*\frac{n}{n+1}} t \left[1 + \frac{\sigma_{ref}}{E\varepsilon^c_{ref}(T)}\right], \tag{39}$$

The integral in Eqn. (39) is proportional to the creep strain near the crack tip. Thus Eqn. (39) shows that this creep strain is increased above that which would have been accumulated under steady state creep by the factor of [1+elastic strain at the reference stress / creep strain at the reference stress]. Since the power of C^* in Eqns. (1, 2) is approximately n/(n+1), this same factor may be used to incorporate the effects of transient creep on creep crack growth.

For the compact tension specimen, the parameter C_t developed by Saxena[17] has been calculated from the computed load-line displacement rate and is compared to C(t) in Fig. 55. It can be seen that C_t<<C(t) for τ<<1, similar to the results reported by Leung et al[18]. Indeed Saxena[17] showed that C_t does not have the 1/t dependence which C(t) has as $t \to 0$ (see Eqns. 37 and 38).

4.1.5 Finite Element Analysis of Surface Crack Growth — CRIEPI

It was shown in Section 4.1.2 that ΔJ_f can be calculated using the finite element solutions and the material cyclic stress-strain curve for through-wall cracks. To examine the applicability of this method to surface crack problems, an analytical study of the test described in Section 3.1.2 was conducted.

The fully plastic solutions for surface cracks, which have so far appeared in the literature[19], are generally limited as regards the geometric parameters and loading conditions. Thus elastic-plastic finite element analyses were used to estimate ΔJ_f for the surface crack growth test performed in this study. A finite element model, consisting of 20-noded isoparametric elements, is shown in Fig. 56. Due to the symmetry of the geometry and loading, one quarter of the plate was modeled. Three different crack sizes were analyzed, corresponding finite element meshes are shown in Fig. 57. All three cracks were semi-elliptical with the same aspect ratio and resembled crack B in the test specimen. Elastic-plastic analysis employed a semi-cyclic stress-strain curve, representing relation between half strain range and half stress range in the cyclically saturated condition. The J-integral was calculated with the virtual crack extension method[20] along the evaluation paths shown in Fig. 58. Since the semi-cyclic stress-strain relation was emoloyed, the ΔJ_f was calculated by multiplying the J-integral by four.

Distribution of ΔJ_f along the crack front is presented in Fig. 59 for five different load levels as a function of nominal bending strain. The ΔJ_f shows two peaks along the crack front, one at 90° and the other at 10° measured counter clockwise from the surface of the plate. Crack growth rate at the 90° station was determined from the beachmarks on the fracture surface and then plotted vs the ΔJ_f values obtained by a linear interpolation of the calculated results against crack depth (see Fig. 60). Resulting data points fall within the data band produced in the fundamental crack growth tests for the through-wall cracks. Thus data obtained in the through-wall crack tests can be used to analyze surface crack behavior.

5. EXPLORATORY FAILURE TESTS — EPRI

5.1 INTERNAL PRESSURIZATION TESTS OF PREFLAWED PIPES — EPRI

Exploratory failure tests on preflawed pipes are designed to investigate development of critical crack growth and/or ligament instability. Material used is AISI type 304 stainless steel, reference heat 9T2796. A thin-walled pipe specimen is shown in Fig. 61. A small axial flaw is manufactured in the middle of the gauge section on the outer surface of each specimen with the electric discharge method. Two flaw geometries, schematically depicted in Fig. 62, are used in order to assess the effect of the flaw shape on the critical crack growth.

In preparation for testing, four specimens have been machined and preflawed (see Fig. 63). Shadowgraphs of the flaw replicas are shown in Fig. 64 (a-d). Crack opening displacement is measured with capacitance strain gages. A detail of the specimen with the strain gage is shown in Fig. 65.

A testing facility, consisting of the furnace and pressurization unit, has been constructed. The pressurized pipe specimen assembly includes a filler plug and blast shield to minimize the consequence of "dynamic" failure. A schematic of the specimen with filler plug and core is given in Fig. 66. Furnace and pressurization unit are presented in Figs. 67-68. Internal pressurization is accomplished with nitrogen under manual control. Specimens are to be subjected to stepwise loading (see in Fig. 69) at room temperature and at 538°C.

5.2 THERMAL SHOCK TESTS OF PREFLAWED THIN-WALLED CYLINDERS — EPRI

Crack growth tests under combined thermal shock and axial loading described in Section 3.2.1. will be performed on thin-walled preflawed cylindrical specimens. Specimens are similar to those shown in Fig. 24, except in this case the inside diameter is 1.625 in. All other dimensions remain unchanged. Unstable crack growth is expected to occur. To promote critical crack growth, the circumferential flaw, machined in the middle of the gauge section, has an aspect ratio >> 1. Flaw geometry is shown schematically in Fig. 70.

REFERENCES

1. D. N. Gladwin, D. A. Miller, G. J. Neate, and R. H. Priest, "Creep, Fatigue and Creep-Fatigue Crack Growth Rates in Parent and Simulated HAZ Type 321 Stainless Steel," *Fatigue and Fracture of Engineering Materials and Structures* 11, 355-370 (1988).

2. R. Ohtani, T. Kitamura, A. Nitta, and K. Kuwabara, "High Temperature LCF Crack Propagation and Life Laws of Smooth Specimens Derived from Crack Propagation Laws," ASTM STP 942, 1985.

3. C. J. Bolton, *Creep Crack Initiation and Growth in Type 316 Stainless Steel*, CEGB Report TPRD/B/0835/N84, Central Electricity Generating Board, United Kingdom, 1984.

4. J. R. Rice, P. C. Paris, and J. G. Merkle, "Some Further Results on J-Integral Analysis and Estimates," *Fracture Toughness*, ASTM STP 514, 40-69 (1972).

5. R. Ohtani, "Characteristics of Elevated Temperature Strength Viewed From the Standpoint of Creep-Fatigue Crack Propagation," *Transactions of JSME* 52-478, 1461-1468 (1986).

6. *ASME Boiler and Pressure Vessel Code, Code Case N-47-26*, 1986.

7. D. J. F. Ewing, *Stress Intensity Factors for Plates and Shells with Long Part-Through Cracks, as Calculated by a Line-Spring Model*, CEGB Report TPRD/L/3163/R87, Central Electricity Generating Board, United Kingdom, 1987.

8. A. G. Miller, *Review of Limit Loads of Structures Containing Defects*, CEGB Report TPRD/B/0093/N82 Rev. 2, Central Electricity Generating Board, United Kingdom, 1987.

9. V. Kumar, M. D. German, and C. F. Shih, *An Engineering Approach to Elastic-Plastic Fracture Analysis*, EPRI NP-1931, Electric Power Research Institute, Palo Alto, Calif., 1981.

10. V. Kumar, M. D. German, W. W. Wilkening, W. R. Andrews, H. G. deLorenzi, and D. F. Mowbray, *Advances in Elastic-Plastic Fracture Analyses*, EPRI NP-3607, Electric Power Research Institute, Palo Alto, Calif., 1984.

11. I. W. Goodall, F. A. Leckie, A. R. S. Ponter, and C. H. A. Townley, "The Development of High Temperature Design Methods Based on Reference Stresses and Bounding Theorems," *Journal of Engineering Materials and Technology 101*, 349-355 (1979).

12. R. A. Ainsworth, "The Assessment of Defects in Structures of Strain Hardening Material," *Engineering Fracture Mechanics* 19, 632-642.

13. C. F. Shih and A. Needleman, "Fully Plastic Crack Problems, Part 1: Solution by a Penalty Method," *Journal of Applied Mechanics* 51, 48-56 (1984).

14. R. Ehlers and H. Riedel, "A Finite-Element Analysis of Creep Deformation in a Specimen Containing a Macroscopic Crack," ICF5, Vol. 2, D. Francois, ed., 1981, p. 691.

15. H. Riedel and J. R. Rice, "Tensile Cracks in Creeping Solids," *Fracture Mechanics: Twelfth Conference*, ASTM STP 700, 1980, pp. 112-30.

16. R. A. Ainsworth and P. J. Budden, *Crack Tip Fields Under Non-Steady Creep Conditions I: Estimates of the Amplitudes of the Fields*, CEGB Report RD1B/6005/R88, Central Electricity Generating Board, United Kingdom, 1988.

17. A. Saxena, "Creep Crack Growth Under Non-Steady Conditions," ASTM STP 905, 185-201 (1986).

18. C. P. Leung, D. L. McDowell, and A. Saxena, "Consideration of Primary Creep at a Stationary Crack Tip: Implication for the C_t parameter," *International Journal of Fracture* 36, 275-289 (1988).

19. G. Yagawa and H. Ueda, *A Finite Element Analysis of Inelastic Behavior of Surface Cracks*, NUREG/CP-0092, 427-461 (1988).

20. G. Yagawa, S. Yoshimura, and H. Ueda, "An Estimation Scheme for J- and C*-Integral for Surface Cracks," presented at International Symposium on Pressure Vessel Technology and Nuclear Codes and Standards, Seoul, Korea, 1989.

21. H. G. deLorenzi, "3-D Elastic-Plastic Fracture Mechanics With ADINA," *Computers and Structures* 13, 613-621 (1981).

Table 1. Fundamental characteristics of the test material

Chemical Compositions (wt %)

C	Si	Mn	P	S	Ni	Cr	N
0.05	0.78	1.21	0.02	0.001	9.5	18.7	0.04

Mechanical Property

	Proof Stress	Tensile Strength	Elongation	Hardeneness
Room Temp.	275MPa	608MPa	64 %	163Hv
550 C	127MPa	382MPa	39 %	----

Table 2. Cyclic deformation test conditions

T (℃) \ Δε (%)	0.3	0.5	0.7	1.0	1.4	2.0
200	○	○	○	○	○	○
400	○	○	○	○	○	○
550	○	○	○	○	○	○
650	○	○	○	○	○	○

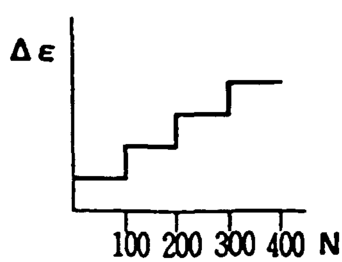

T: Temperature

Δε: Total Strain Range

$\dot{\varepsilon}=0.1\%/sec$

Table 3. Creep deformation test conditions

T (℃) \ σ (MPa)	110	130	240	280
550			○	○
650	○	○		

T: Temperature

σ: Stress

Table 4. Cyclic crack growth test conditions

T (℃) \ Δσ (MPa)	240	300	400	500
200				O
400			O	
550	O	O	O	O
650			O	

T: Temperature
Δσ: Nominal Stress Range
(Fully Reverse Loading)
Frequency 0.5Hz

Table 5. Creep crack growth test conditions

T (℃) \ σ (?a)	TBD	TBD	200	250
550			O	O
650	O	O		

T: Temperature
σ: Nominal Stress

Table 6. Schematic representation of the through-wall crack growth tests under stress-controlled creep-fatigue loading

t_H (hr) / T (℃)	1/6	1	5
550	O	O	O

T : Temperature
t_H : Hold Time
$\Delta\sigma$=500MPa (Fully Reverse Loading)

Table 7. Schematic representation of the through-wall crack growth tests under displacement-controlled creep-fatigue loading

$\dot{\varepsilon}_t$ (%/sec) / T (℃)	0.1	0.00167	0.000167
550	O	O	O

T : Temperature

$\dot{\varepsilon}_t$: Strain Rate for Tension-Going

$\dot{\varepsilon}_c$ =0.1%/sec : Strain Rate for Compression-Going

$\Delta\varepsilon$=0.8%

ORNL-DWG 89-14975

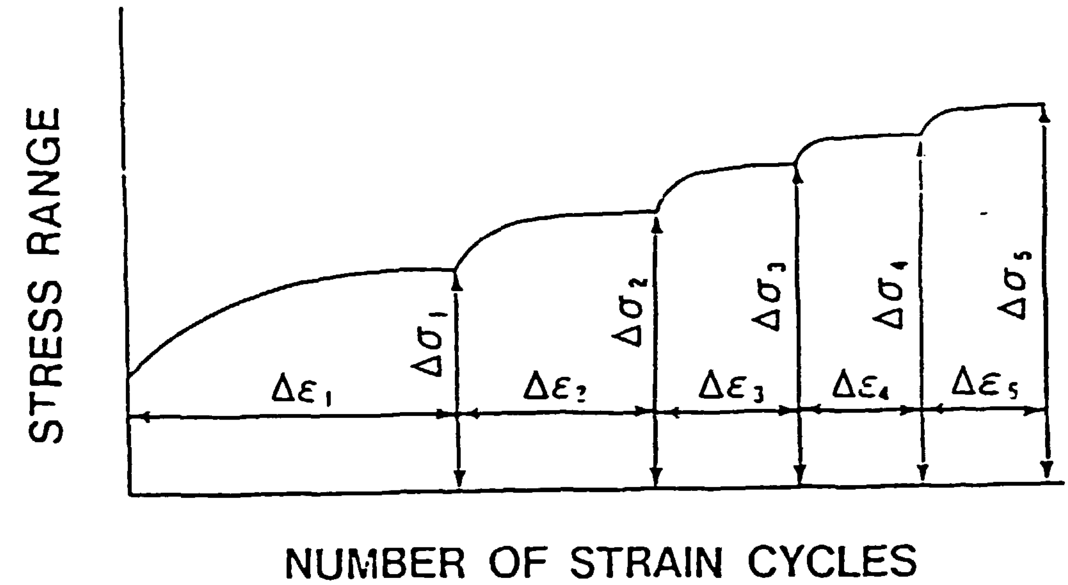

(a). Strain range step-up procedure.

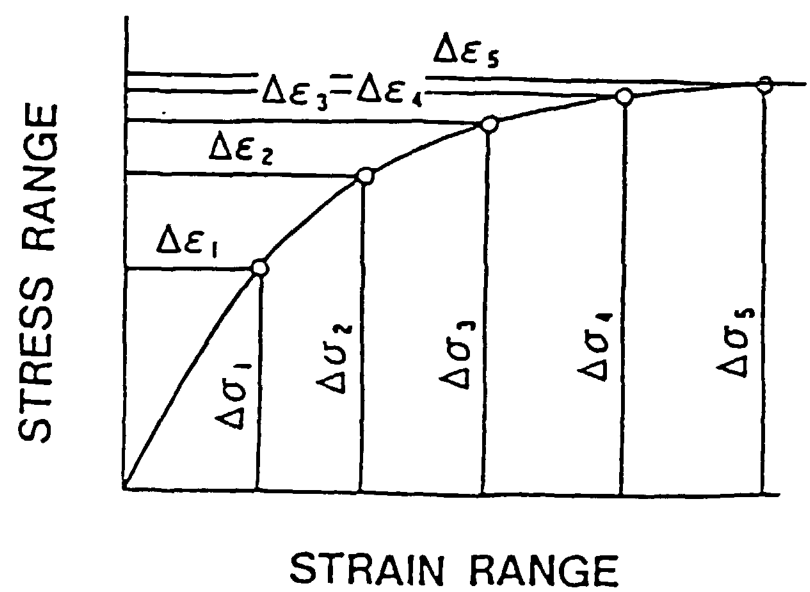

(b). Stress range vs strain range diagram.

Fig. 1. Strain range step-up procedure used for construction of cyclic stress-strain curve.

ORNL-DWG 89-14976

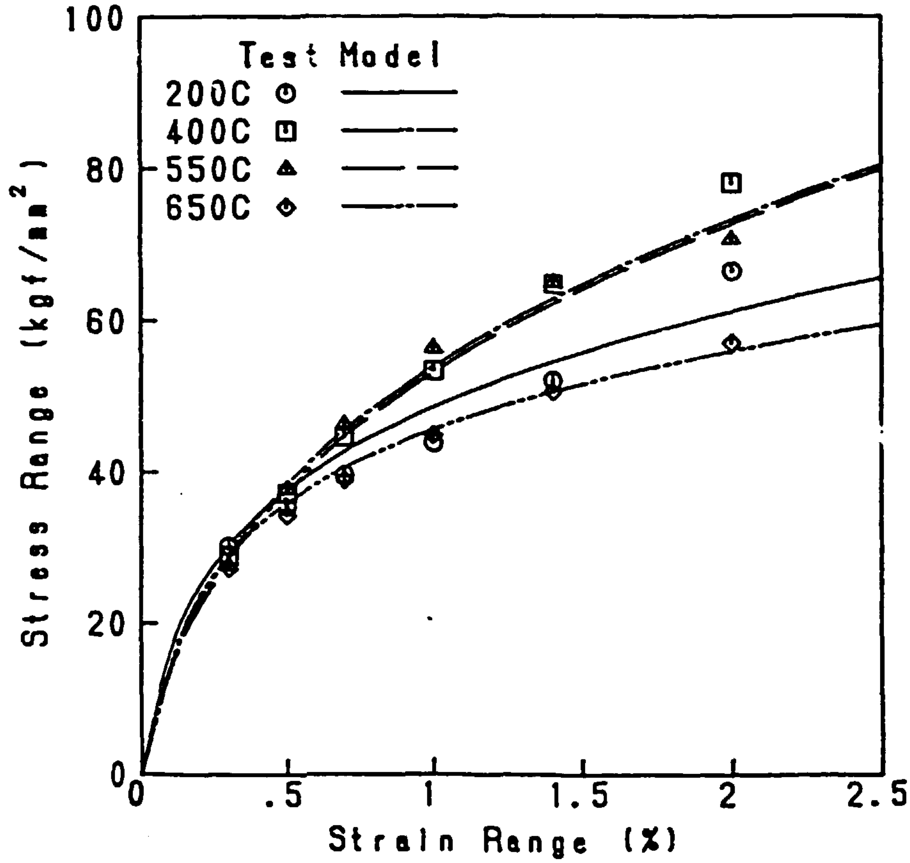

Fig. 2. Strain range - stress range relation.

ORNL-DWG 14977

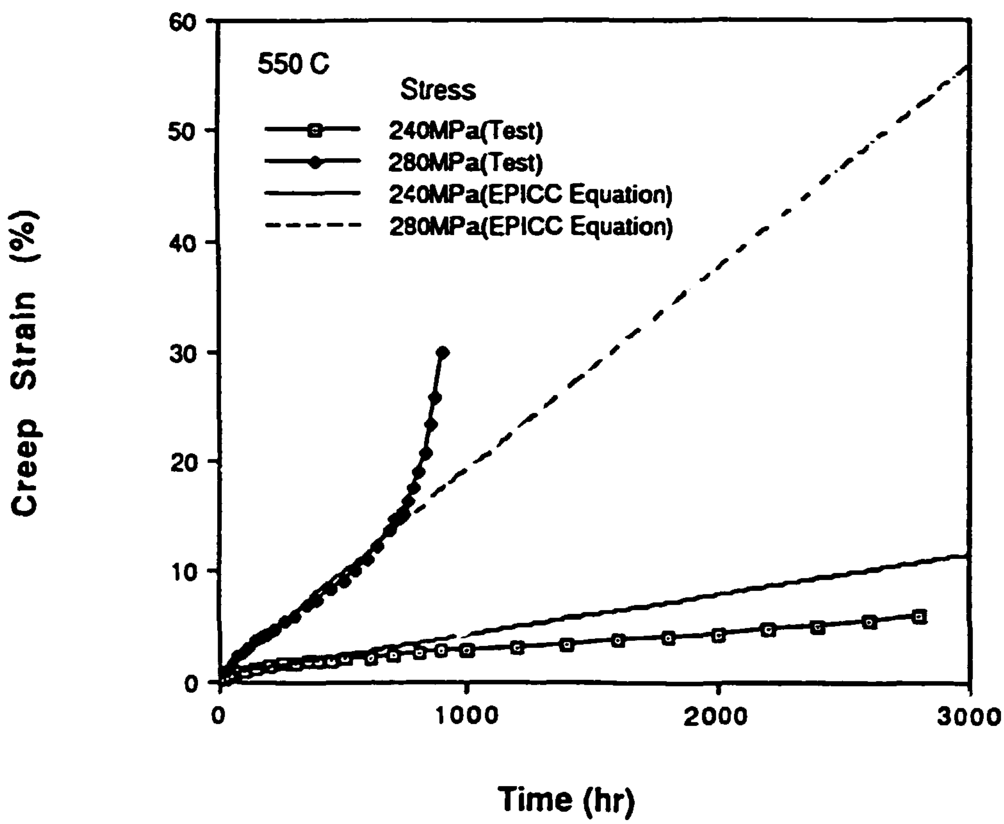

Fig. 3. Creep curves at 550°C.

ORNL-DWG 89-14978

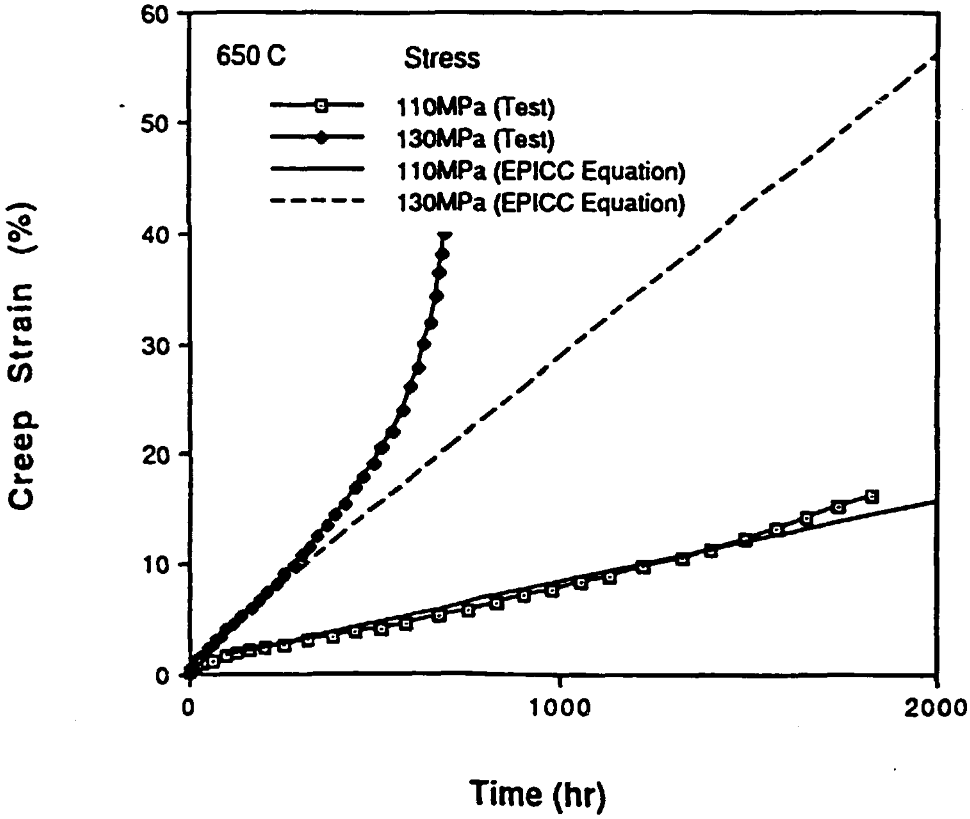

Fig. 4. Creep curves at 650°C.

ORNL-DWG 89-14979

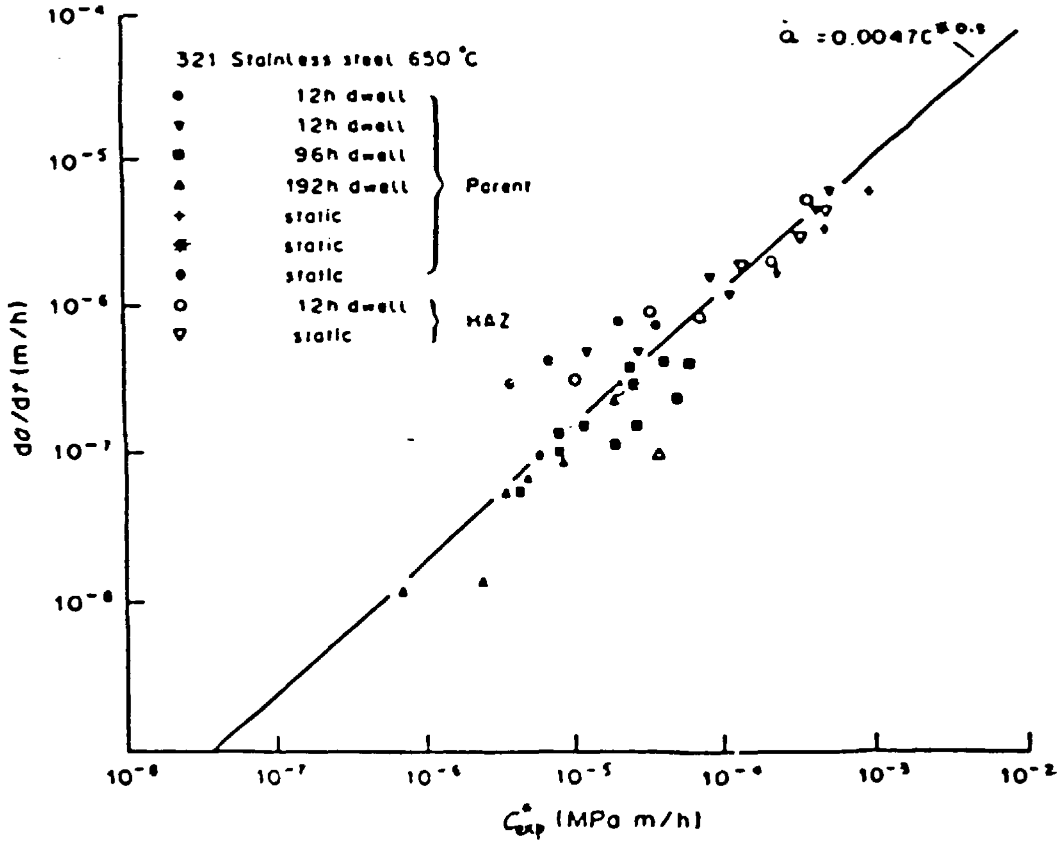

Fig. 5. Creep crack growth response of aged type 321 stainless Steel and HAZ at 650°C. Comparison of cyclic and static data.

ORNL-DWG 89-14980

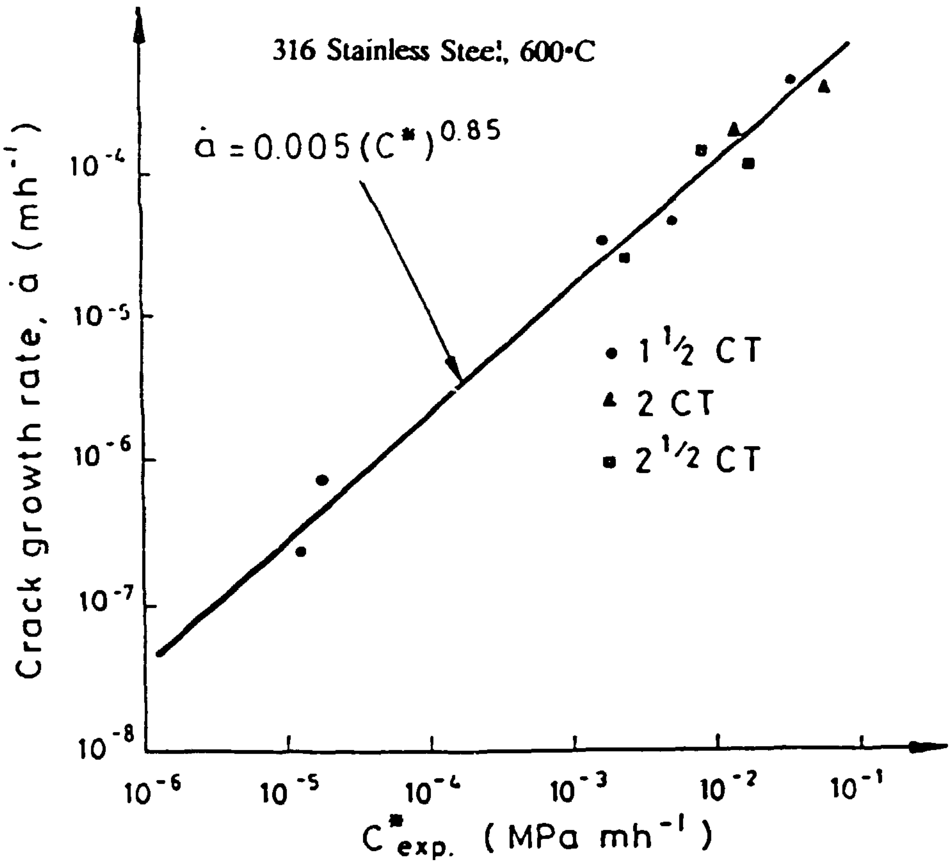

Fig. 6. Creep crack growth response of type 316 stainless steel at 600°C for CT specimens of various thickness.

ORNL-DWG 89-14981

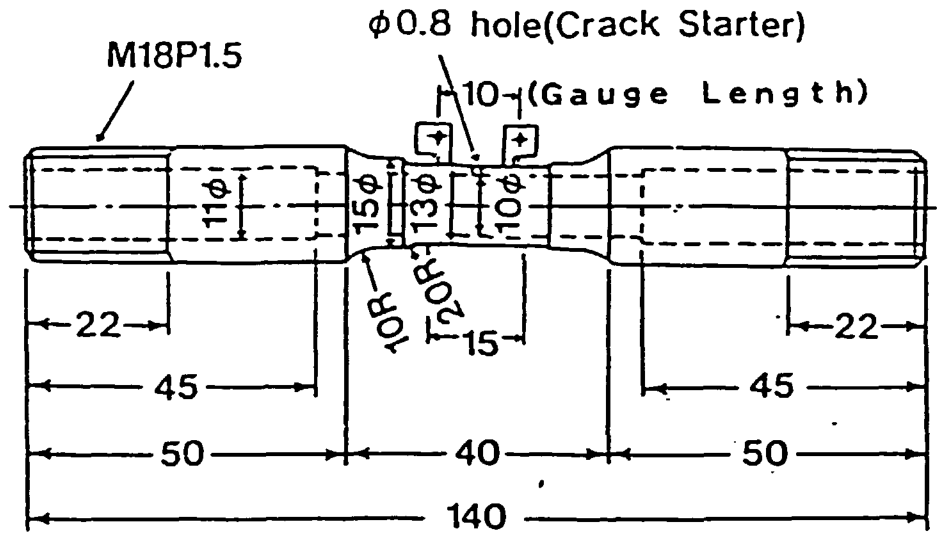

Fig. 7. Crack growth test specimen (unit: 1 mm).

ORNL-DWG 89-14982

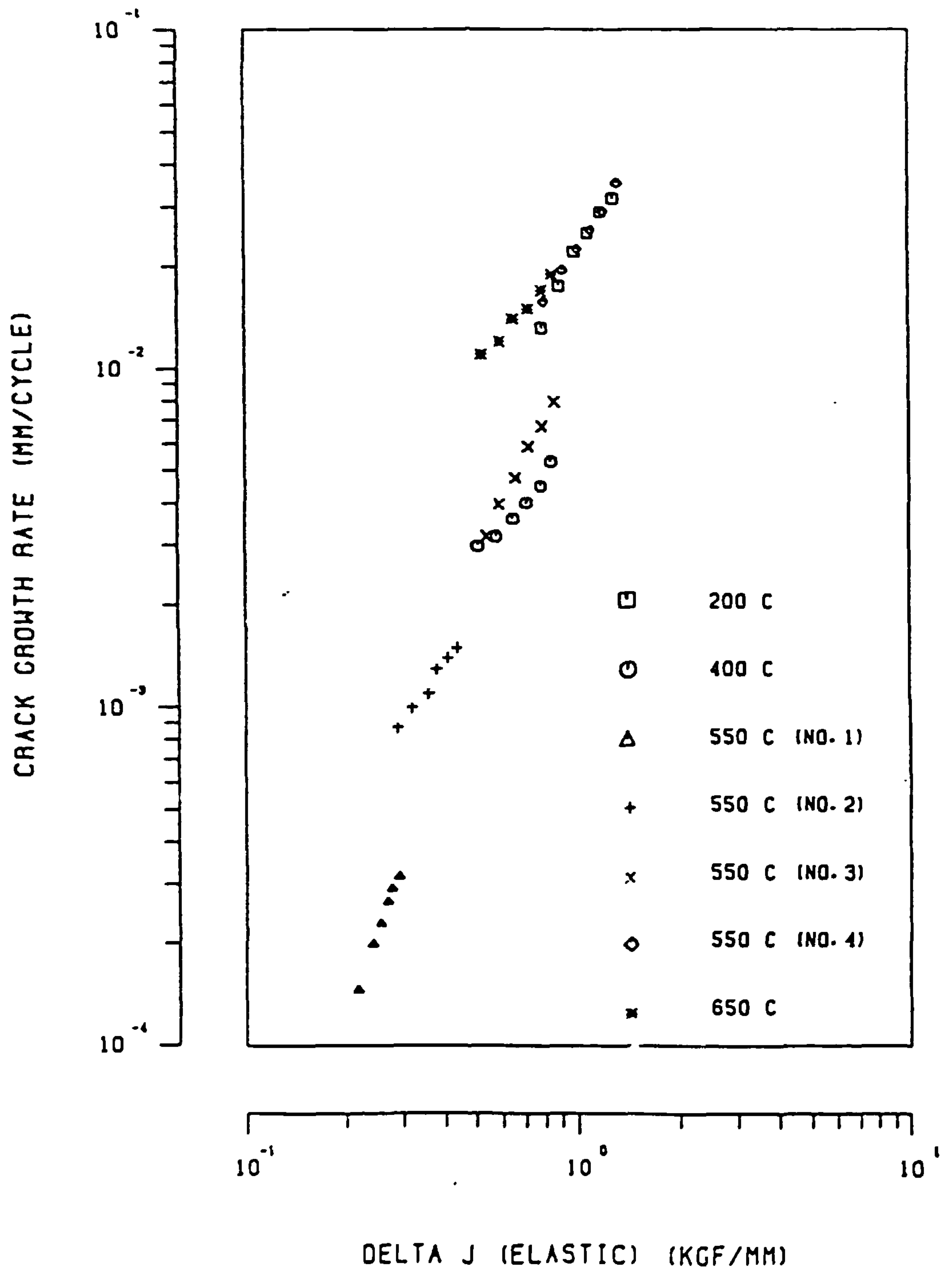

Fig. 8. Correlation between crack growth rate and elastic J-integral range.

ORNL-DWG 89-14983

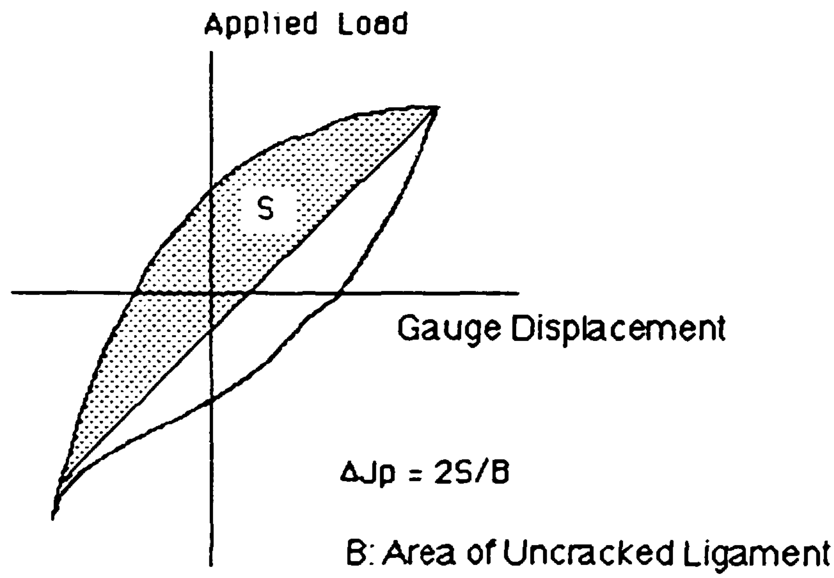

Fig. 9. Experimental determination of elastic-plastic fatigue J-integral range.

ORNL-DWG 89-14984

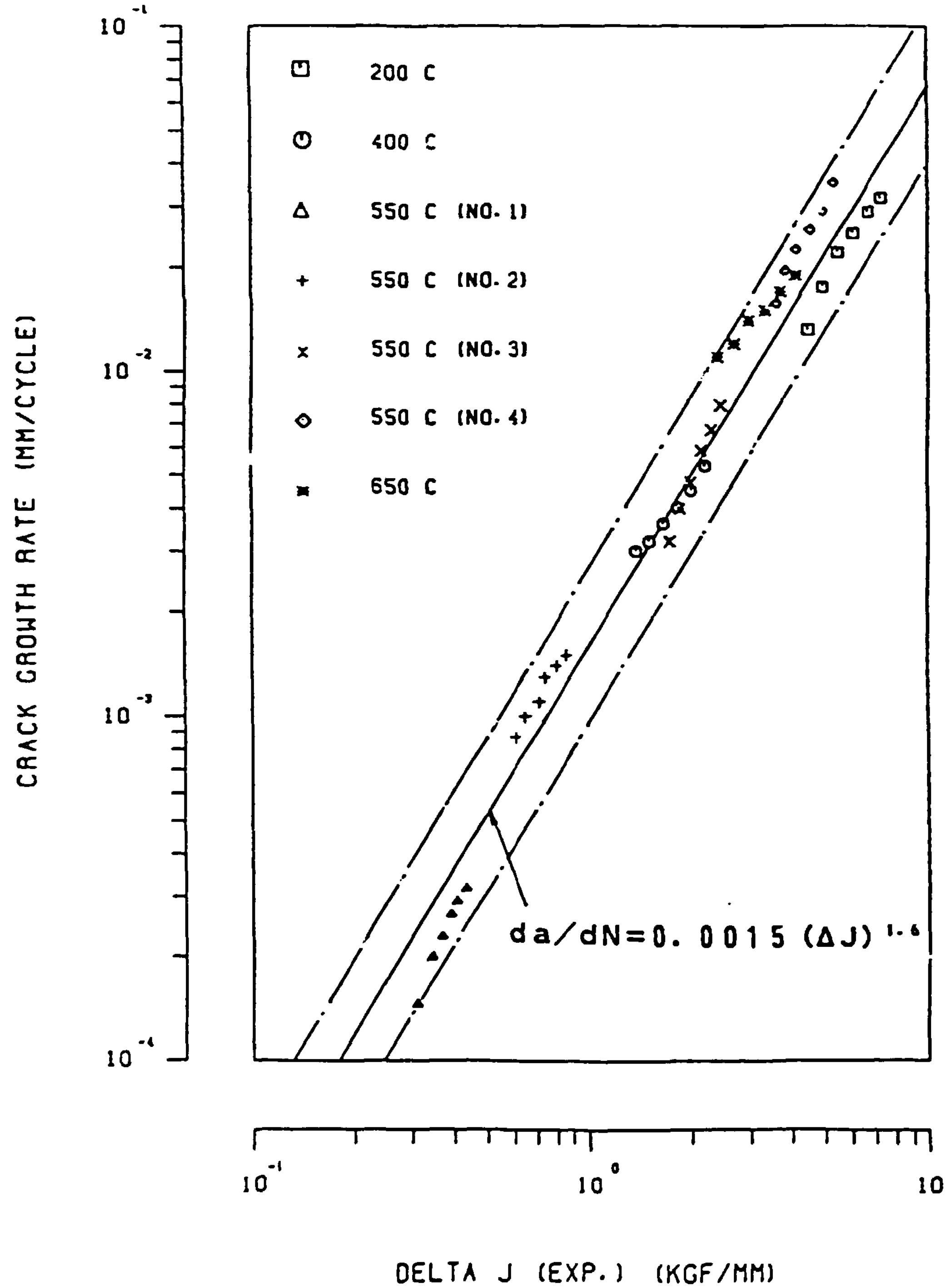

Fig. 10. Correlation between crack growth rate and elastic-plastic J-integral range.

ORNL-DWG 89-14985

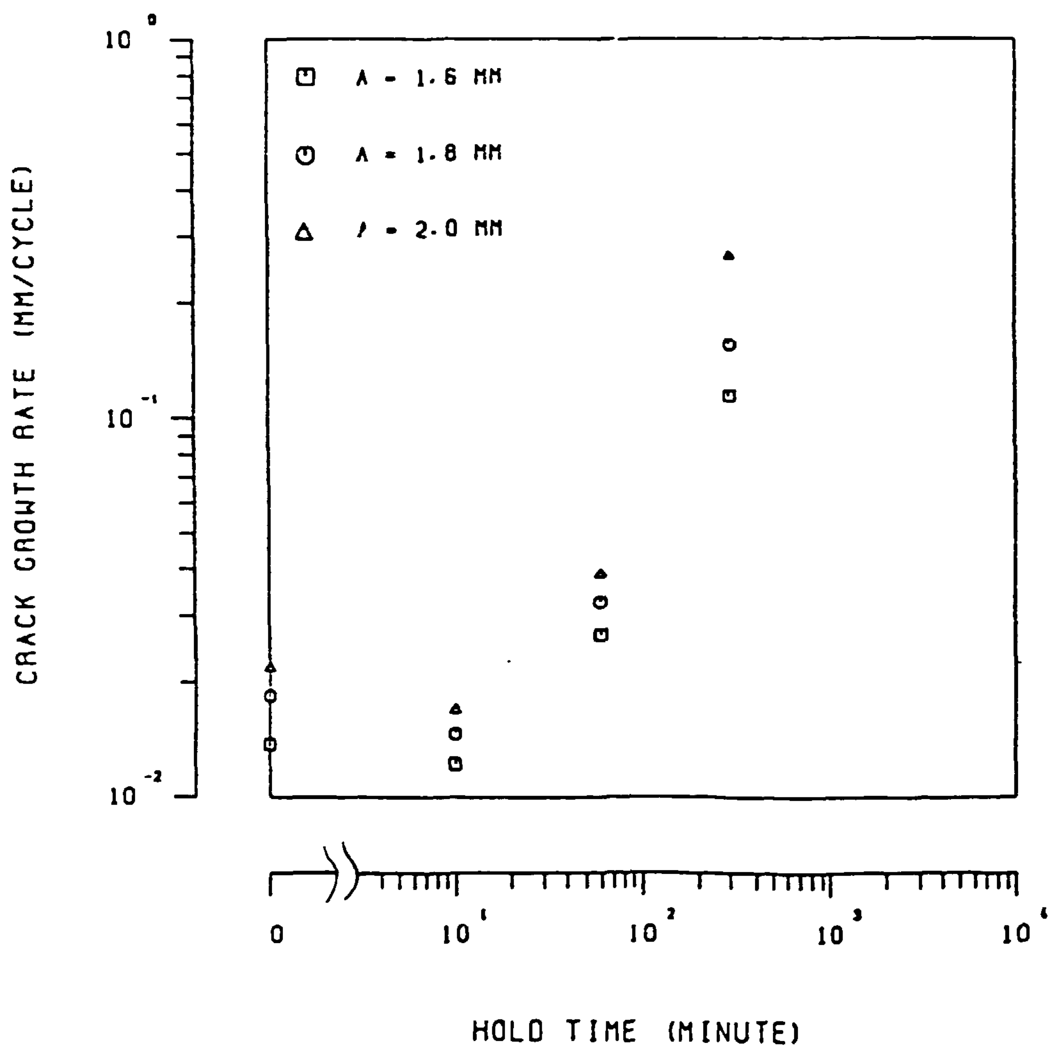

Fig. 11. Dependence of crack growth rate on stress hold time.

ORNL-DWG 89-14986

$$\Delta J_f = (\Delta K)^2 / E + 2 S_1 / B$$

$$\Delta J_c = S_2 / B$$

B : Area of Uncracked Ligament

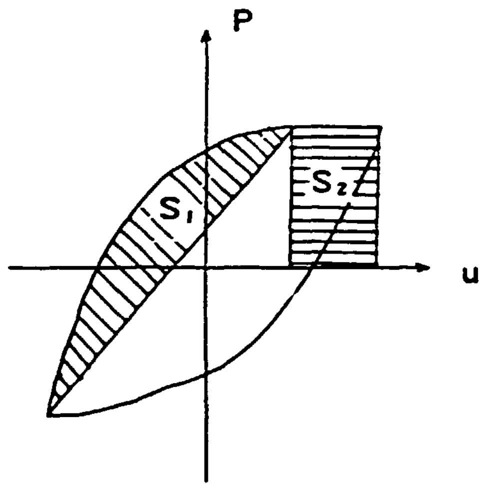

Fig. 12. Experimental determination of creep J-integral range.

ORNL-DWG 89-14987

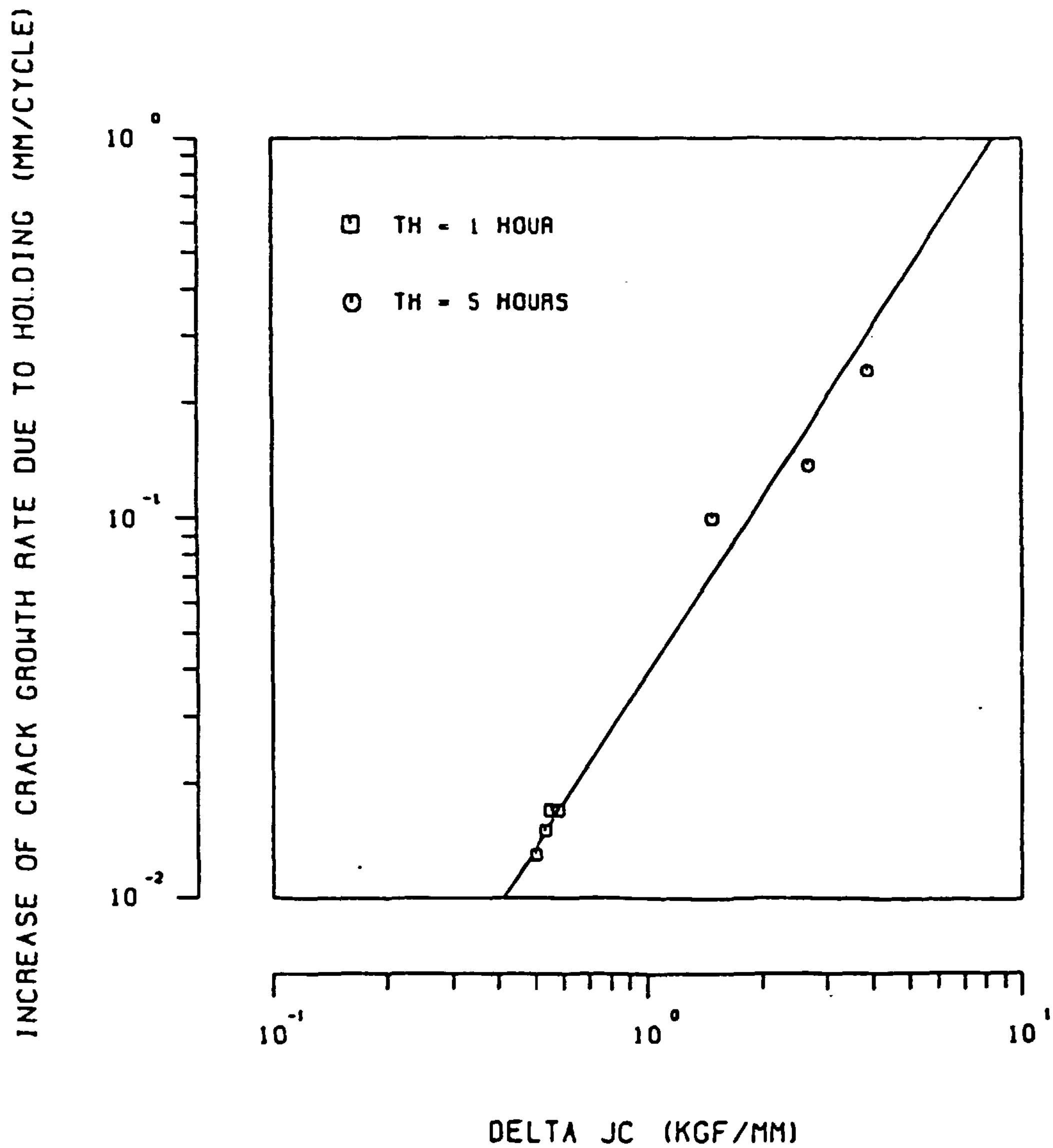

Fig. 13. Correlation between crack growth rate, increasing due to stress holds, and creep J-integral range.

ORNL-DWG 89-14988

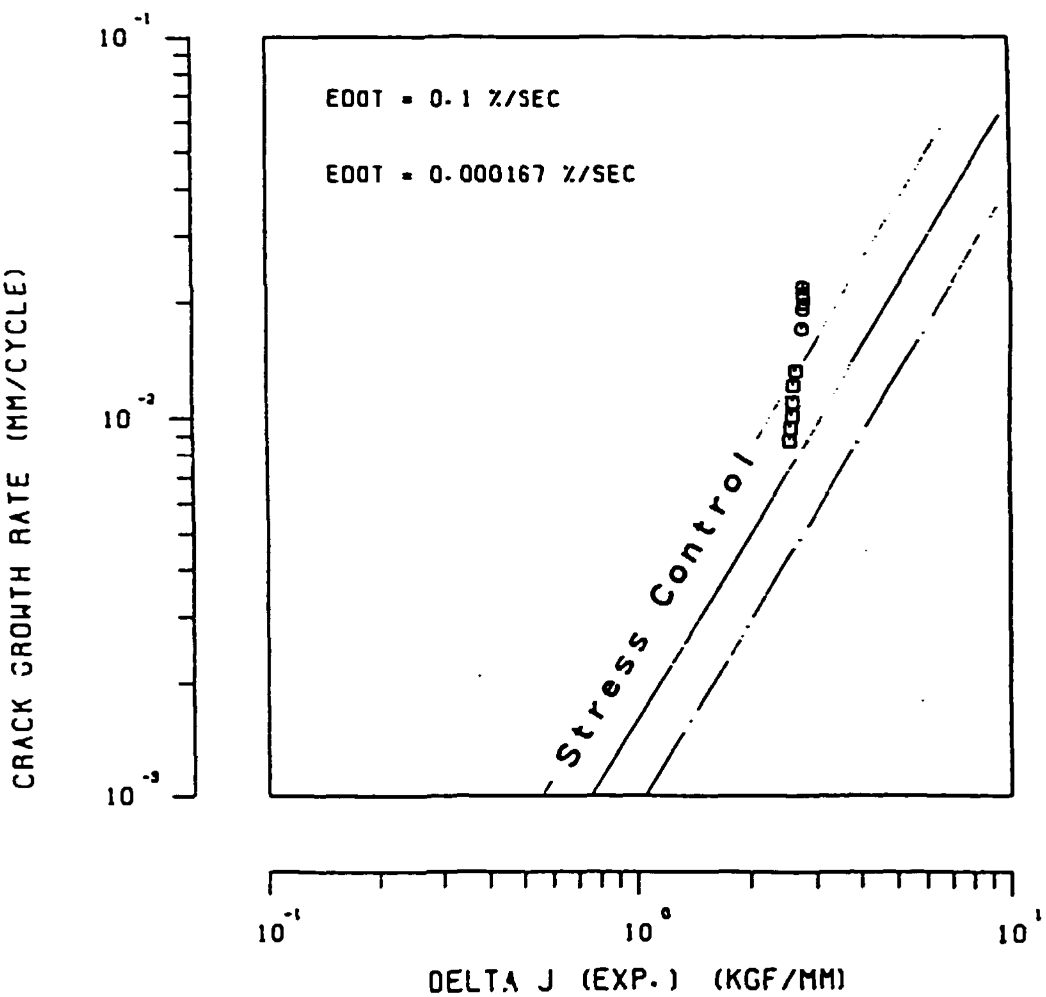

Fig. 14. Correlation between crack growth rate and fatigue J-integral range in displacement-controlled crack growth tests.

ORNL-DWG 89-14989

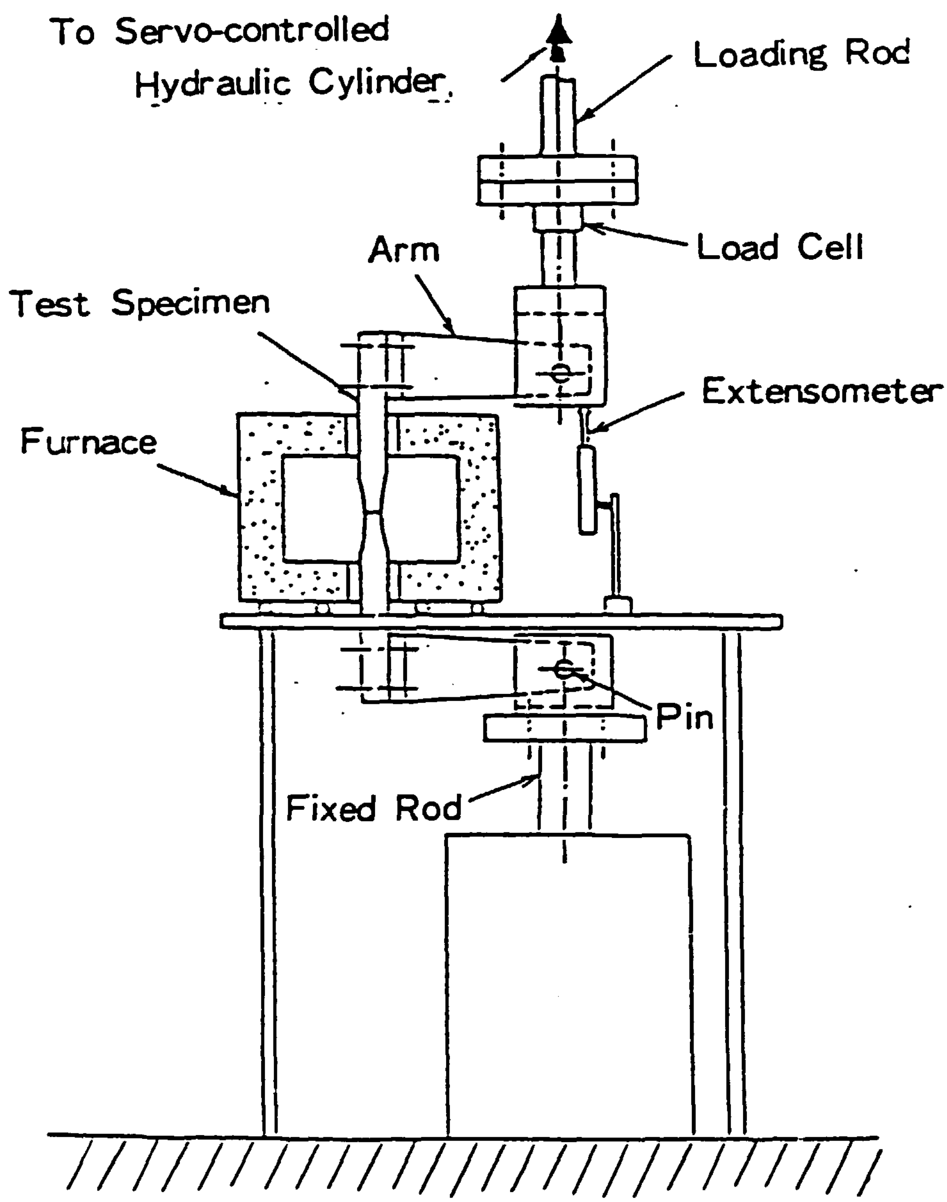

Fig. 15. Test apparatus for surface crack growth tests under mechanical loading.

ORNL-DWG 89-14990

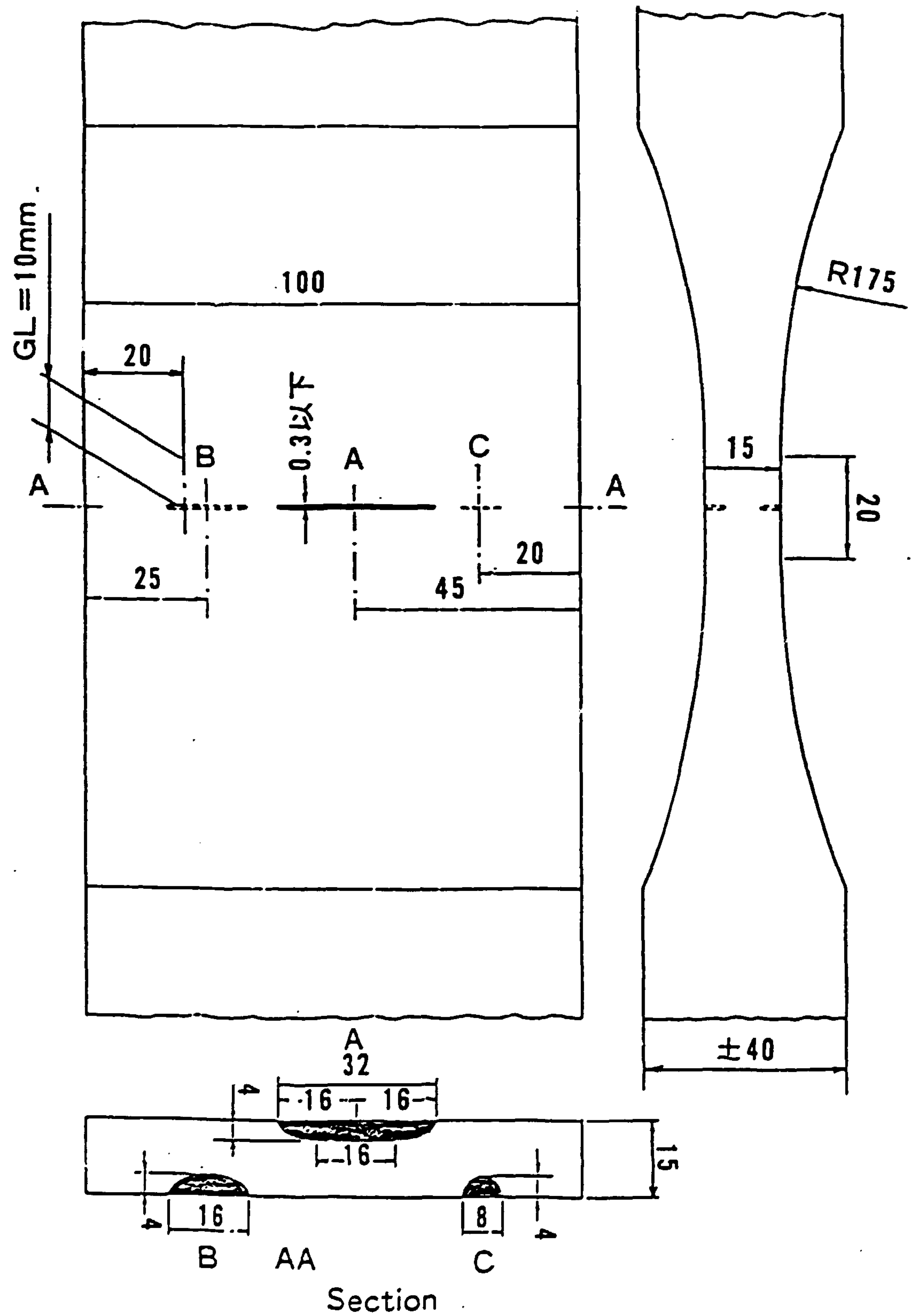

Fig. 16. Surface crack growth test specimen (unit: 1 mm).

ORNL-DWG 89-14991

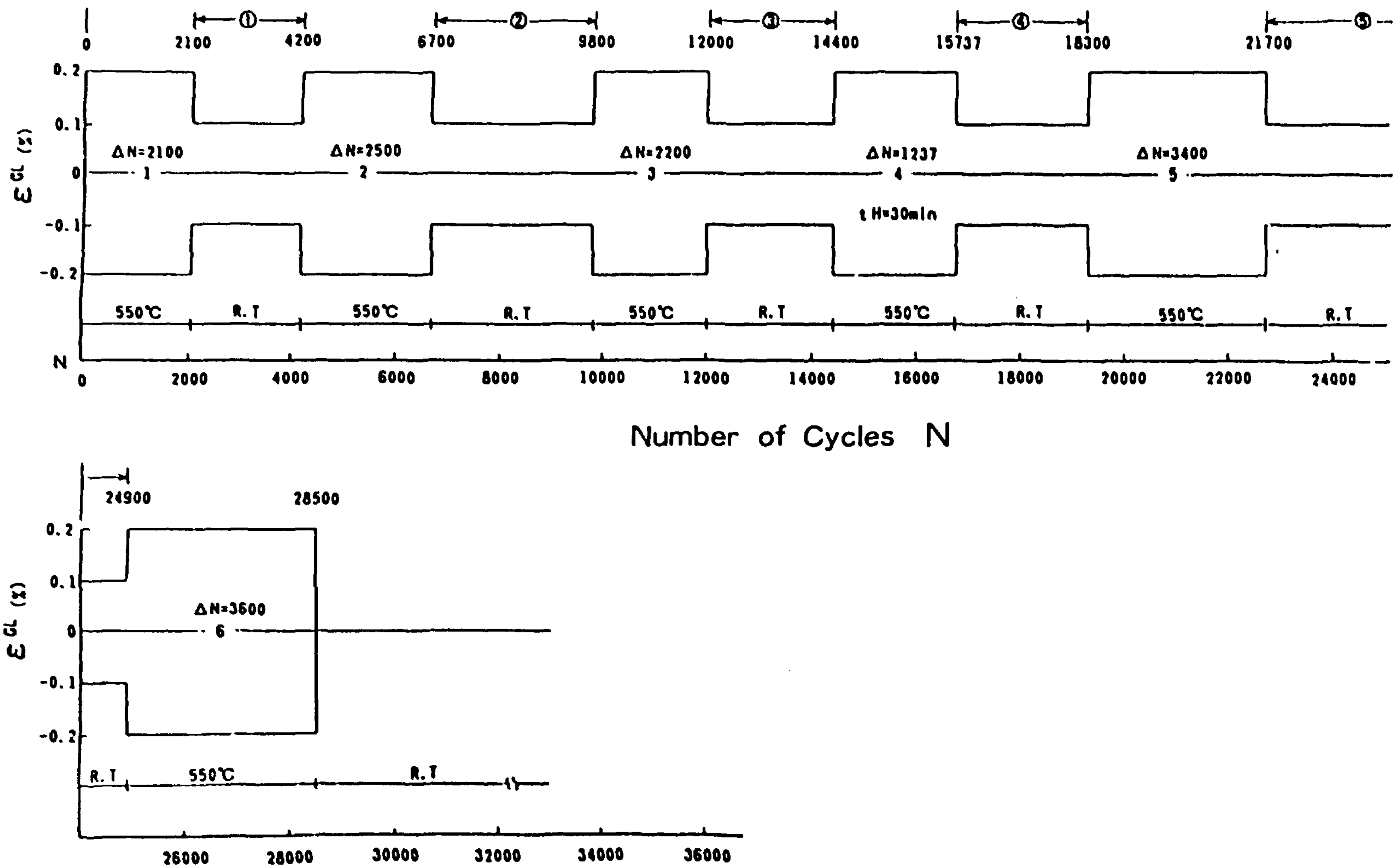

Fig. 17. Loading sequence for surface crack growth tests.

ORNL PHOTO 5485-89

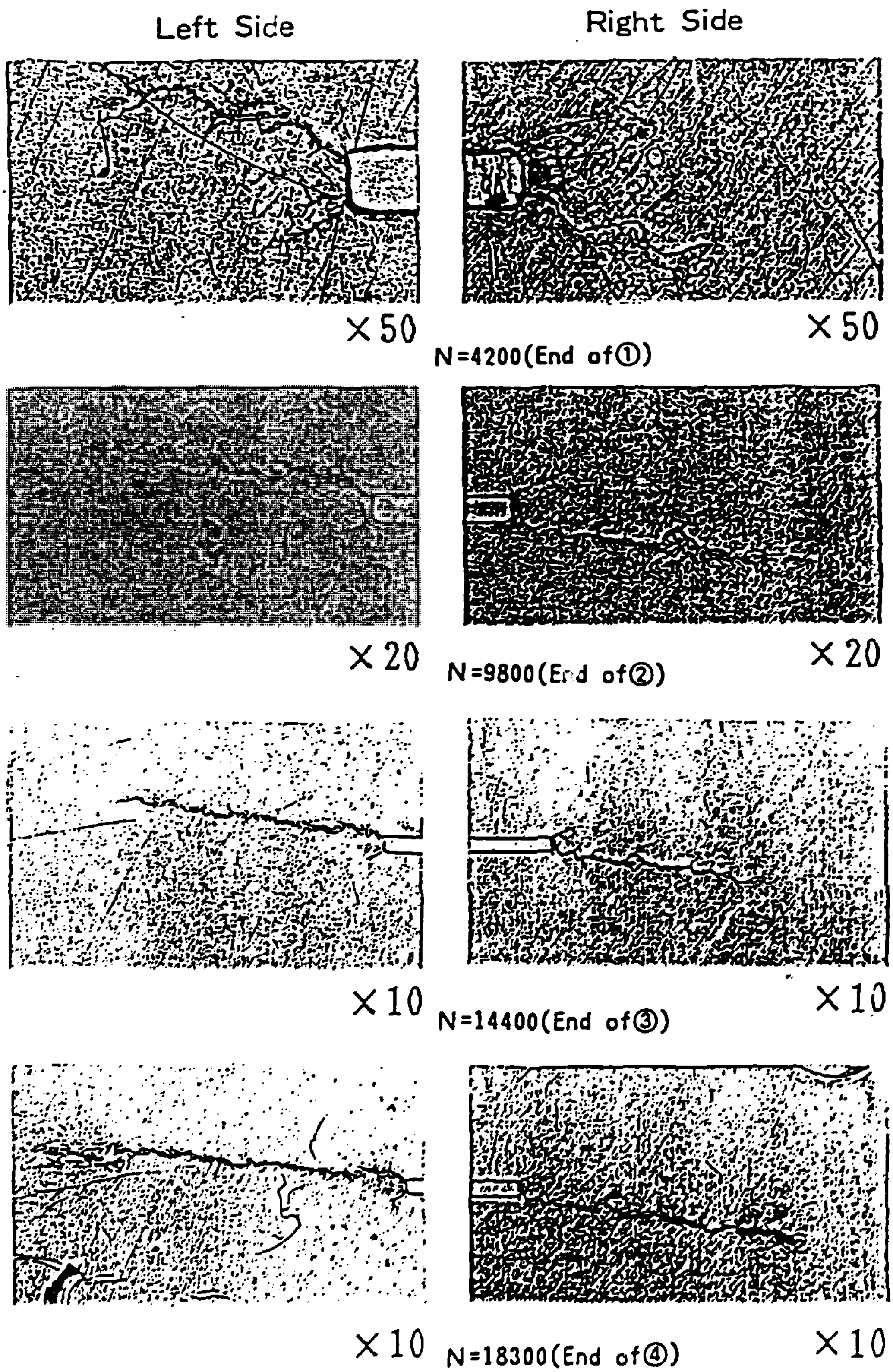

Fig. 18. Status of crack B observed on specimen surface.

ORNL PHOTO 5486-89

Crack A(a_o=4mm, $2c_o$=32mm)

Fig. 19. Fracture surface around crack A.

ORNL PHOTO 5487-89

Crack B(a_o=4mm, $2c_o$=16mm)

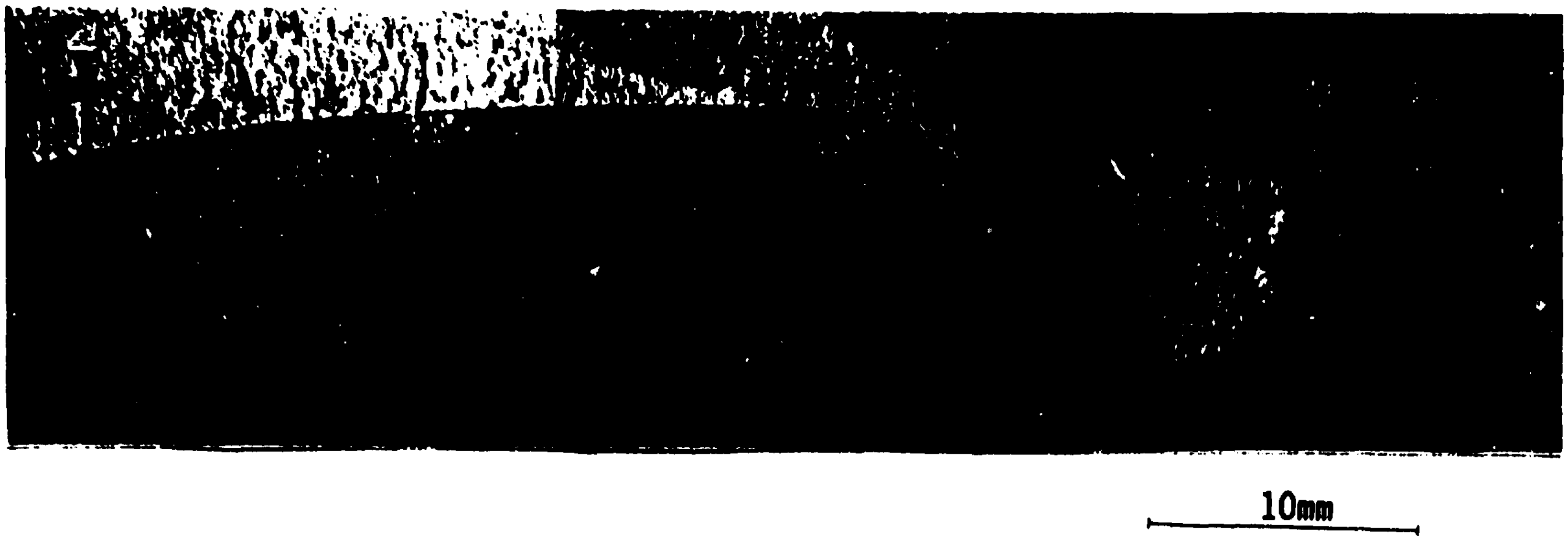

Fig. 20. Fracture surface around crack B.

ORNL PHOTO 5488-89

Crack C (a_o =4mm, $2c_o$ =8mm)

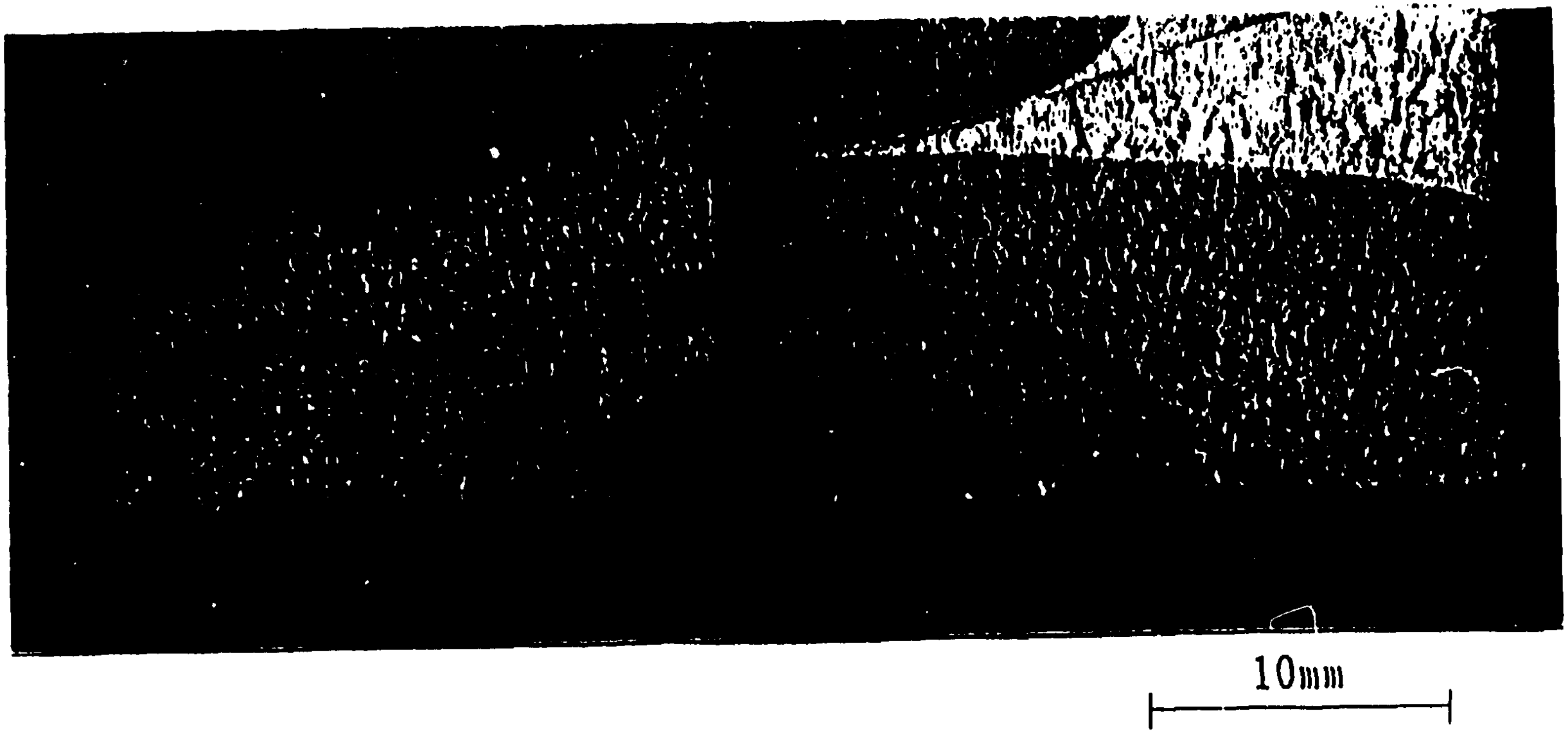

Fig. 21. Fracture surface around crack C.

ORNL-DWG 89-14992

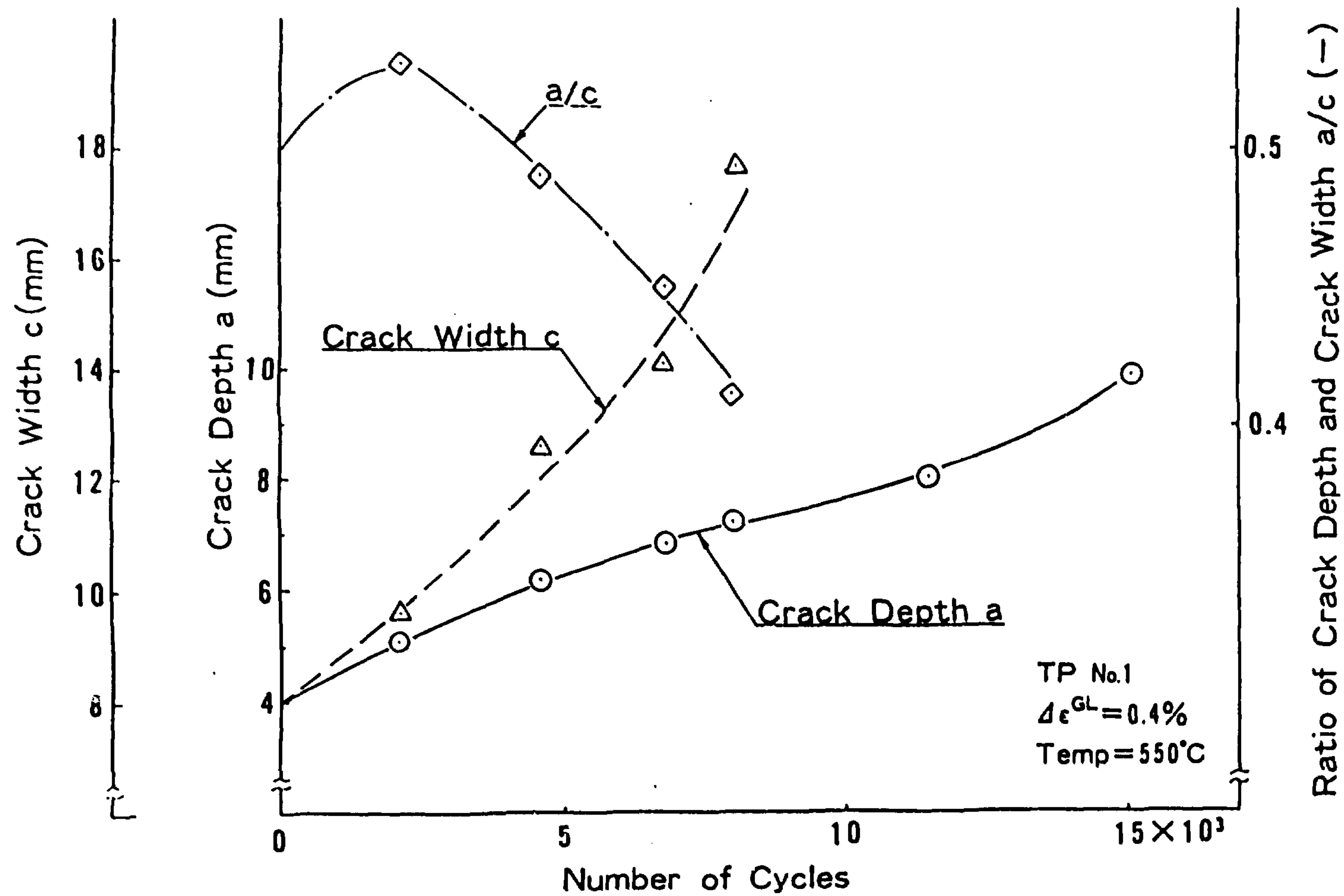

Fig. 22. Variations in depth and width for crack B.

ORNL-DWG 89-14993

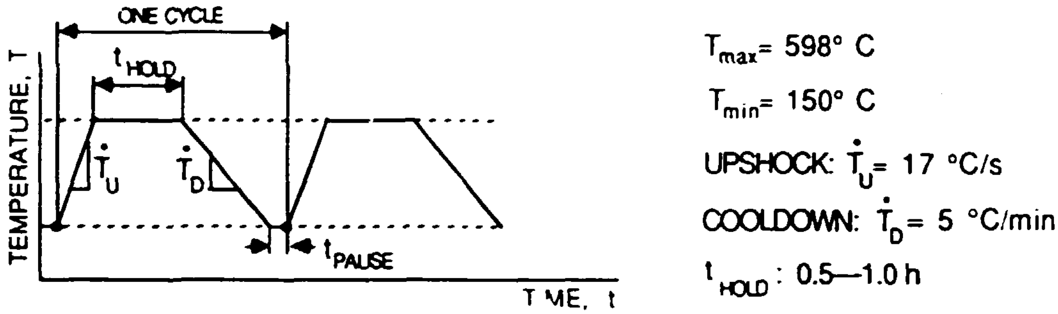

Fig. 23. EPRI thermal shock cycle.

ORNL-DWG 89-14994

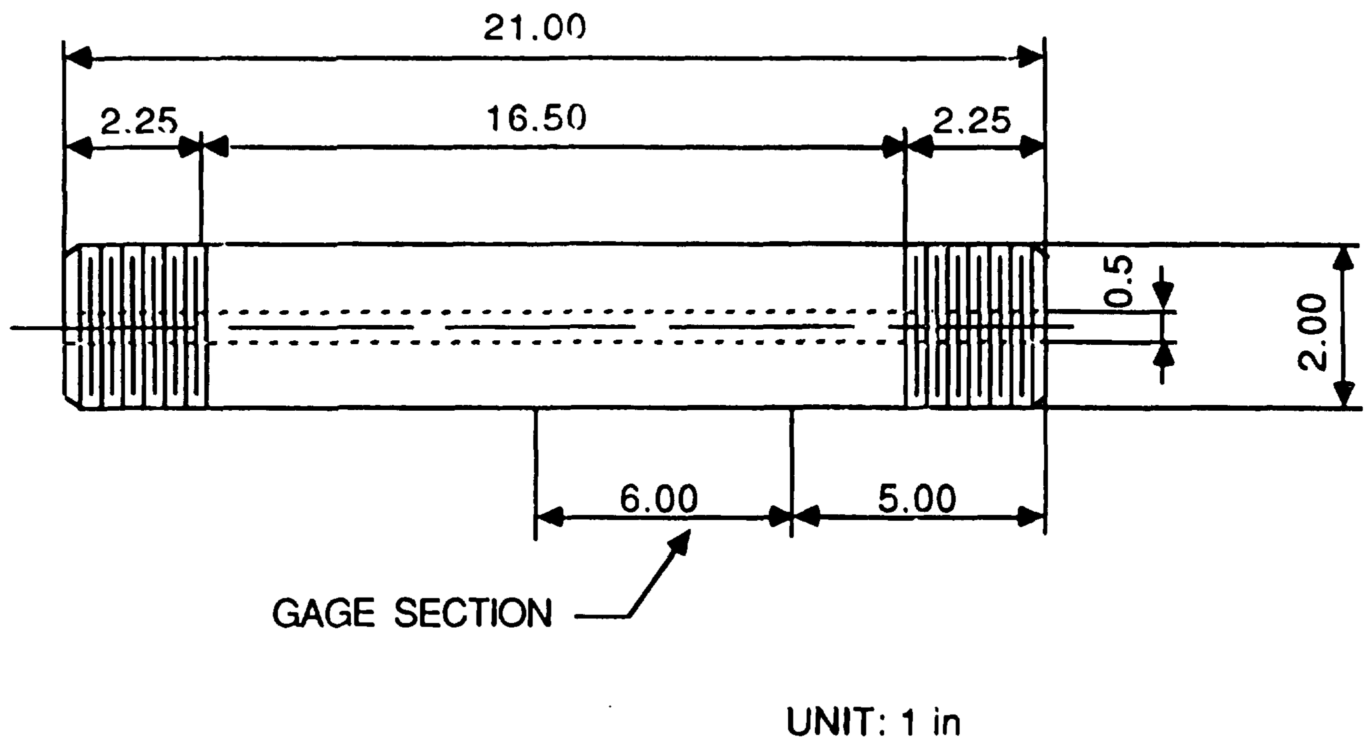

Fig. 24. Thick-walled cylindrical thermal shock specimen.

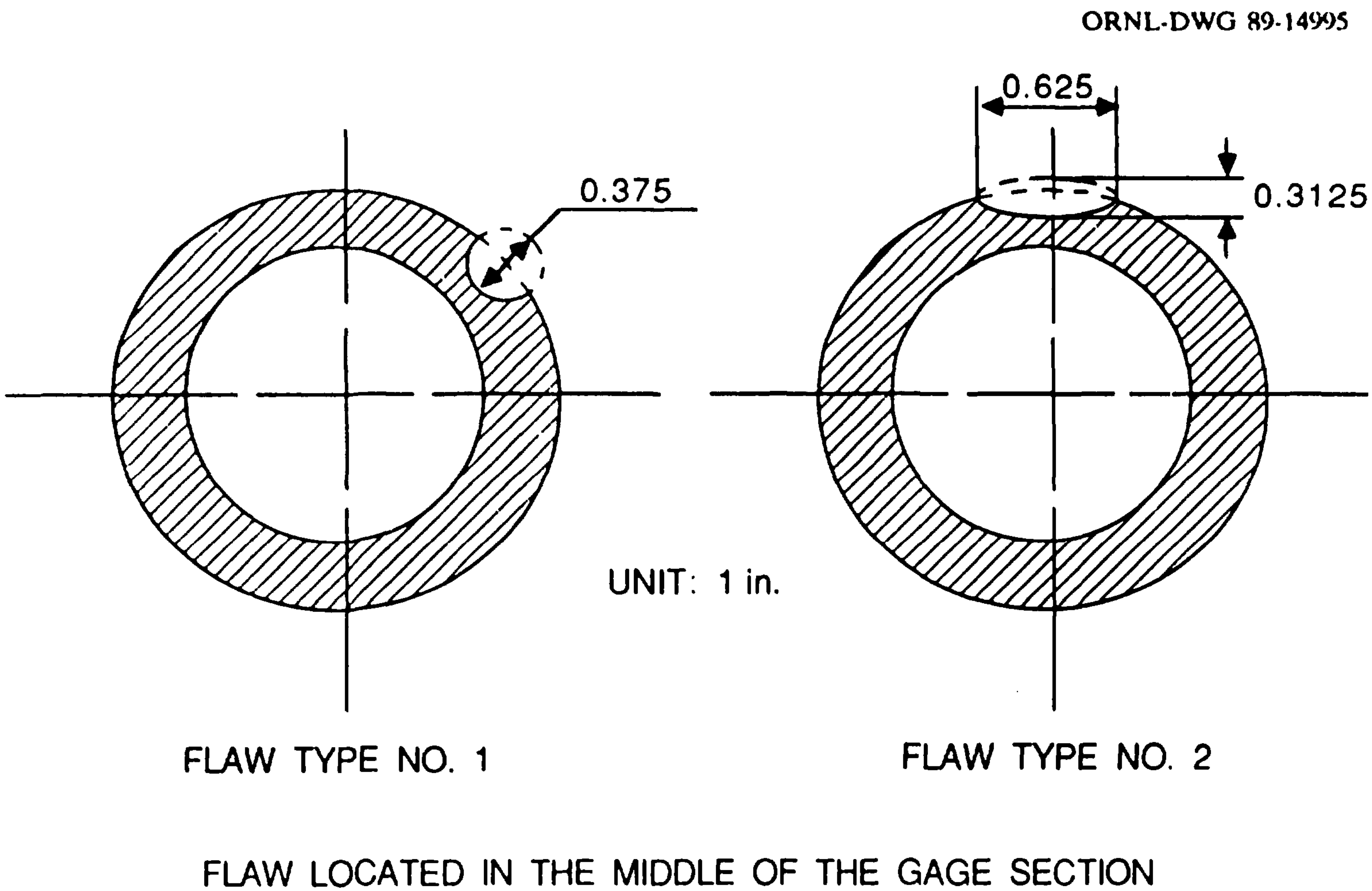

Fig. 25. Two types of circumferential flaws used for thick-walled cylindrical thermal shock specimens.

Fig. 26 Existing thermal shock facility

ORNL PHOTO 8174-89

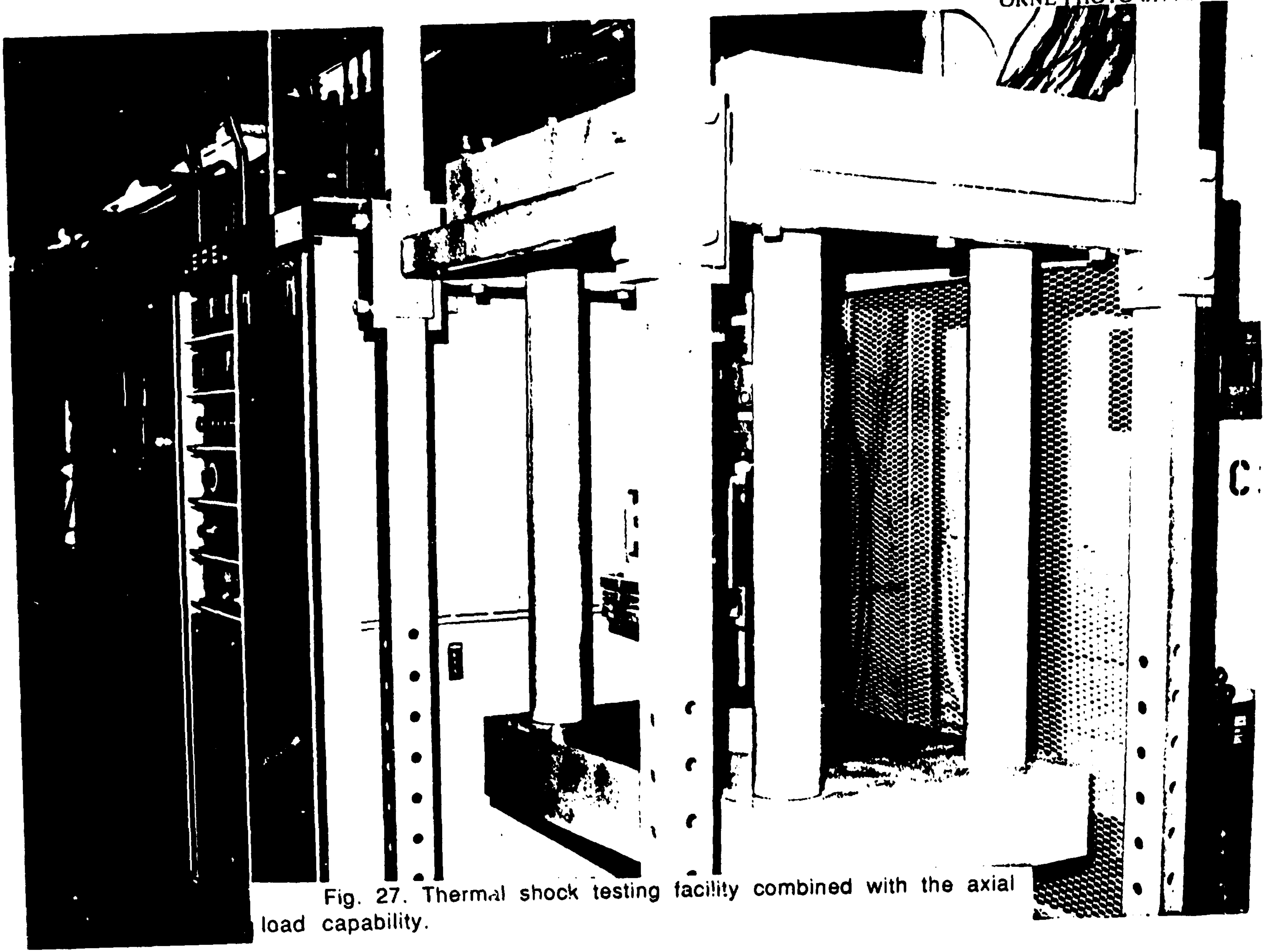

Fig. 27. Thermal shock testing facility combined with the axial load capability.

ORNL-DWG 89-14996

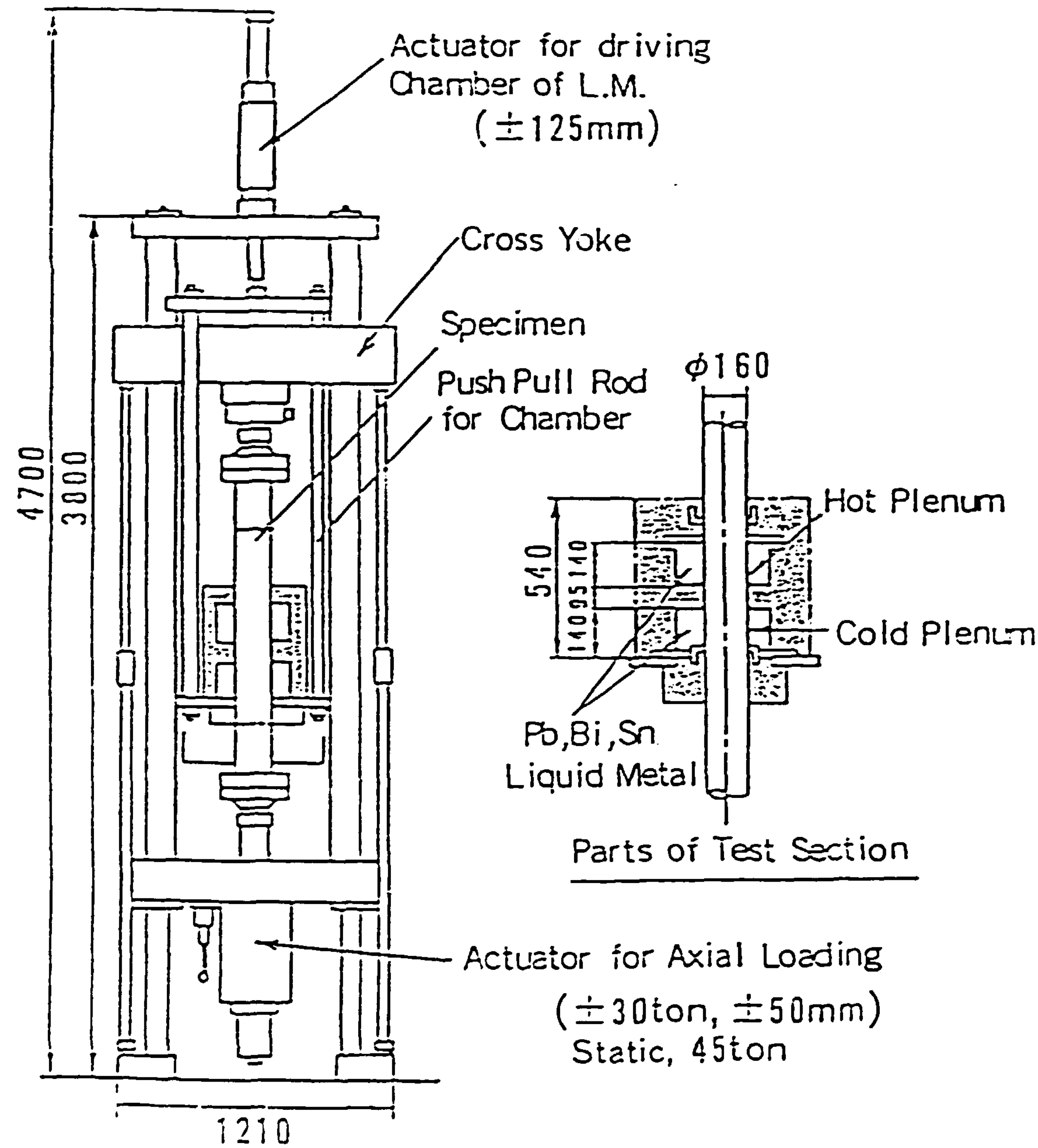

Fig. 28. Testing system for thermal shock tests of preflawed cylinders.

ORNL-DWG 89-14997

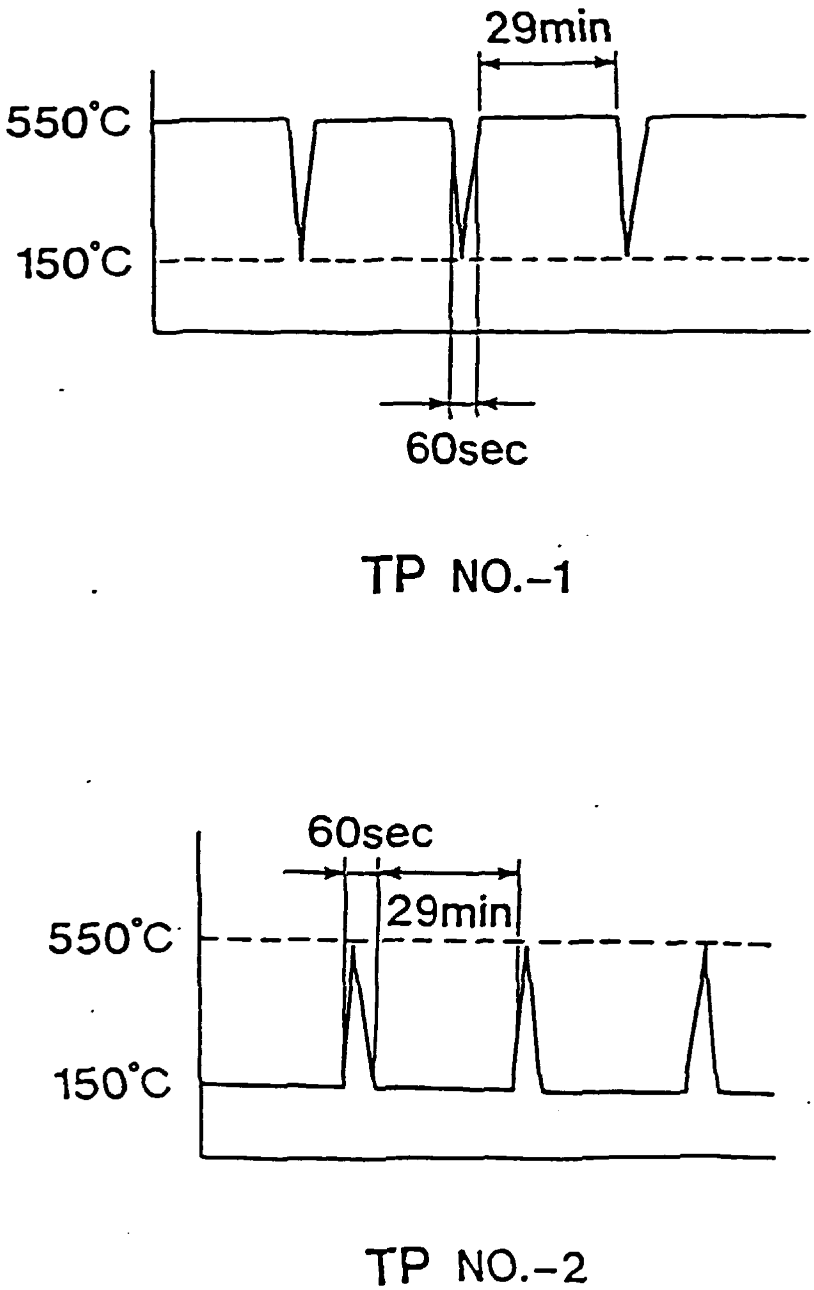

Fig. 29. Thermal loading applied to the outer surface of the cylindrical specimen near preflawed planes.

ORNL-DWG 89-14998

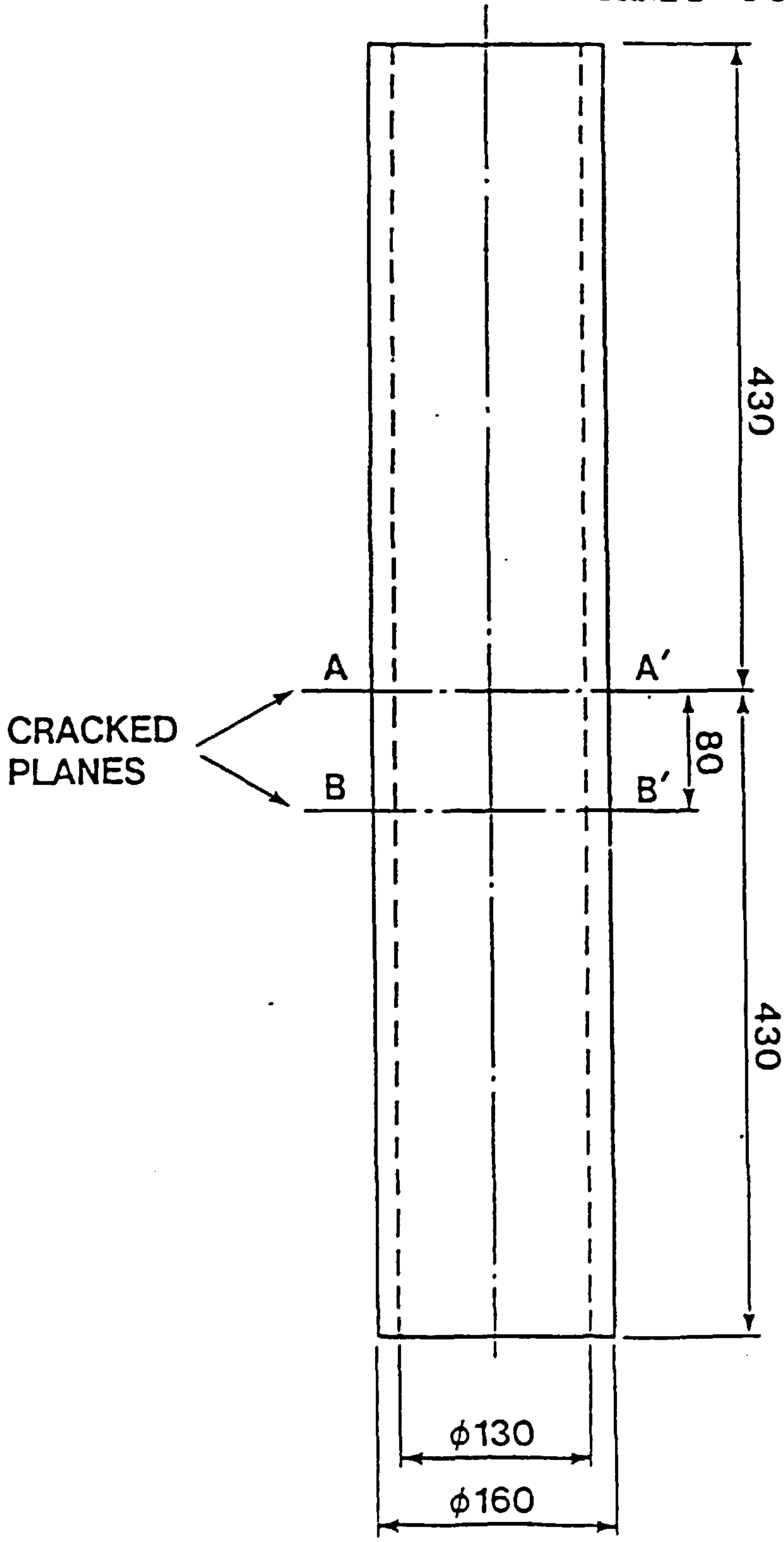

Fig. 30. Position of flaws in cylindrical specimens (unit: 1mm).

ORNL-DWG 89-14999

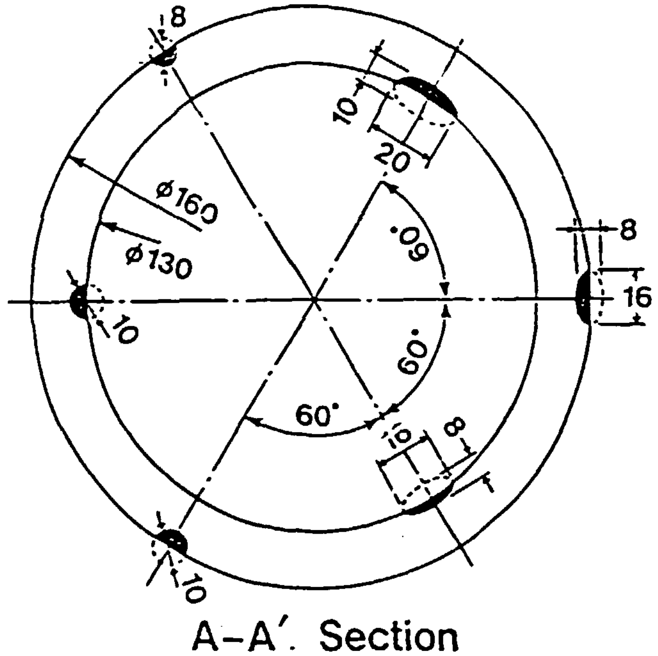

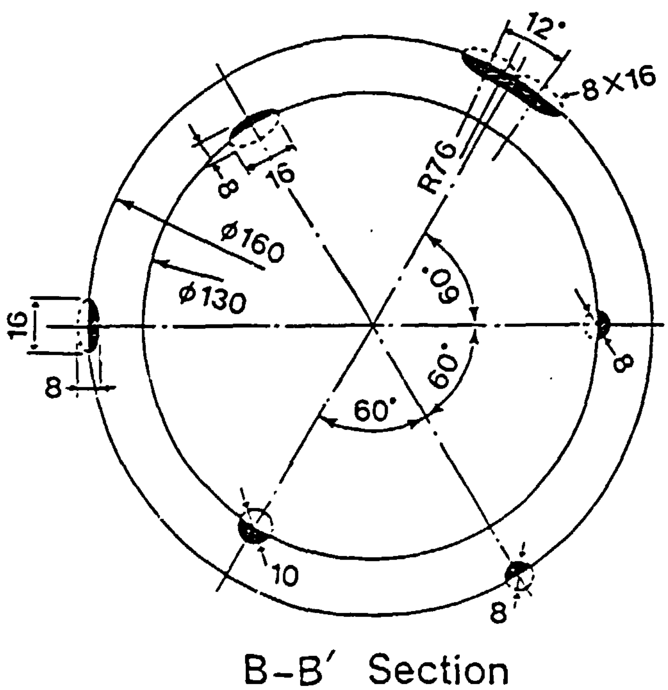

Fig. 31. Dimensions of flaws in two circumferential planes (unit: 1 mm).

ORNL-DWG 89-15000

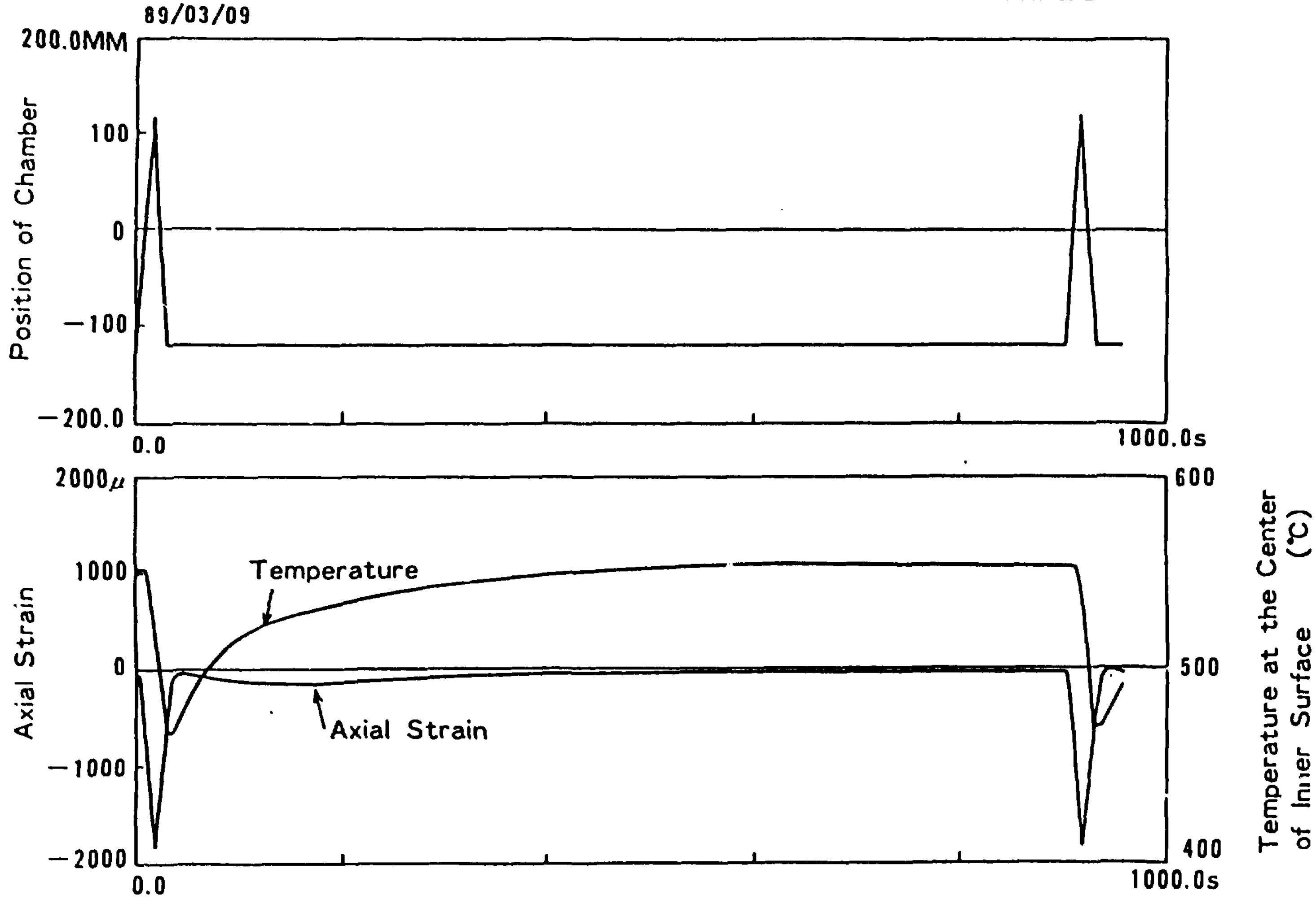

Fig. 32. Variation of temperature and axial strain at inner surface in the center of the specimen.

ORNL PHOTO 5489-89

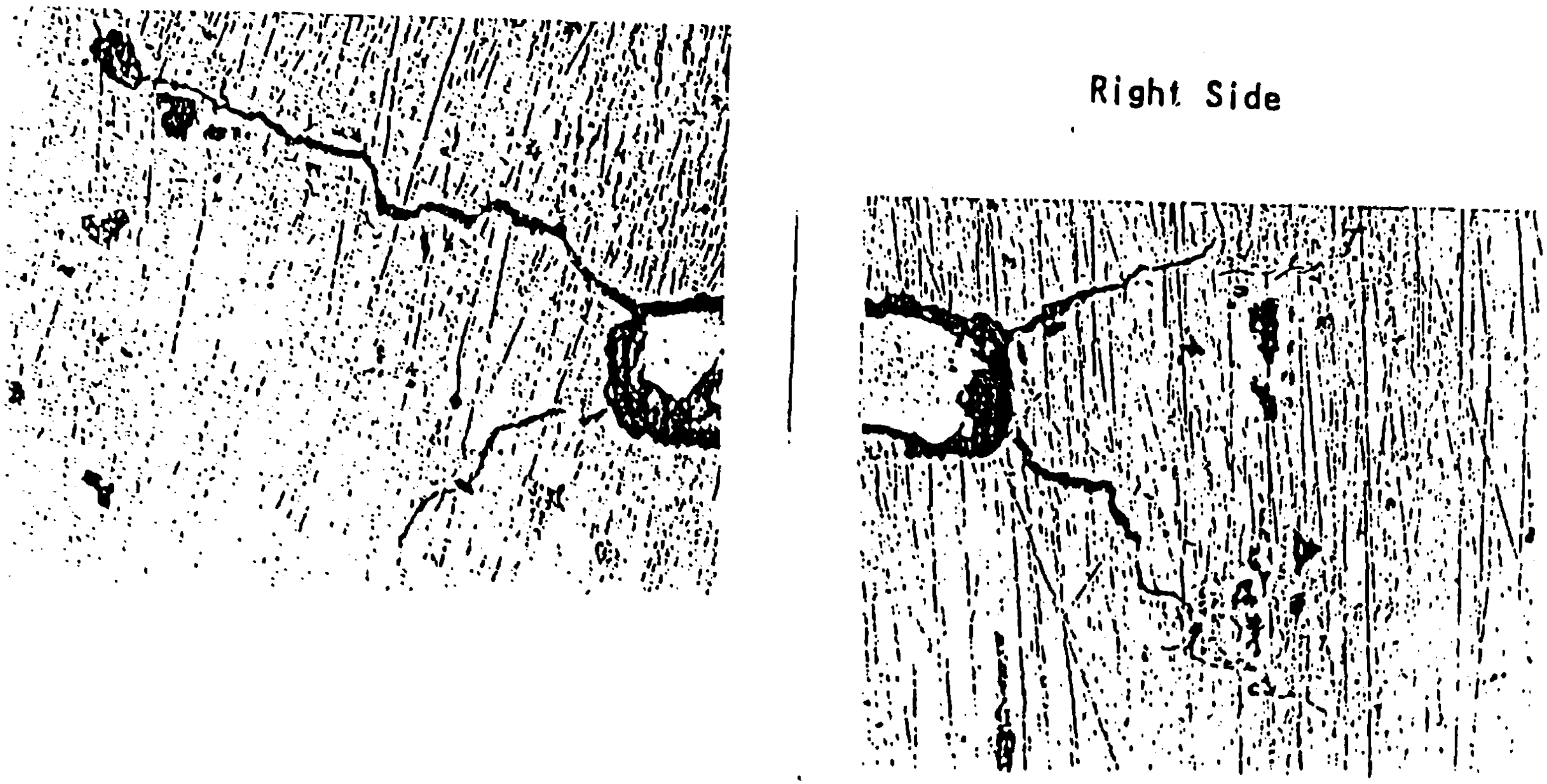

Outer Surface, Section B-B

Fig. 33. Observed crack growth originating from the flaw of least depth in section B-B.

ORNL-DWG 89-15001

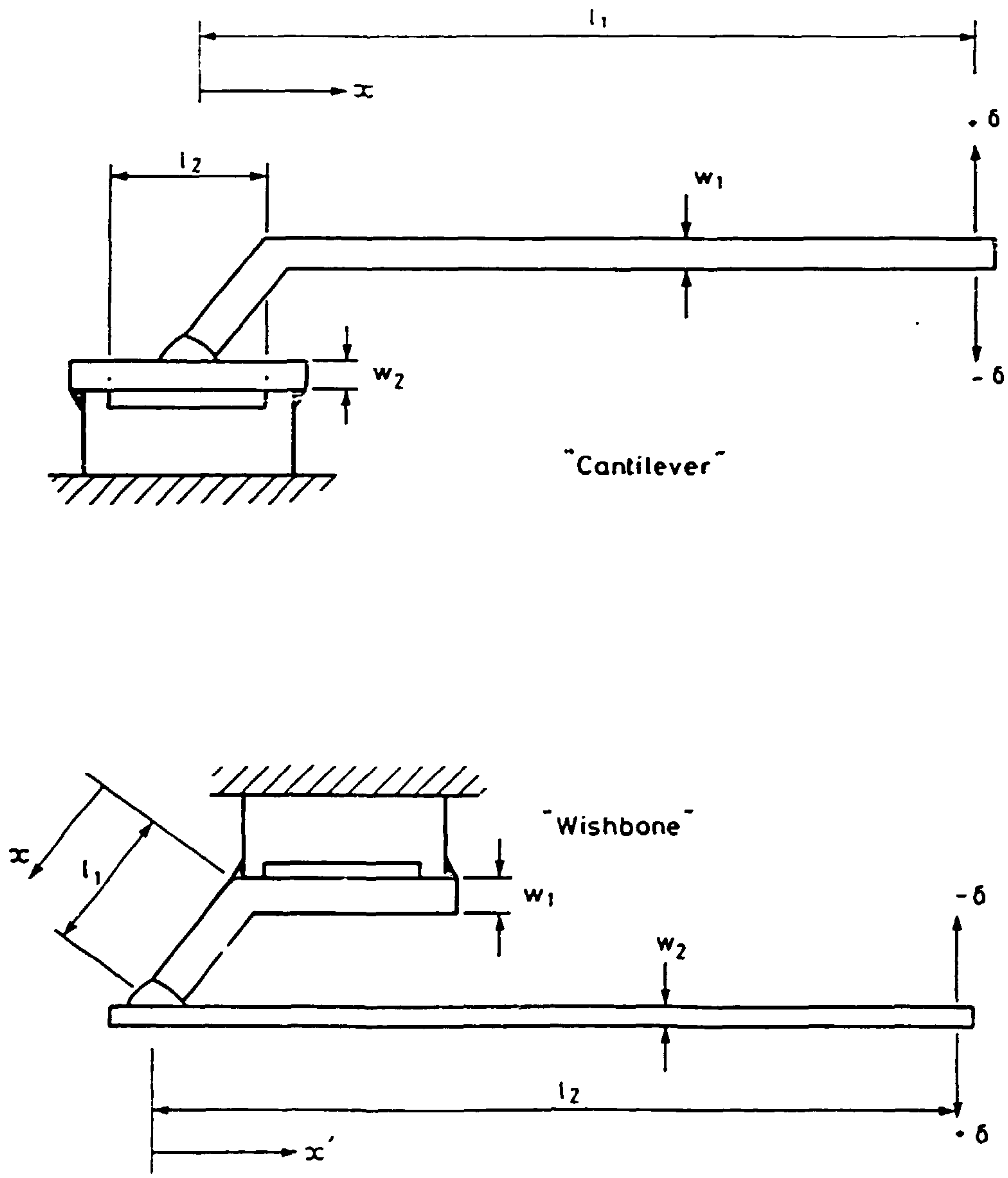

Fig. 34. Schematic of test specimen geometries.

ORNL-DWG 89-15002

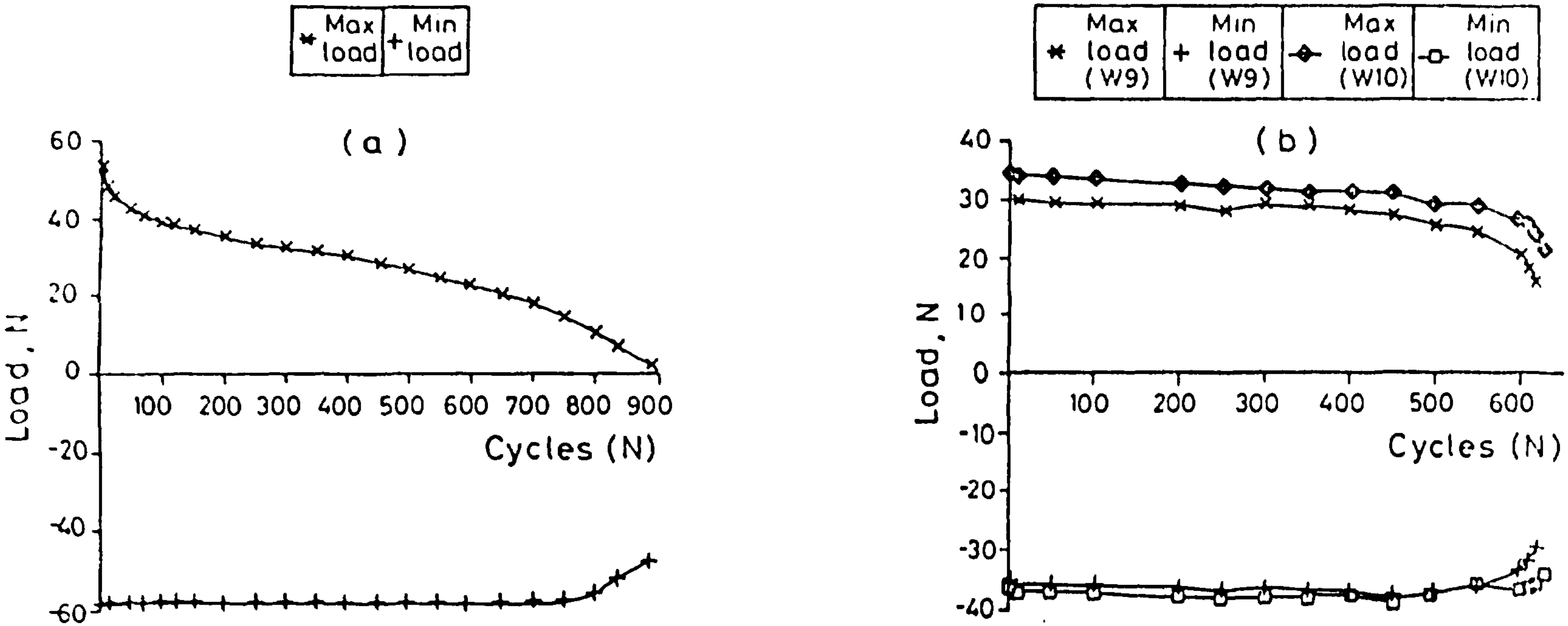

Fig. 35. Peak loads vs cycles behavior, experimental results.
(a) "Cantilever "specimen C5, (b) "wishbone" specimens W9 and W10.

ORNL-DWG 89-15003

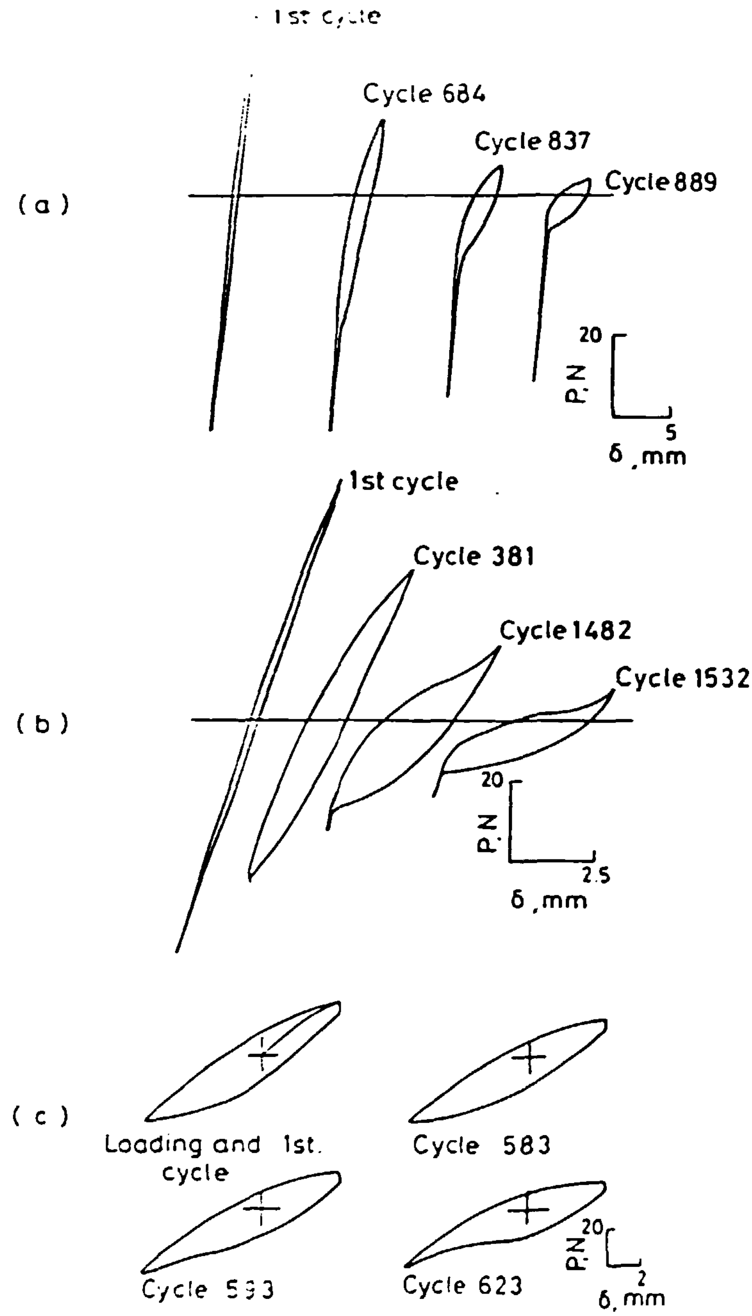

Fig. 36. Cyclic load-displacement behavior. (a) "Cantilever" specimen C5 held in tension, (b) "cantilever" specimen C8 held in compression, (c) "wishbone" specimen W9 held in tension.

ORNL-DWG 89-15004

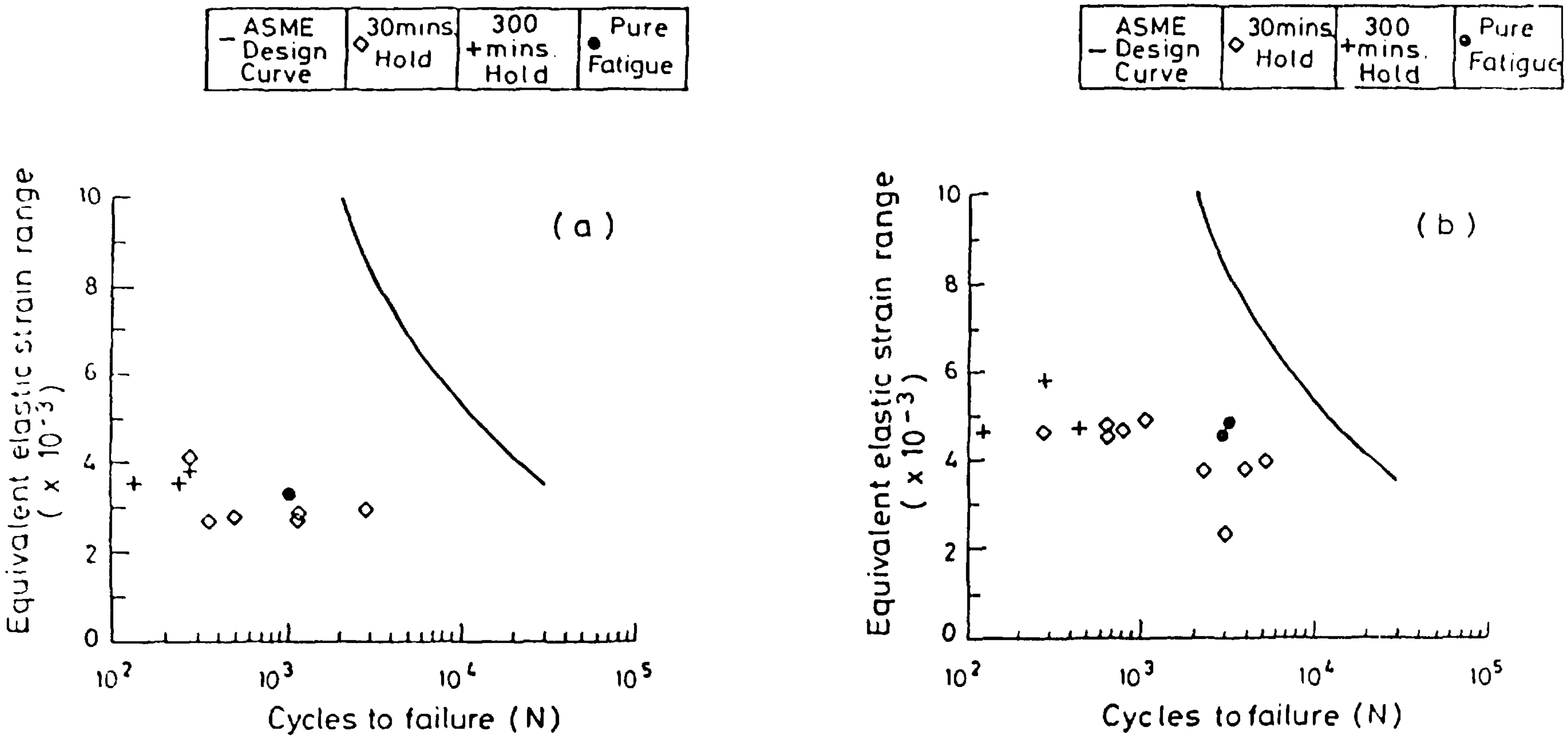

Fig. 37. Creep-fatigue endurance curves. (a) "Cantilever" specimens, (b) "wishbone" specimens.

ORNL-DWG 89-15005

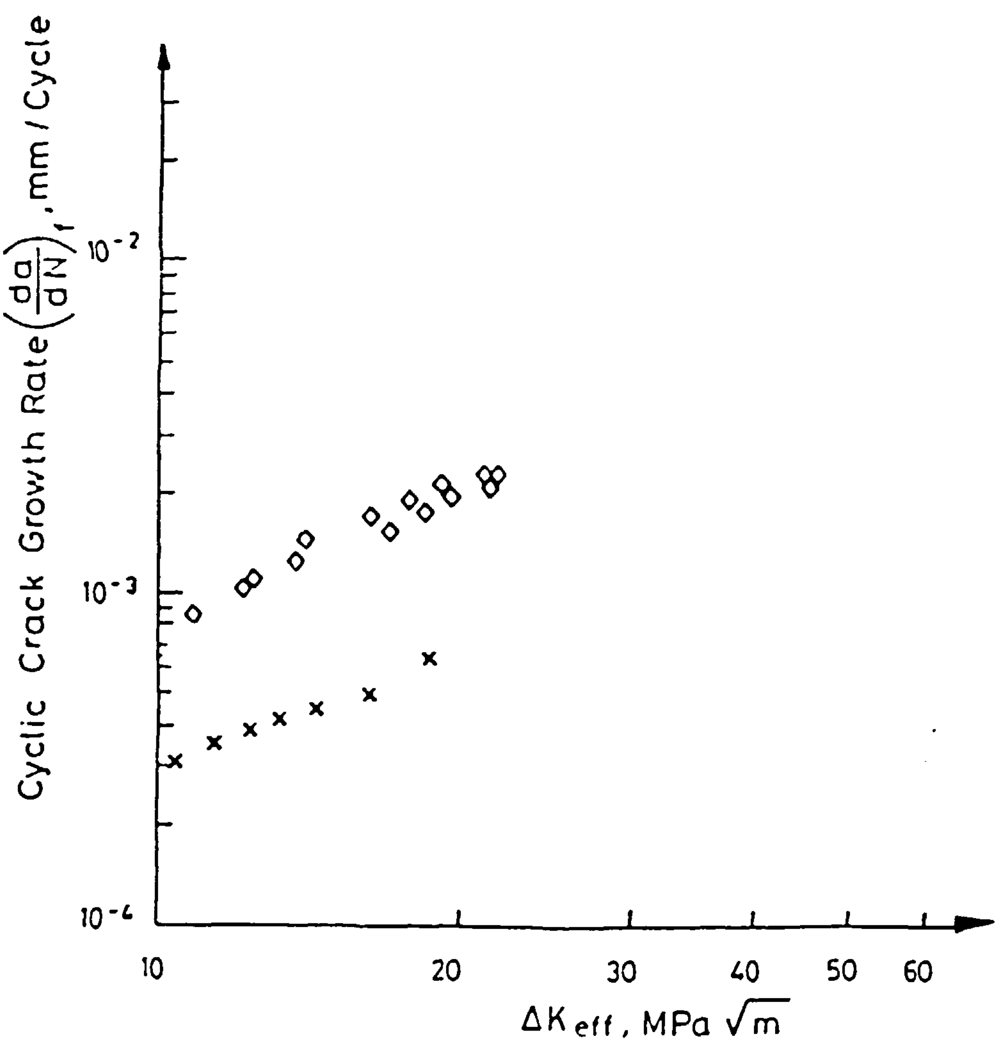

Fig. 38. Creep-fatigue crack growth rate correlations.

ORNL-DWG 89-15006

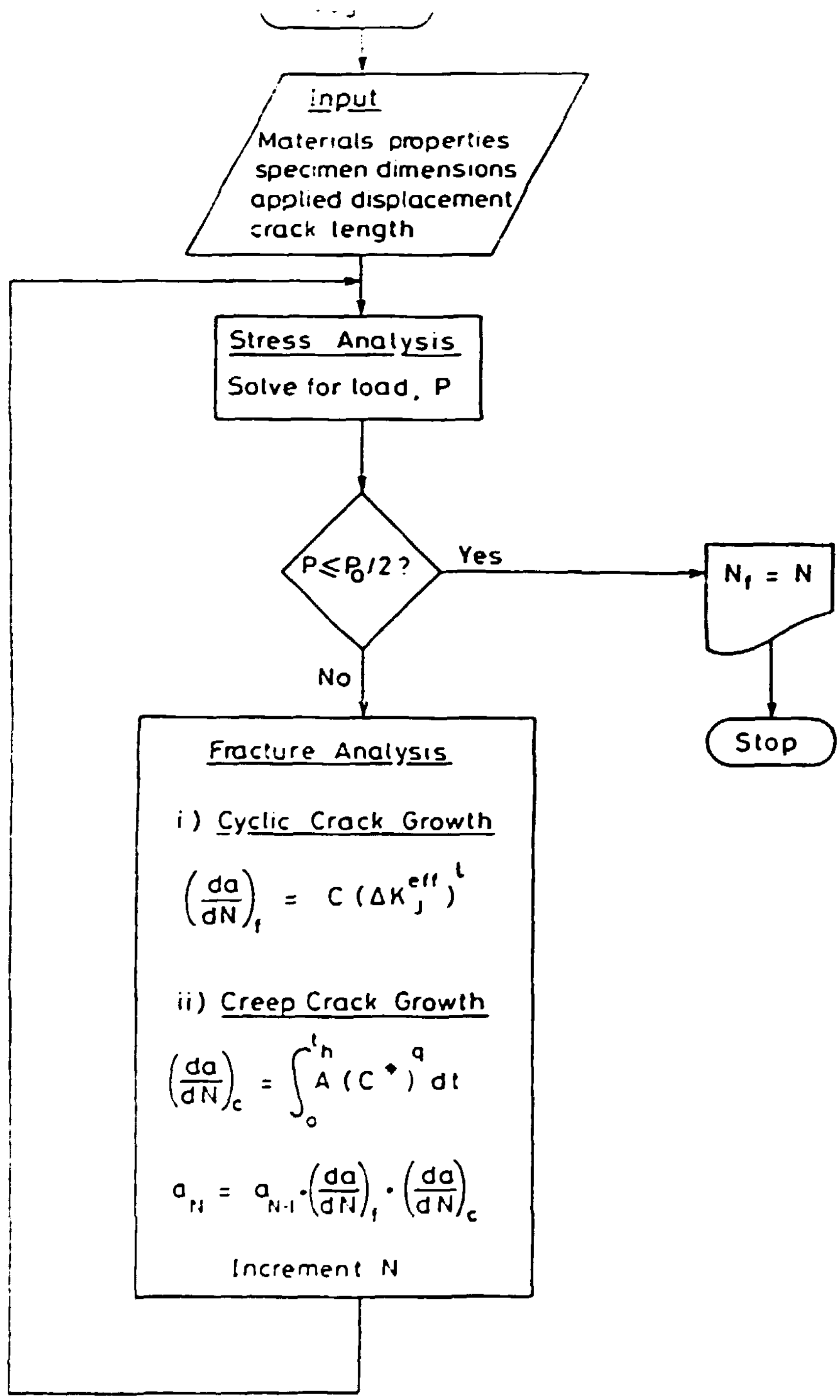

Fig. 39. Analysis procedure.

ORNL-DWG 89-15007

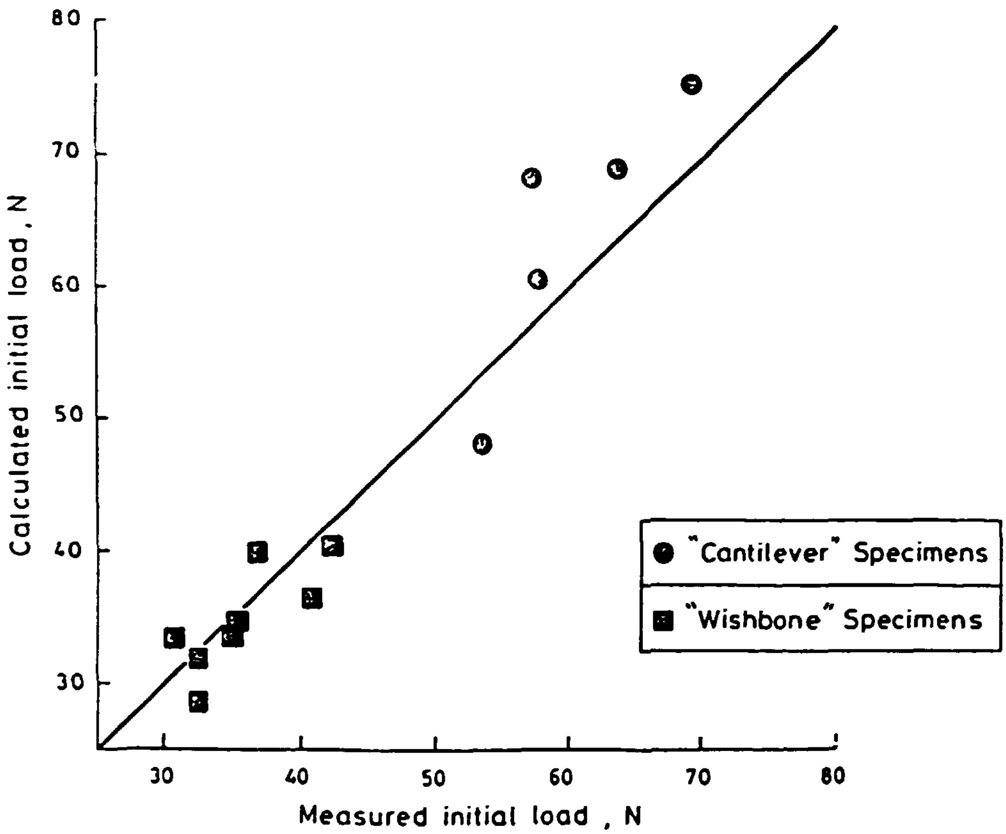

Fig. 40. Comparison between measured and calculated initial loads.

ORNL-DWG 89-15008

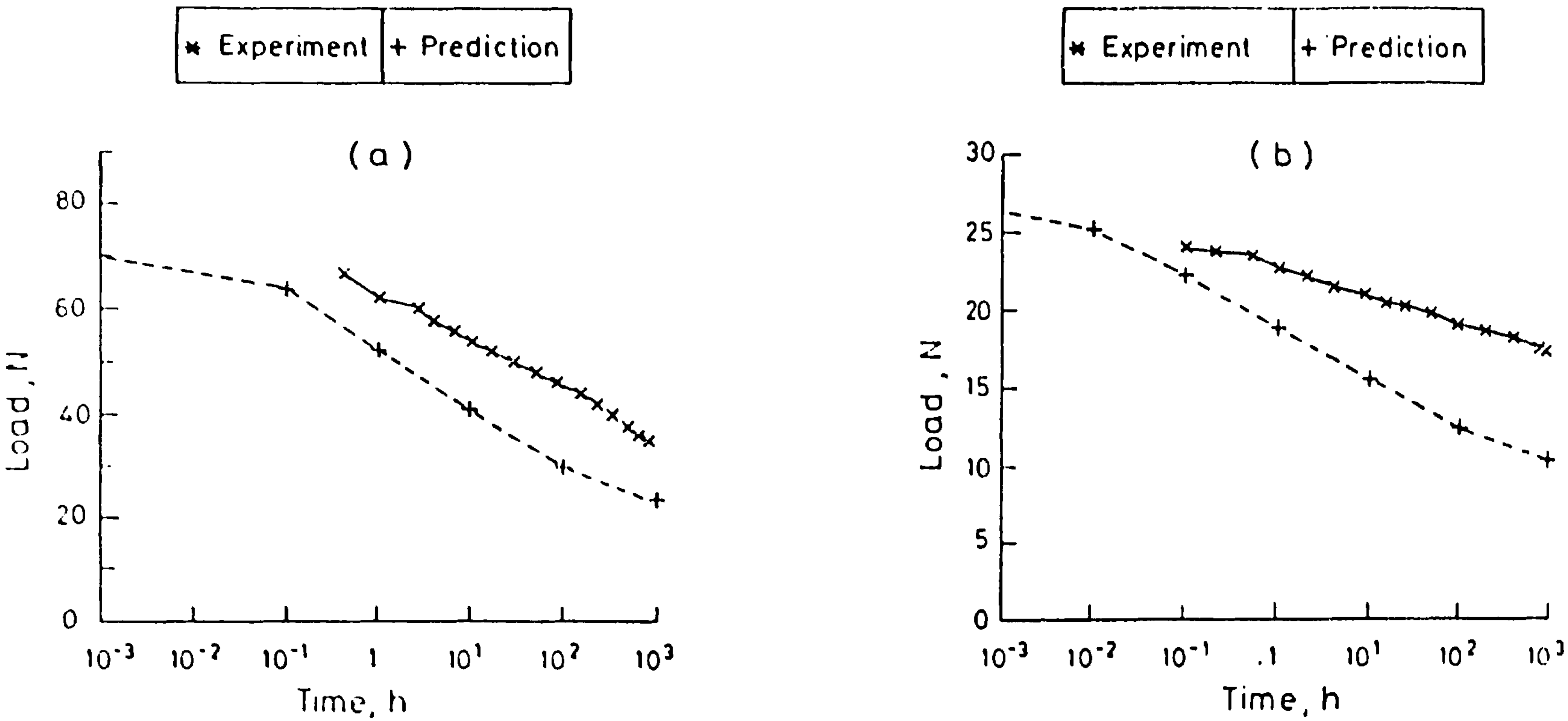

Fig. 41. Comparison between experimental and predicted load relaxation. (a) "Cantilever" specimen, (b) "wishbone" specimen.

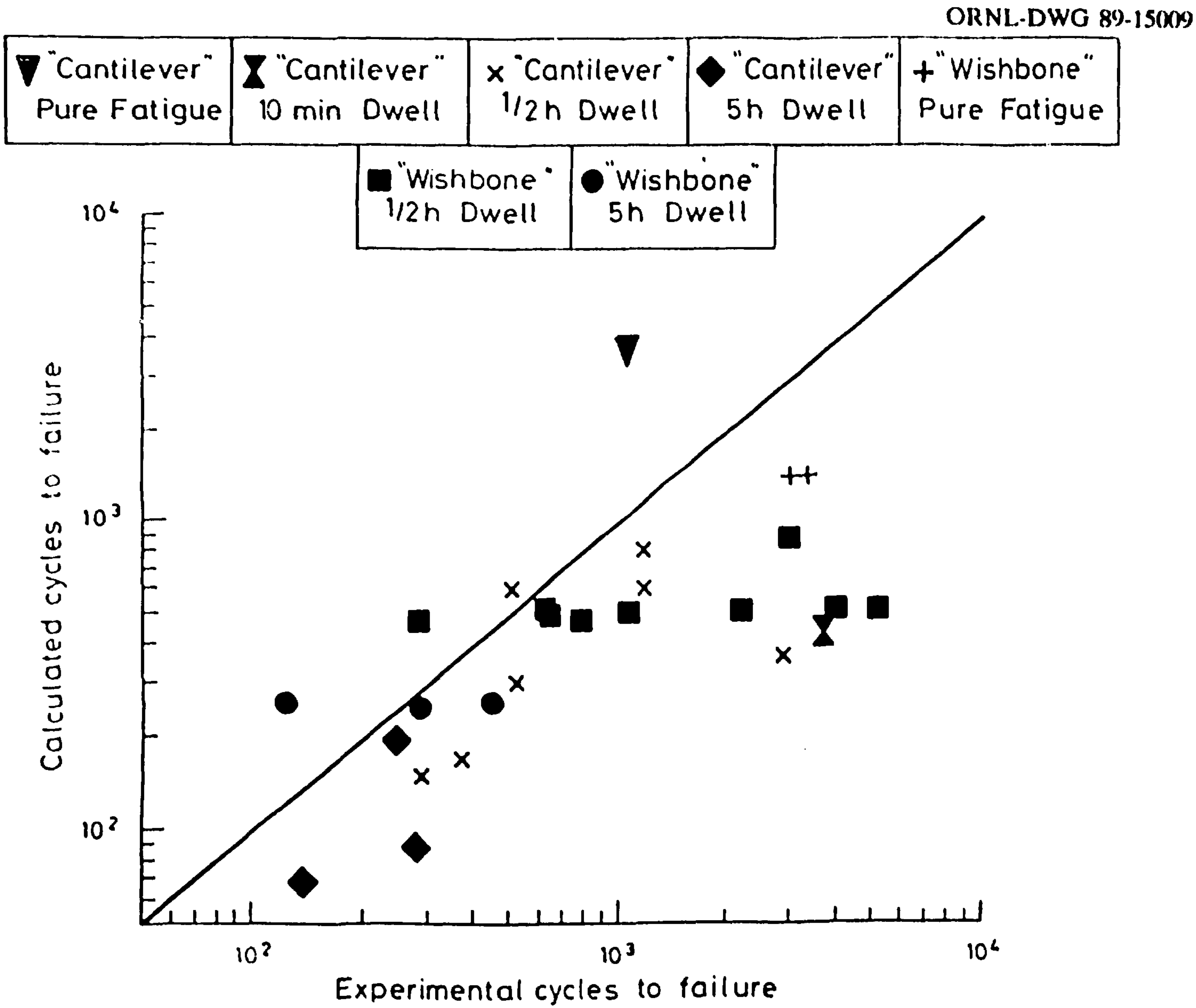

Fig. 42. Comparison between experimental and calculated cycles to failure under various creep-fatigue conditions.

ORNL-DWG 89-15010

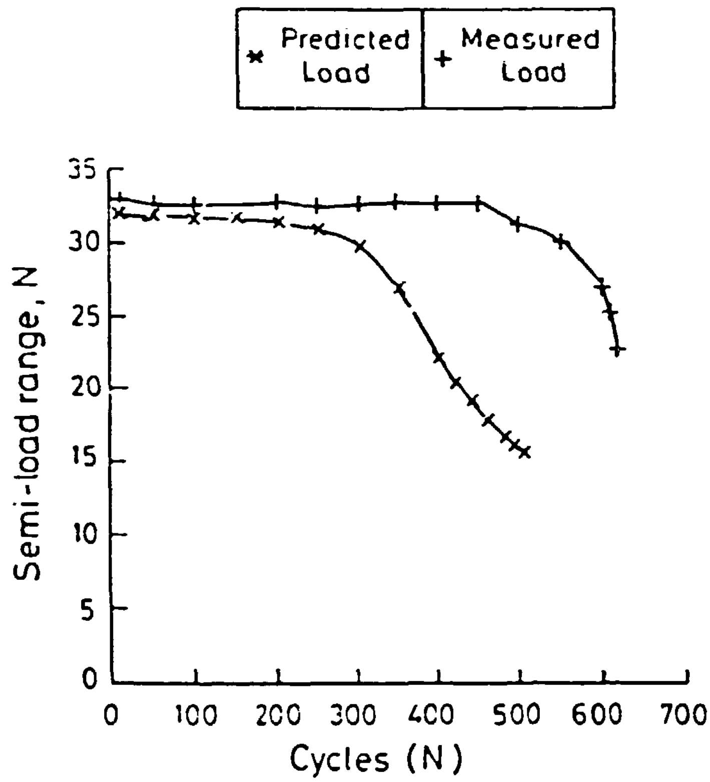

Fig. 43. Predicted vs experimental semi-load range for "wishbone" specimen W9.

ORNL-DWG 89-15011

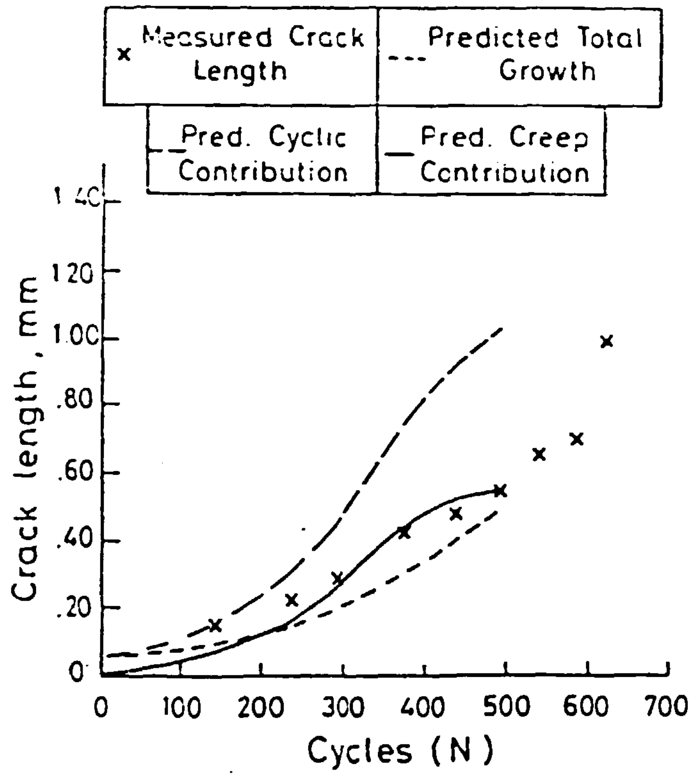

Fig. 44. Predicted vs experimental crack length for "wishbone" specimen W9.

ORNL-DWG 89-15012

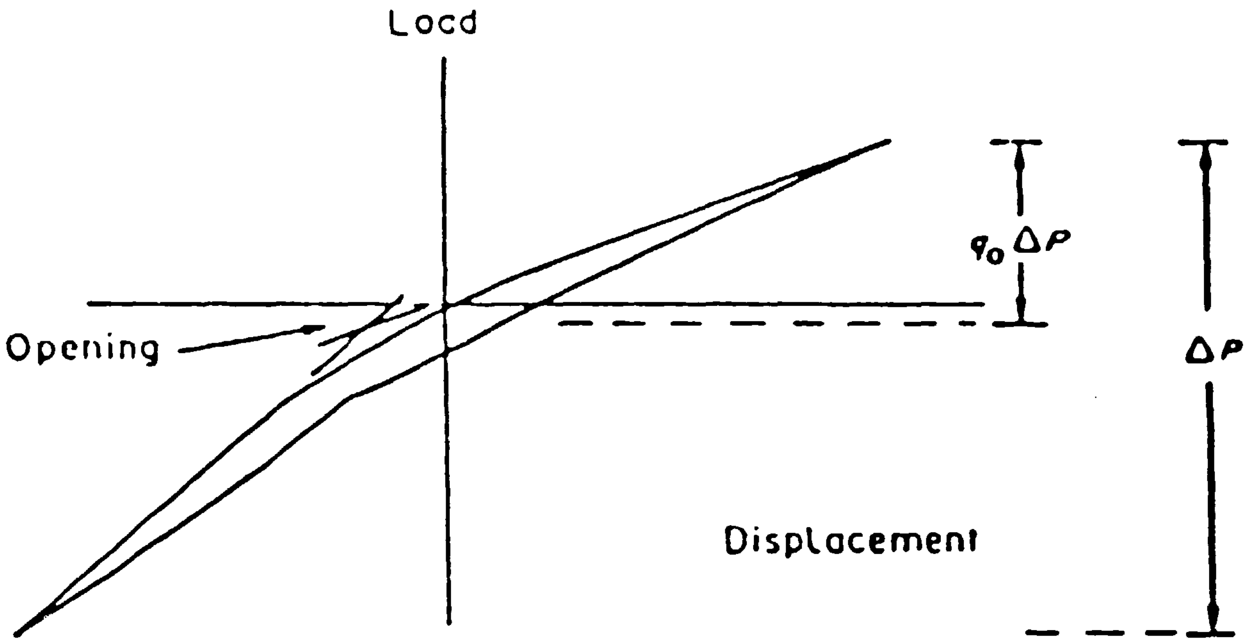

Fig. 45. Crack opening parameter q_0. Evaluation of q_0.

ORNL-DWG 89-15013

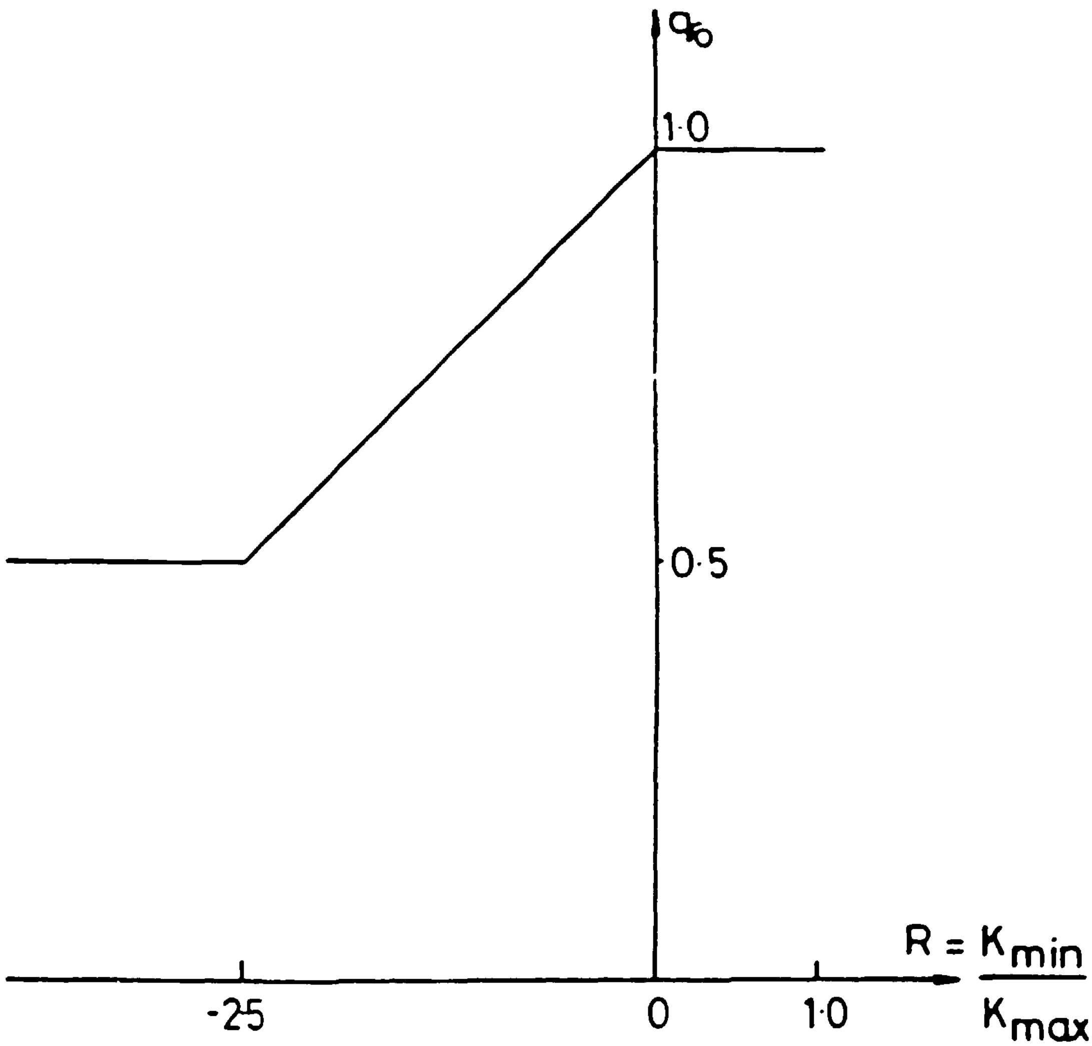

$$\Delta K_{eff} = q_o \ (K_{max} - K_{min})$$

Fig. 46. Definition of the parameter q_0 used to define ΔK_{eff} in Eqn. (18).

ORNL-DWG 89-15014

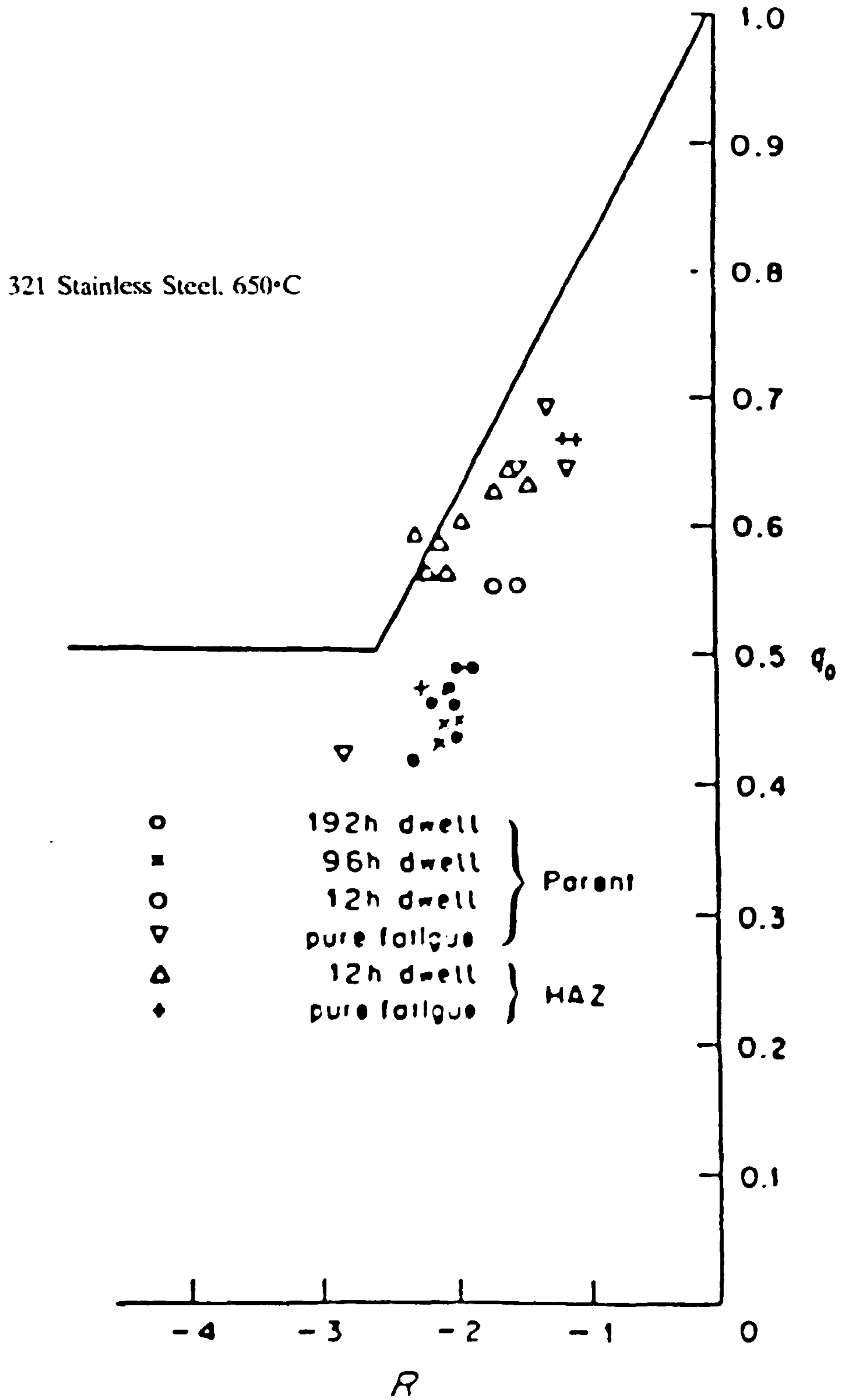

Fig. 47. Effect of R ratio on the q_0 for type 321 stainless steel at 650°C.

ORNL-DWG 89-15015

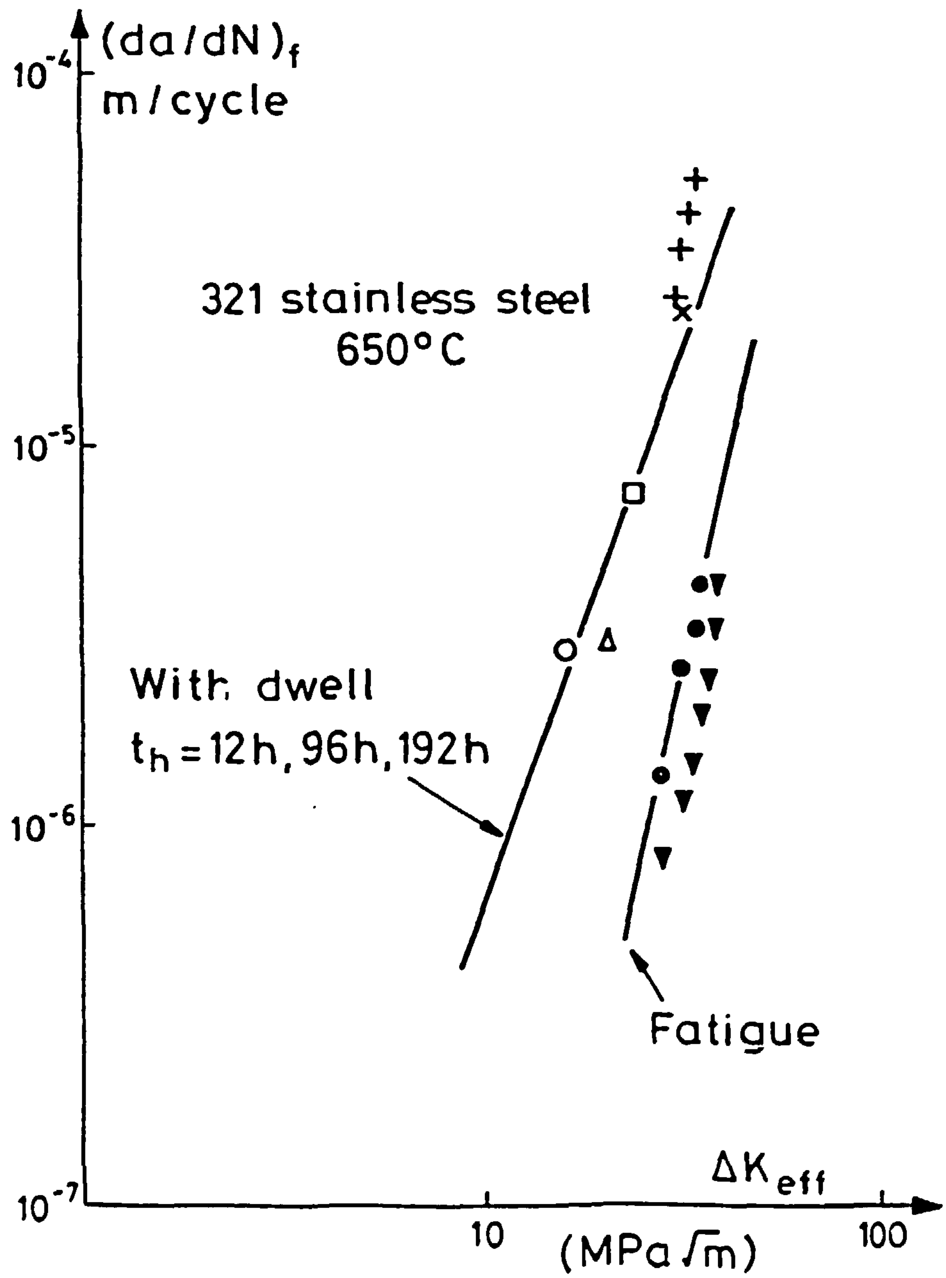

Fig. 48. Cyclic response of aged type 321 stainless steel and HAZ at 650°C.

ORNL-DWG 89-15016

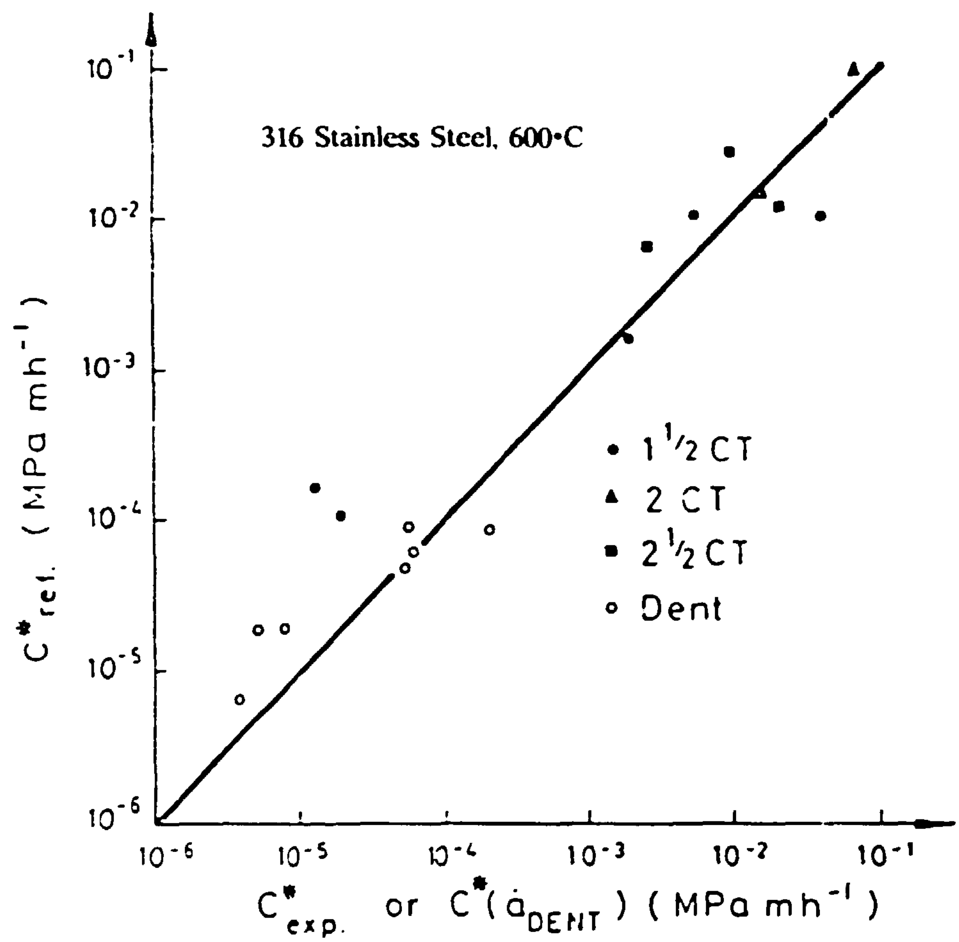

Fig. 49. Comparison of value of C* predicted by Eqn. (12), C^*_{ref}, with that deduced from experimental data, C^*_{exp}, for an austenitic type 316 stainless steel, for CT specimens of various thickness and for DENT specimens.

ORNL-DWG 89-15017

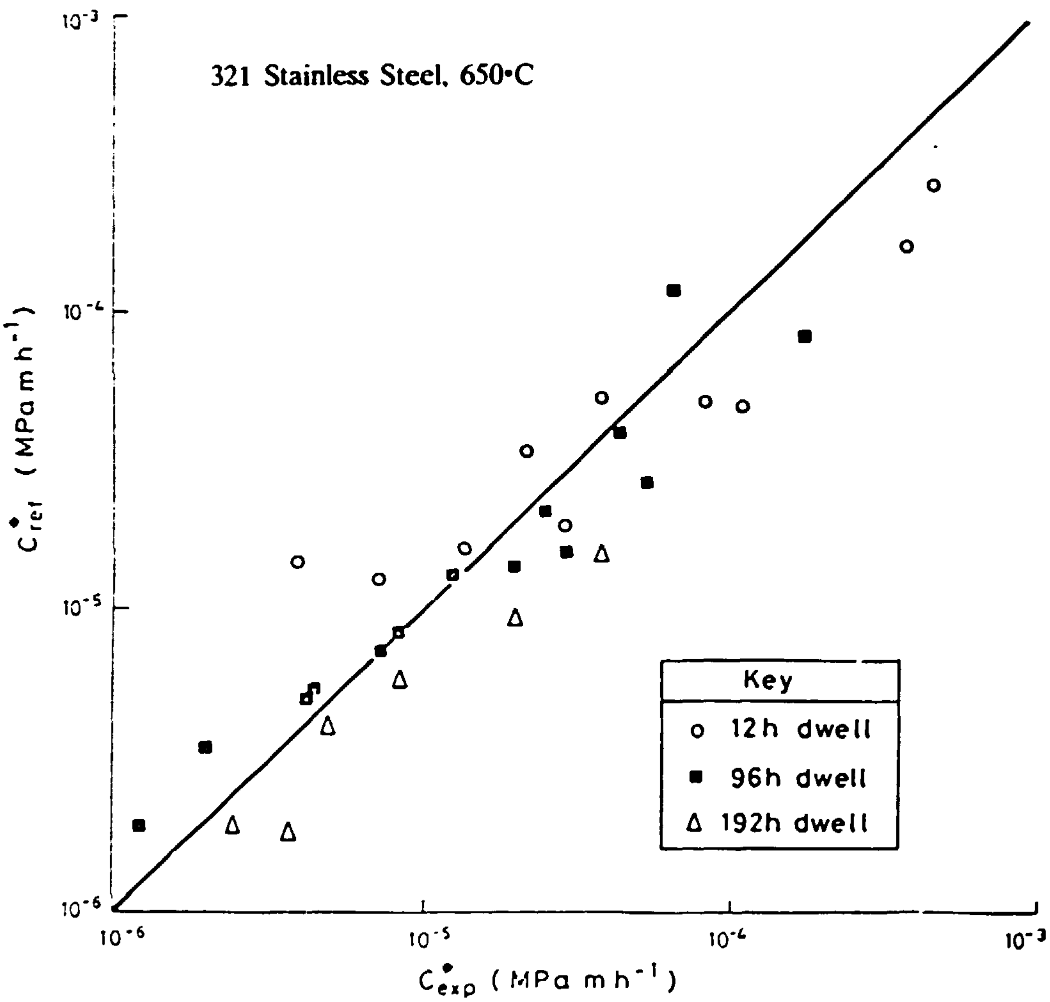

Fig. 50. Comparison of value of C^* predicted by Eqn. (12), C^*_{ref}, with that deduced from experimental data, C^*_{exp}, for an austenitic type 321 stainless steel (after Gladwin et al[1]).

ORNL-DWG 89-15018

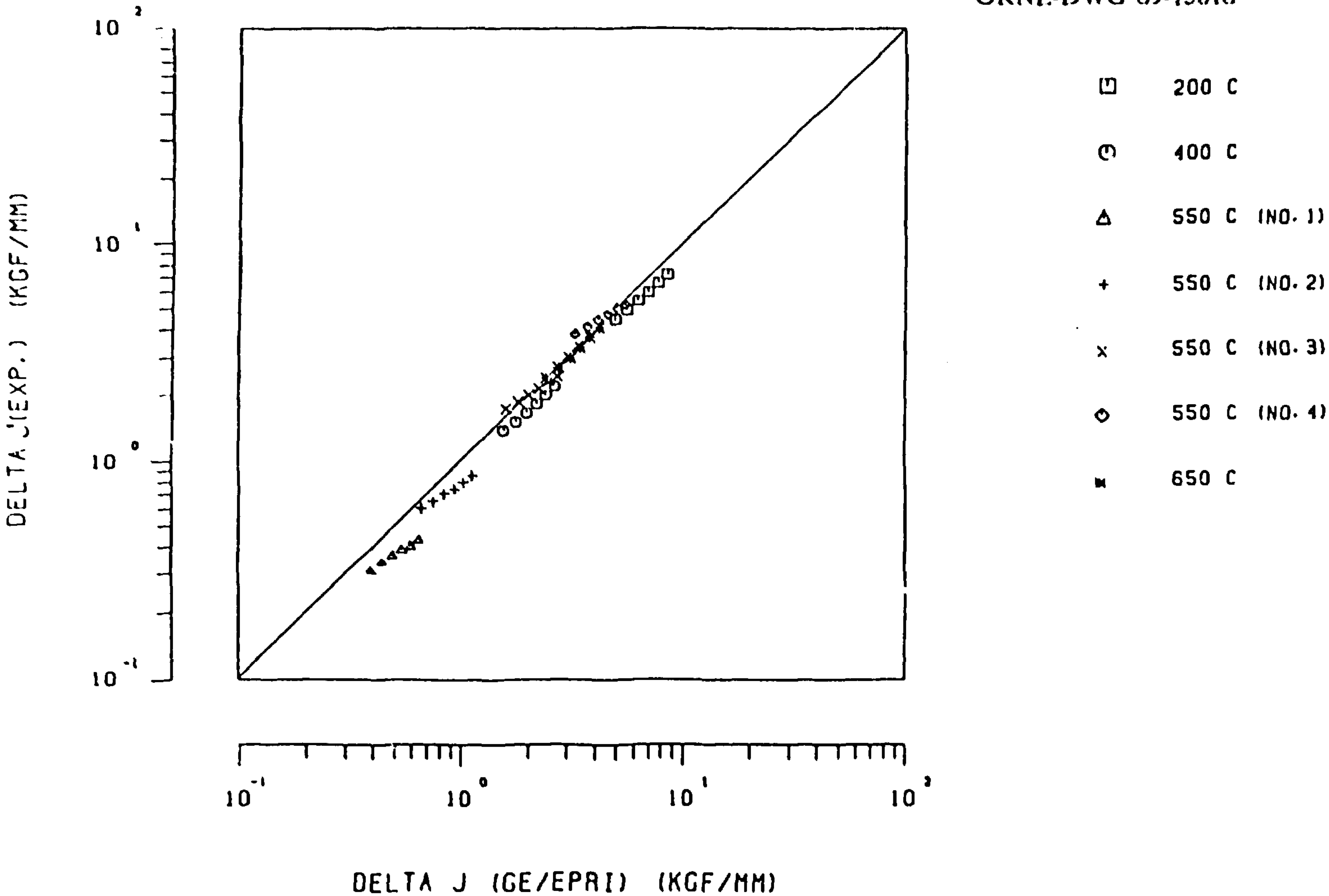

Fig. 51. Comparison of fatigue J-integral range values obtained by GE/EPRI method with those determined experimentally.

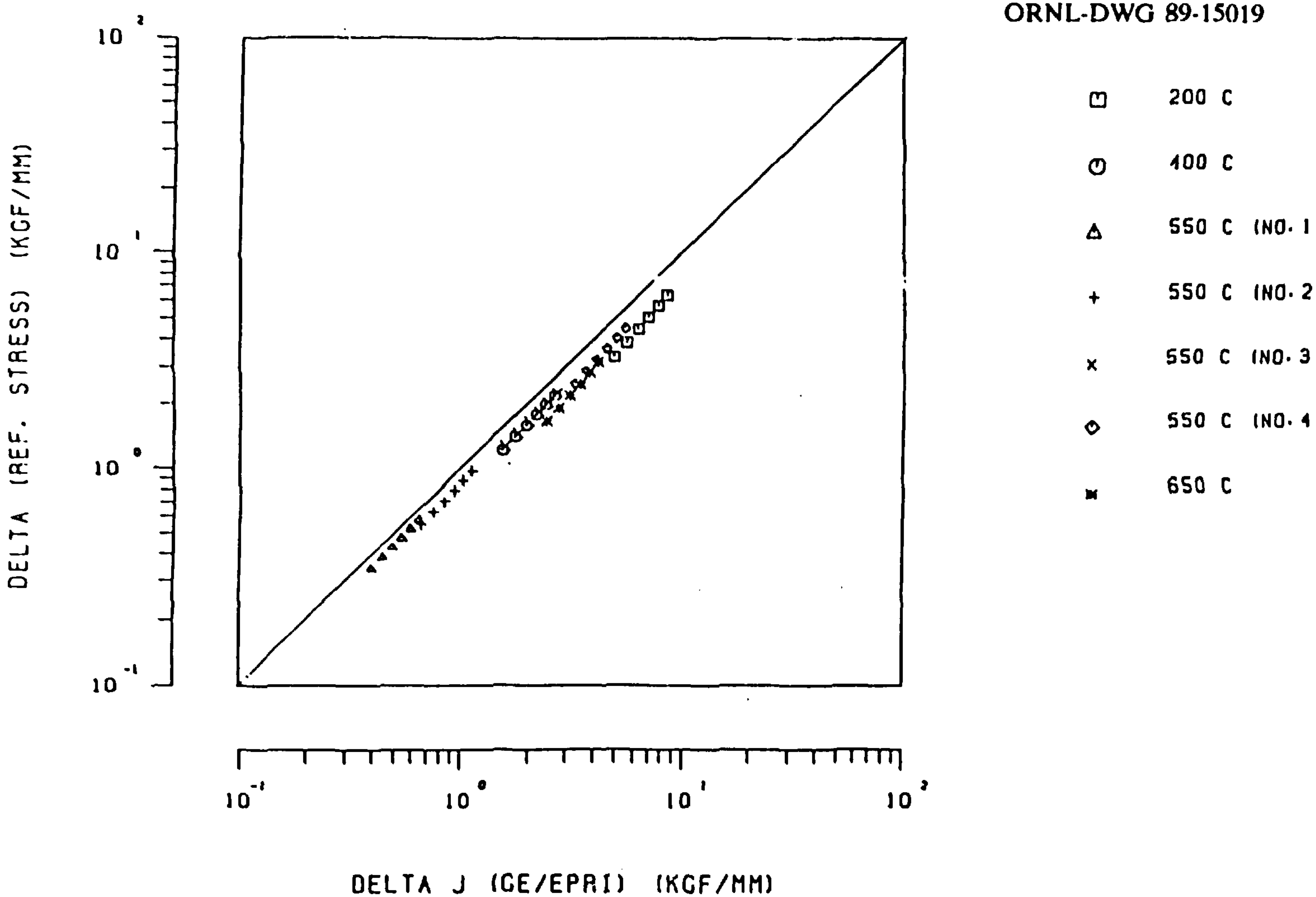

Fig. 52. Comparison of fatigue J-integral range values obtained by GE/EPRI and reference stress methods.

ORNL-DWG 89-15020

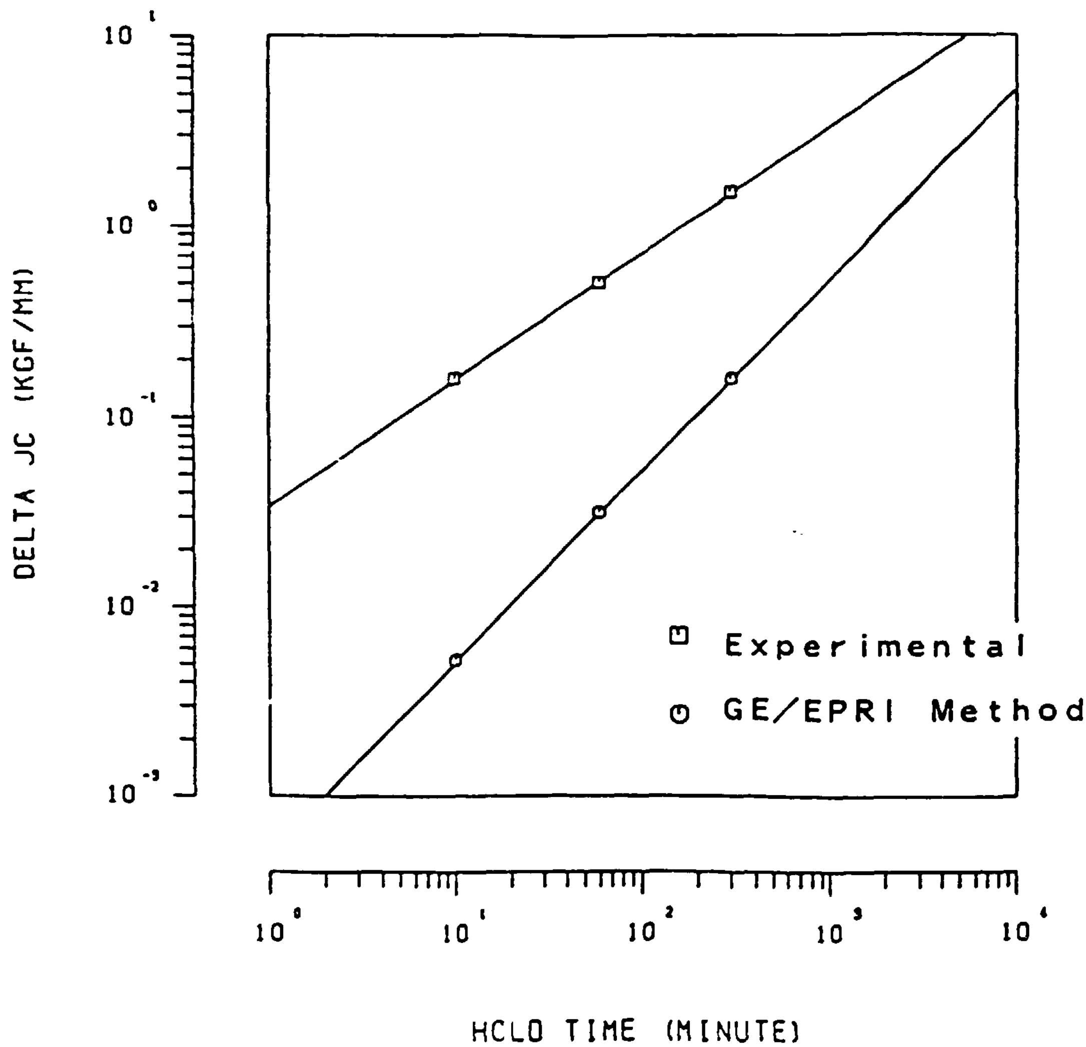

Fig. 53. Comparison of creep J-integral range values obtained by GE/EPRI methods with those determined experimentally.

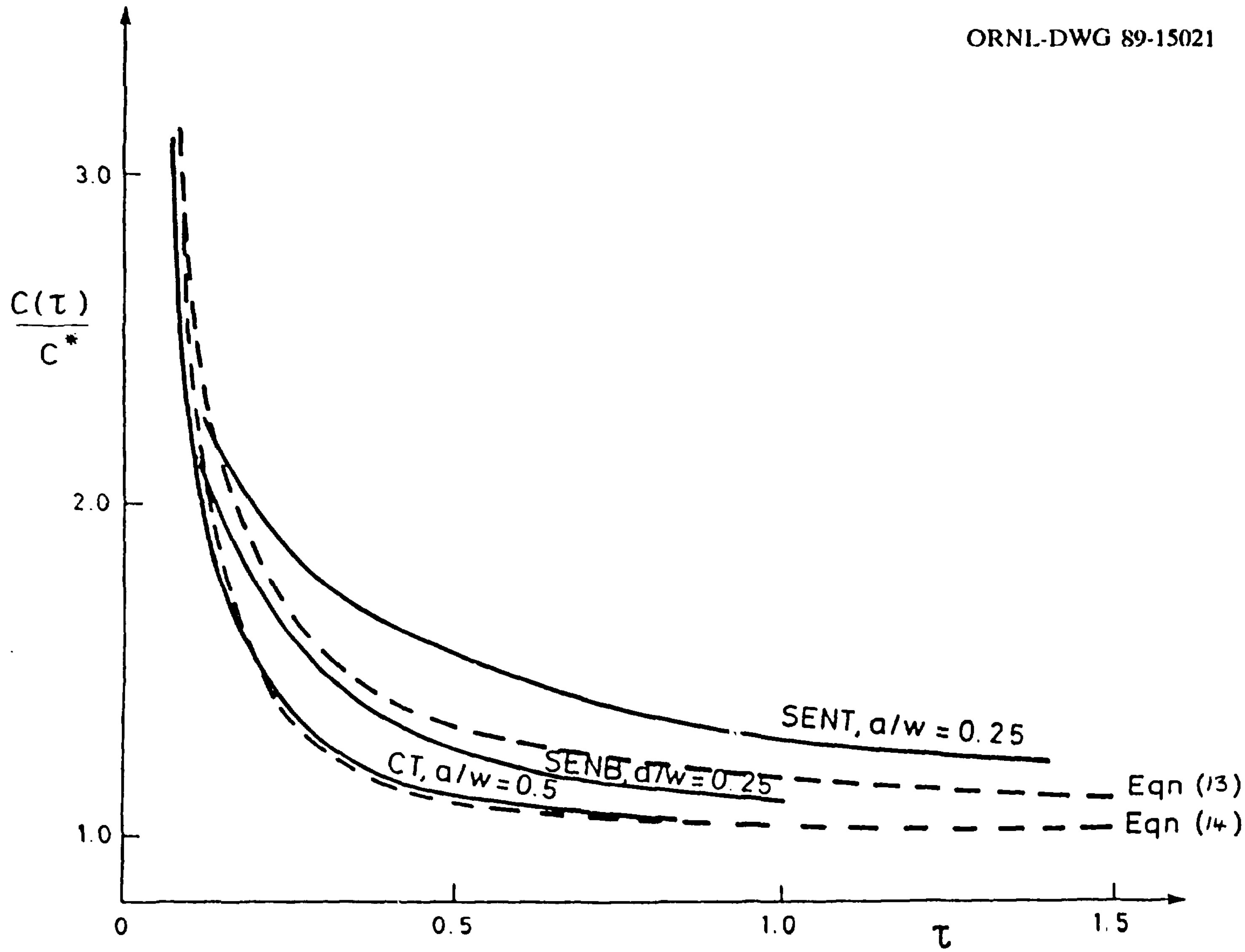

Fig. 54. Variation of C(t) for the compact tension and for the single edge notch geometry under tension and bending.

ORNL-DWG 89-15022

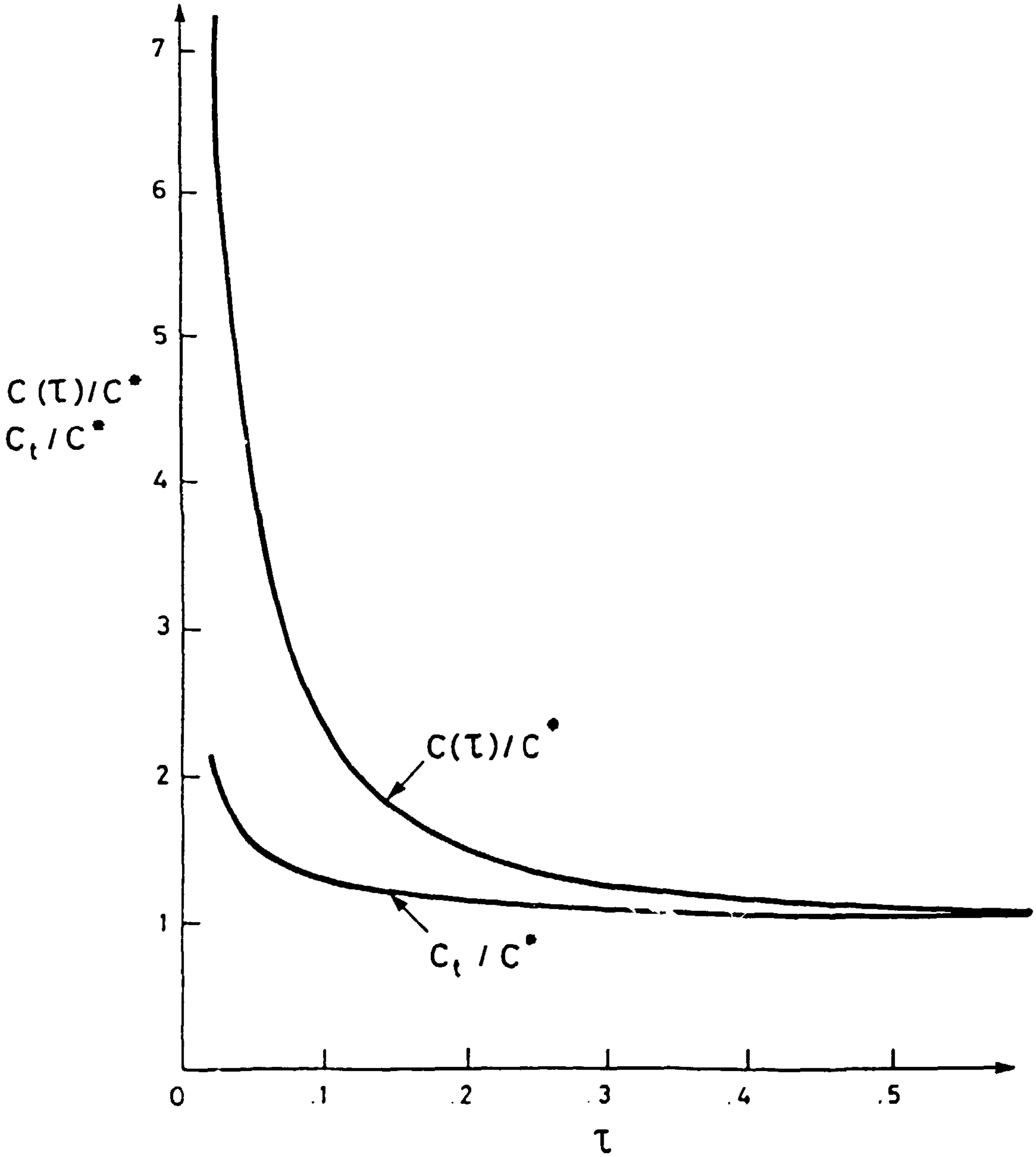

Fig. 55. Comparison of variation of C_t by Saxena[17] with that of C(t).

ORNL-DWG 89-15023

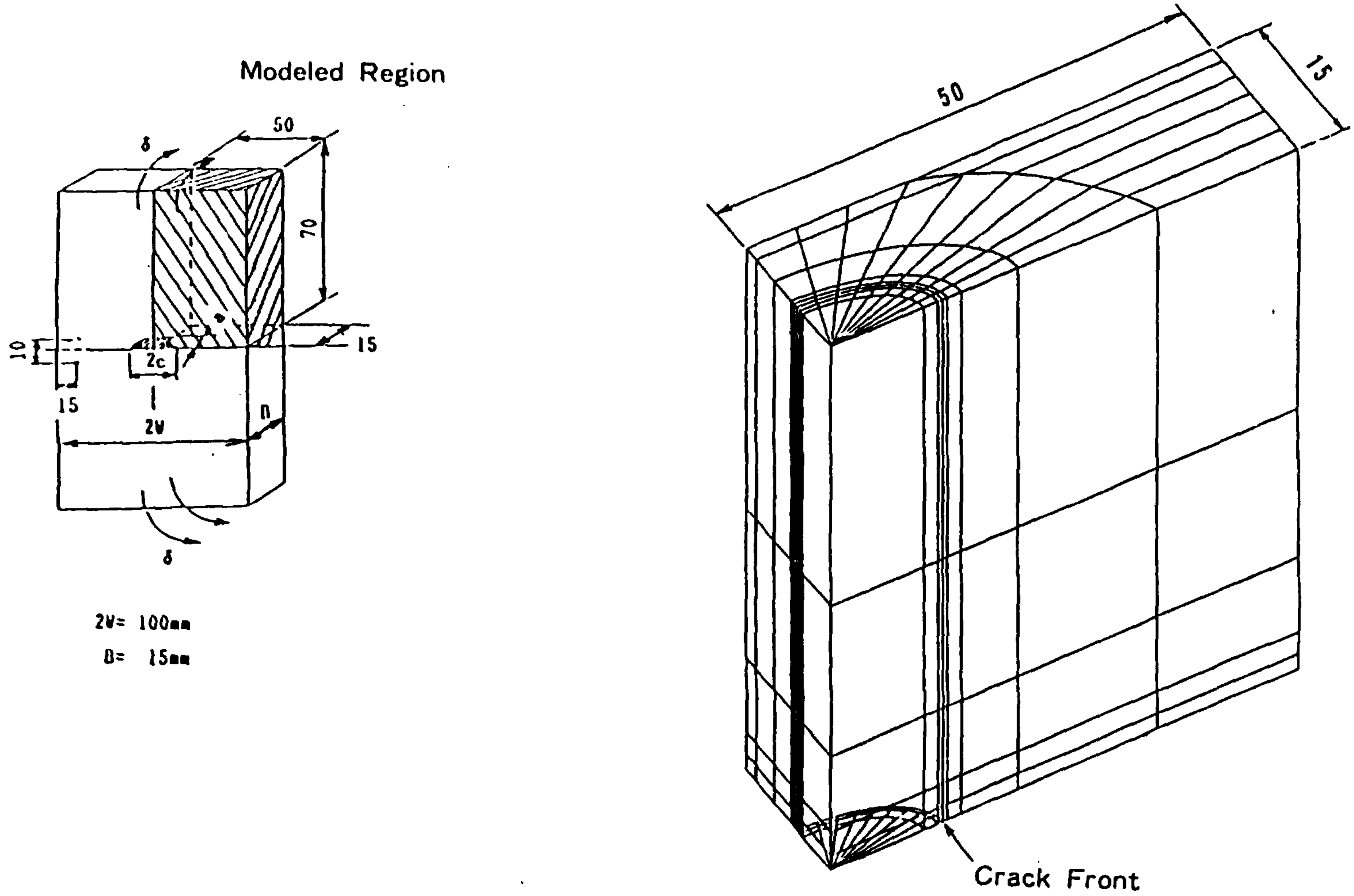

Fig. 56. Finite element model of one quarter of the surface crack specimen.

ORNL-DWG 89-15024

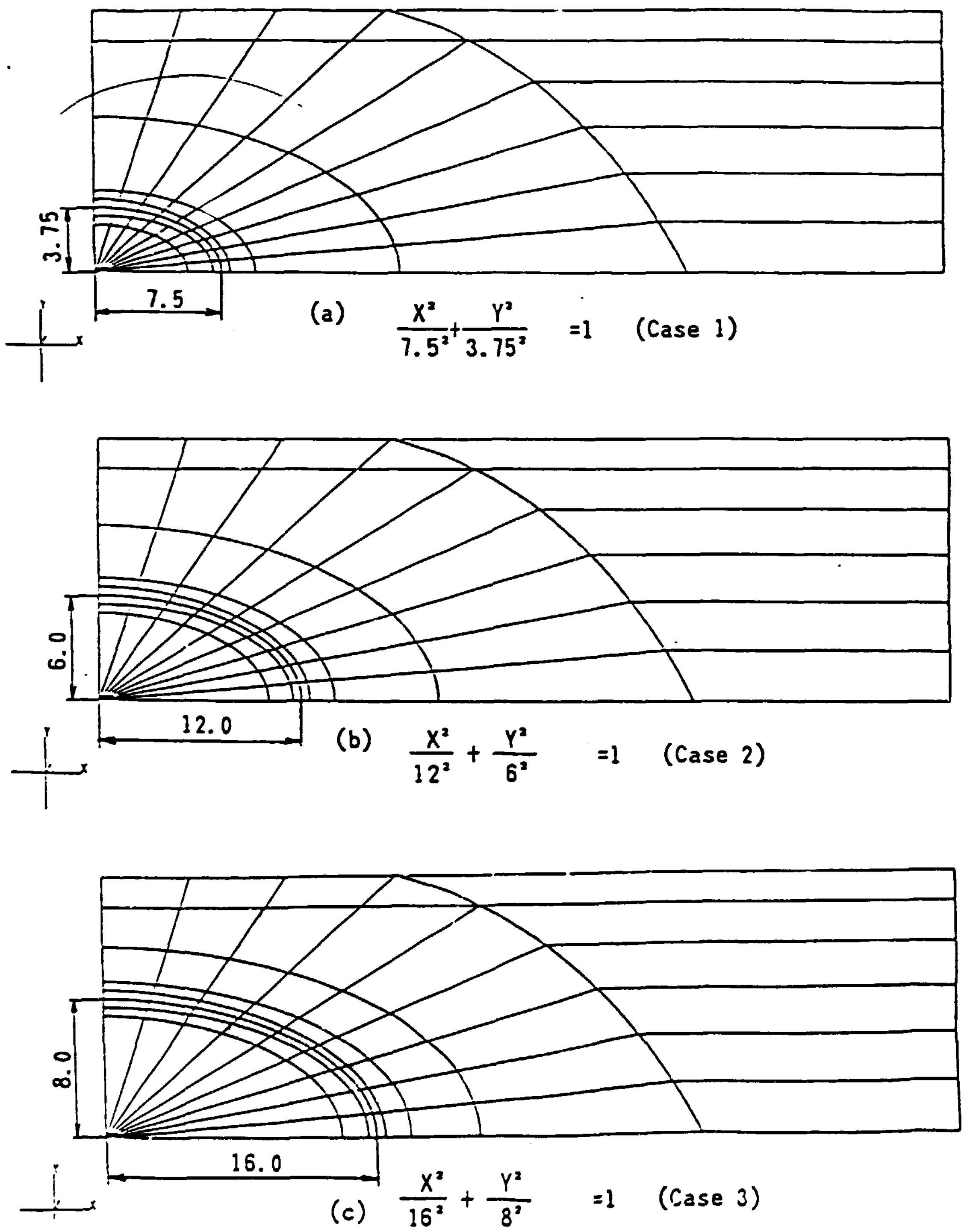

Fig. 57. Finite element meshes for the three crack sizes.

ORNL-DWG 89-15025

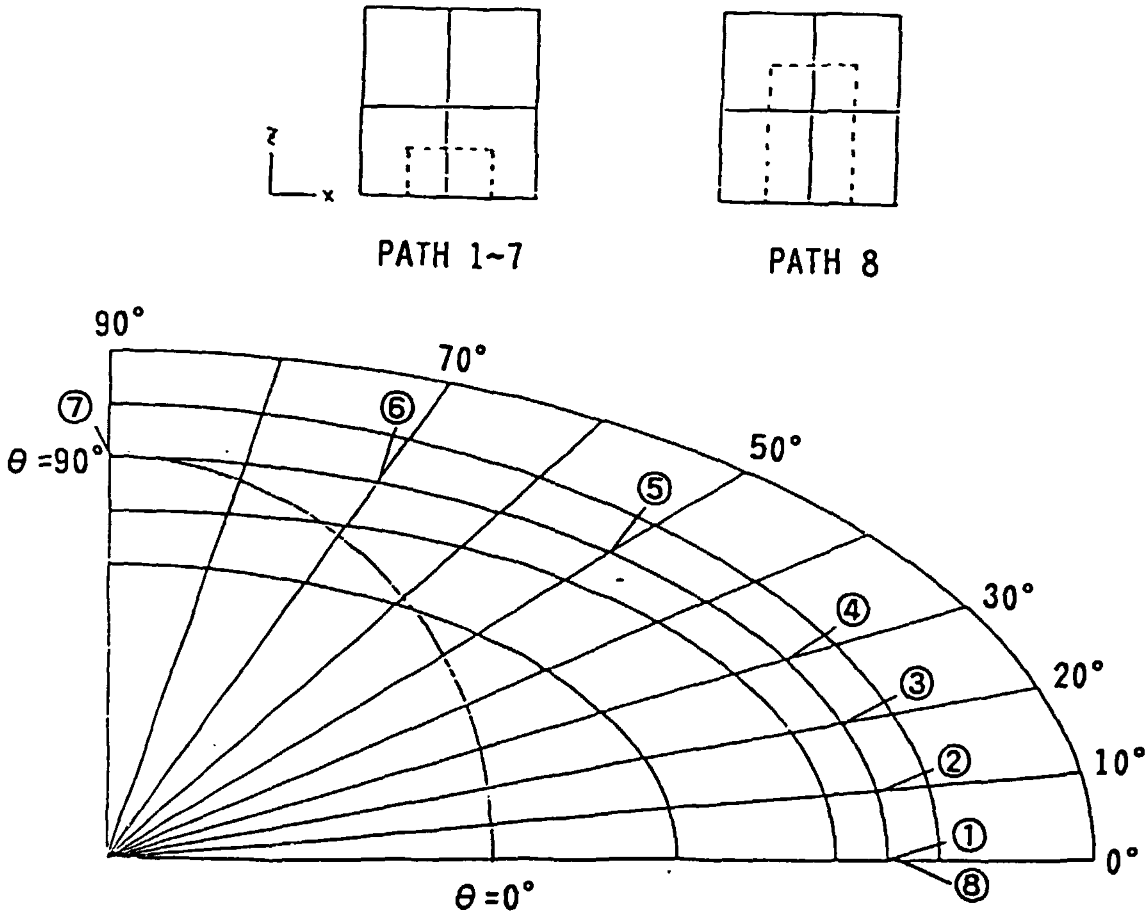

Fig. 58. Paths for J-integral evaluation by virtual crack extension method.

ORNL-DWG 89-15026

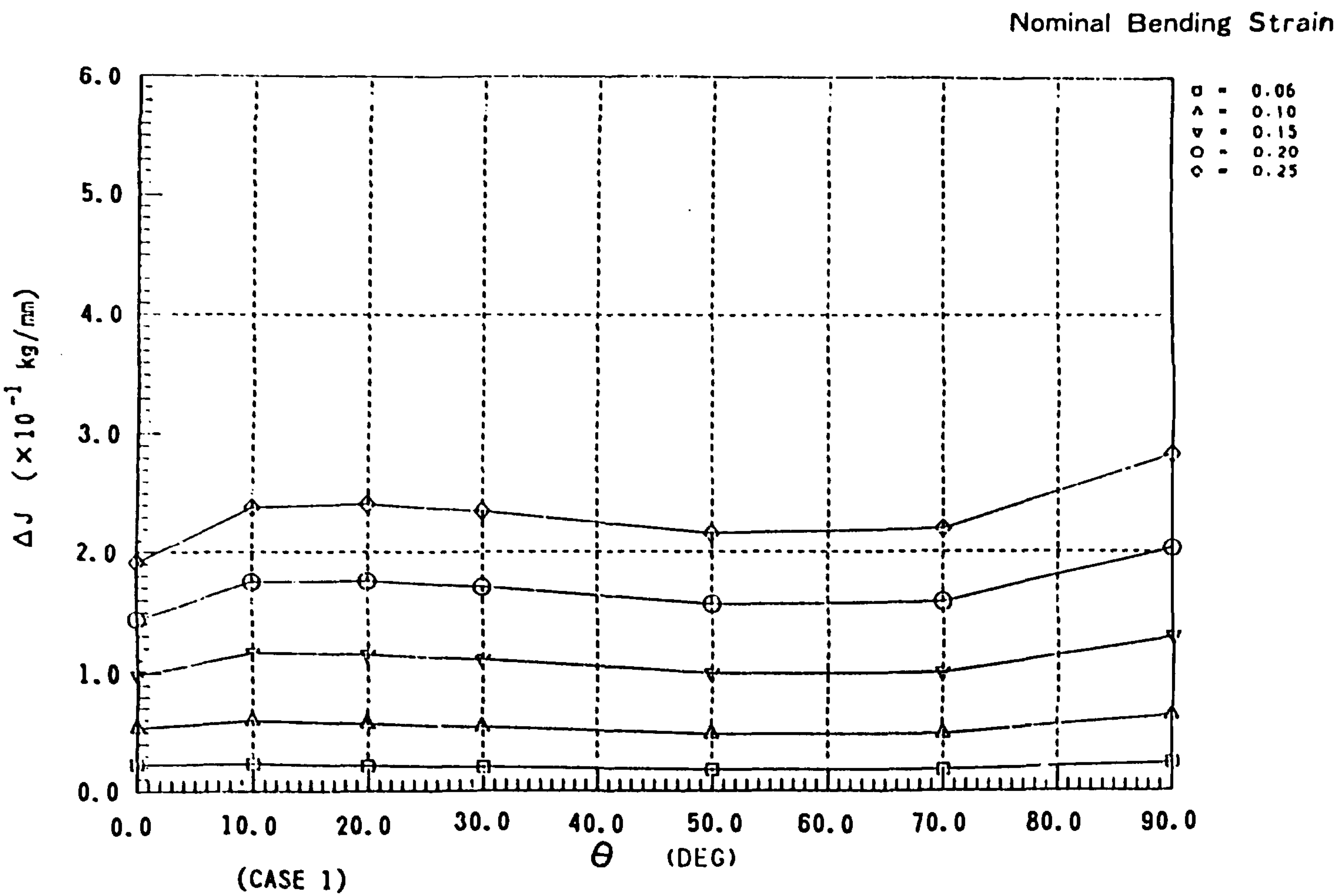

Fig. 59. Variation of fatigue J-integral range along the crack front.

ORNL-DWG 89-15027

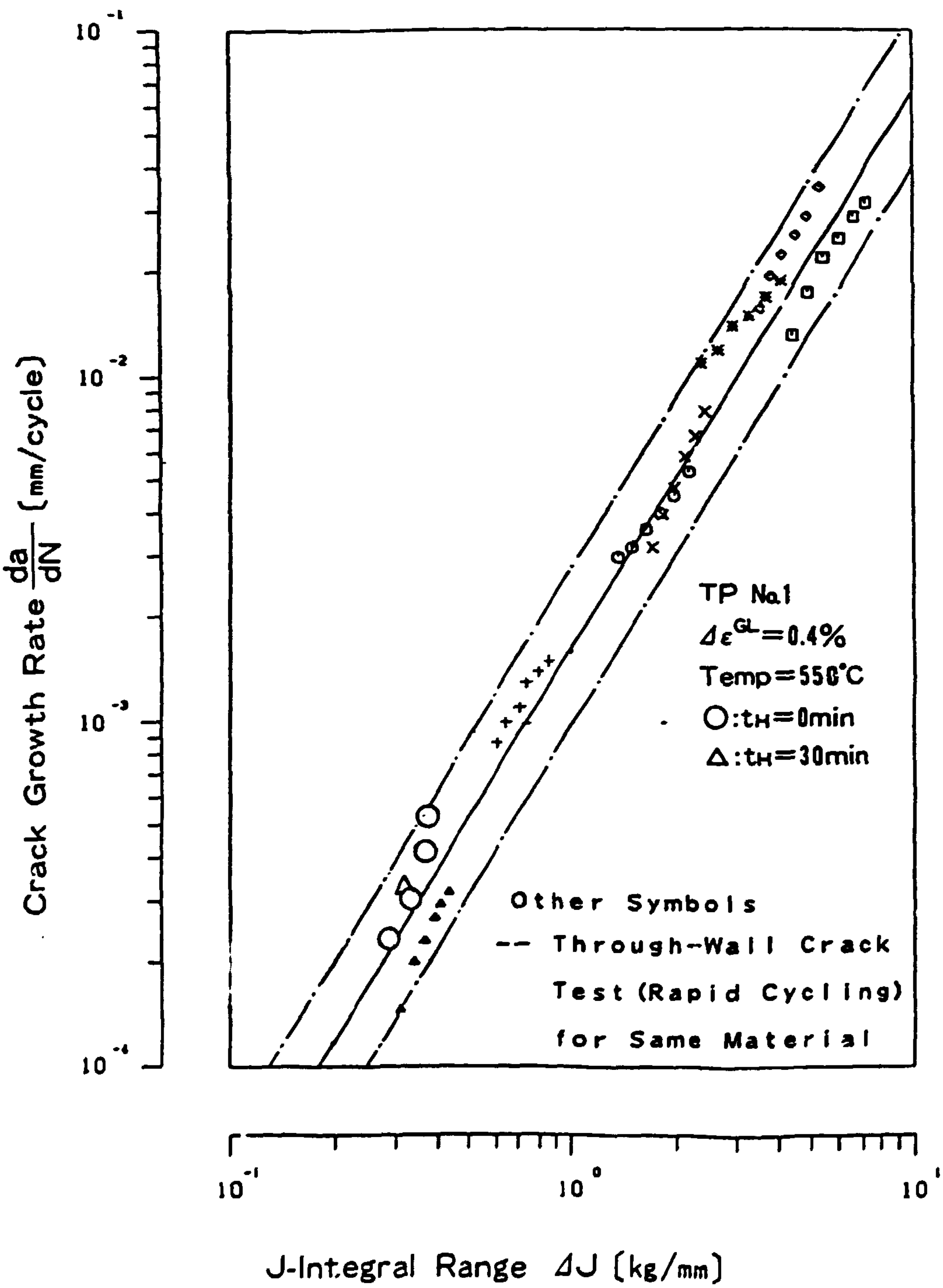

Fig. 60. Crack growth rate vs fatigue J-integral range relation.

ORNL-DWG 89-15028

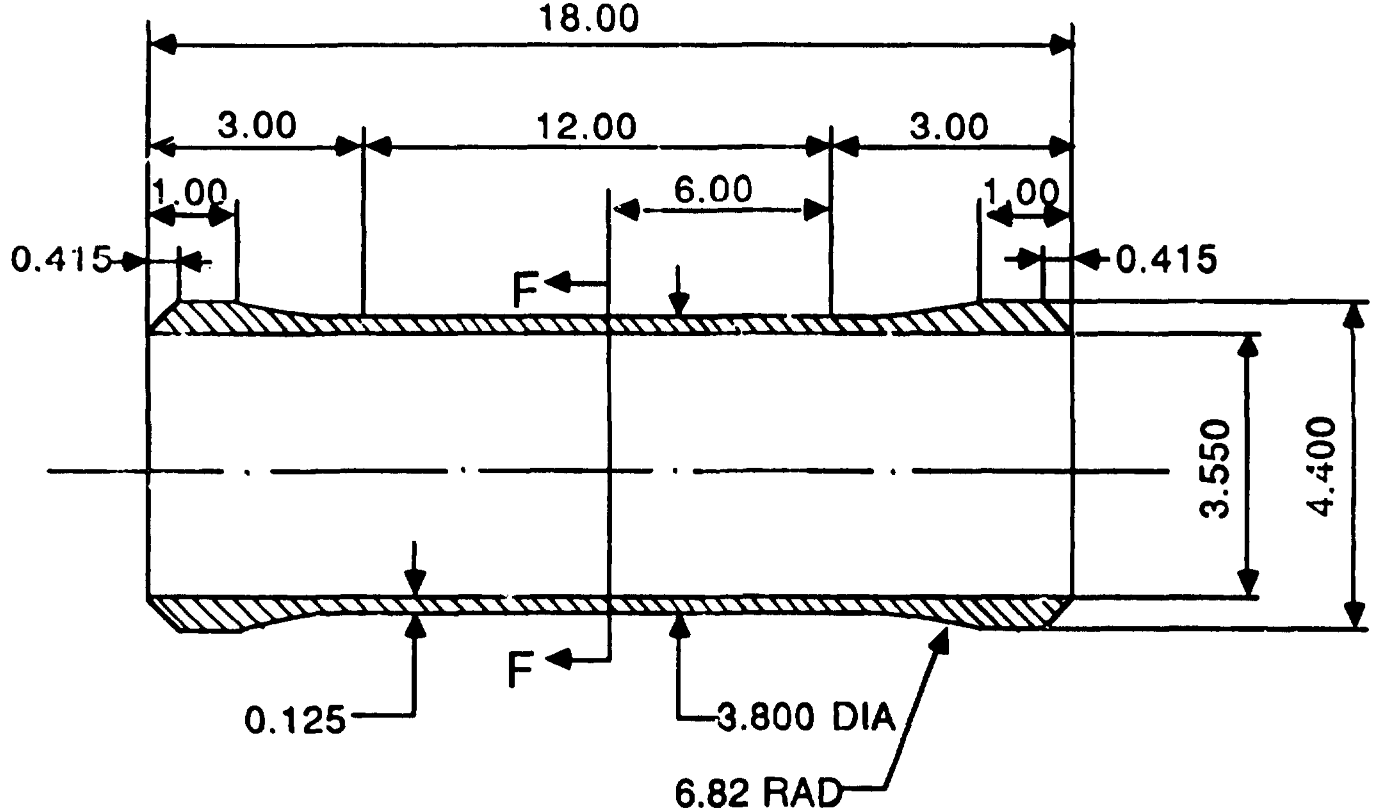

UNIT: 1 in

Fig. 61. Thin-walled pressurized pipe specimen.

ORNL-DWG 89-15029

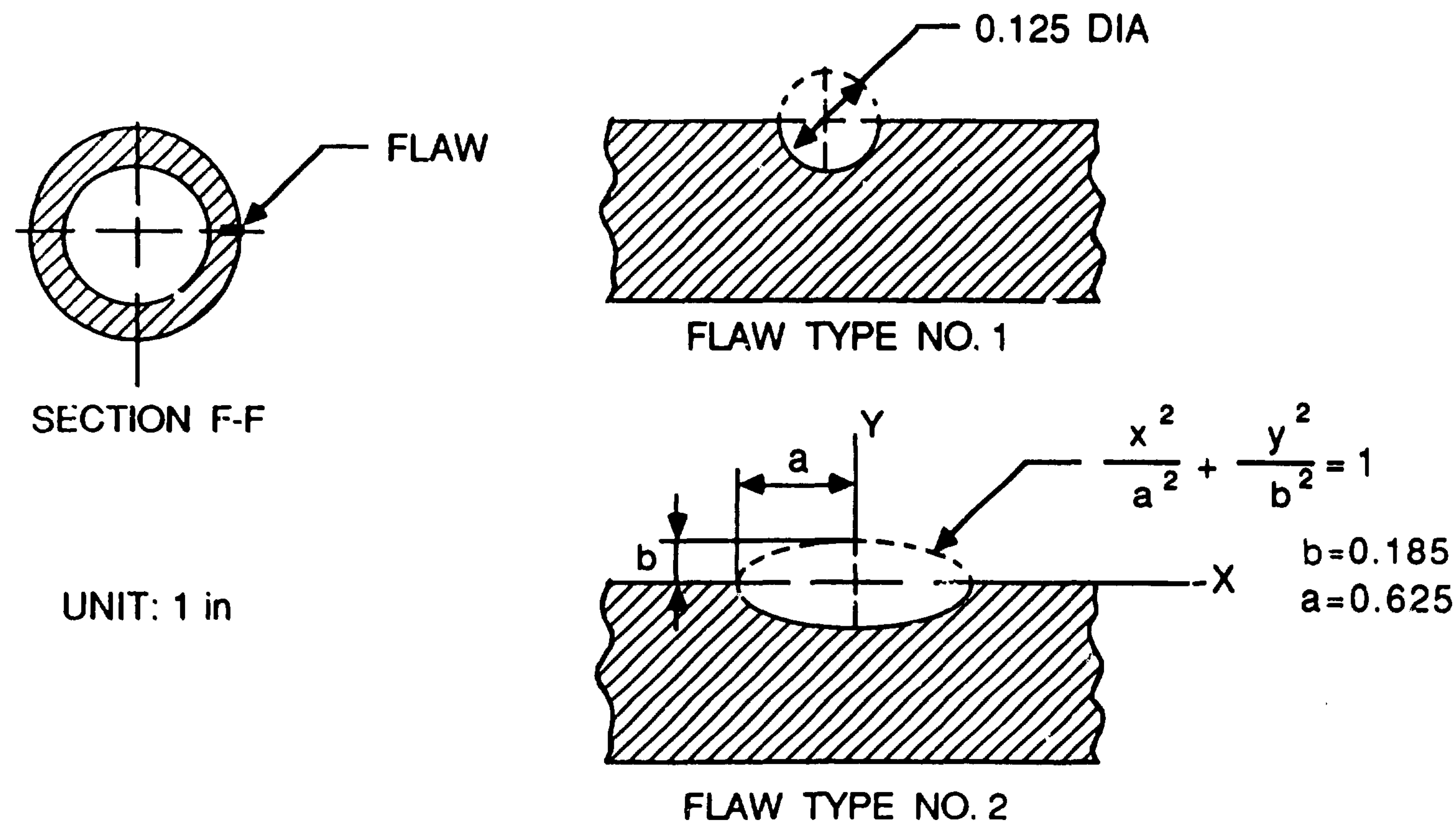

Fig. 62. Schematic of the two types of axial flaws used for thin-walled pressurized pipe specimens.

ORNL PHOTO 8158-89

Fig. 63. Thin-walled pressurized pipe specimens prepared for testing.

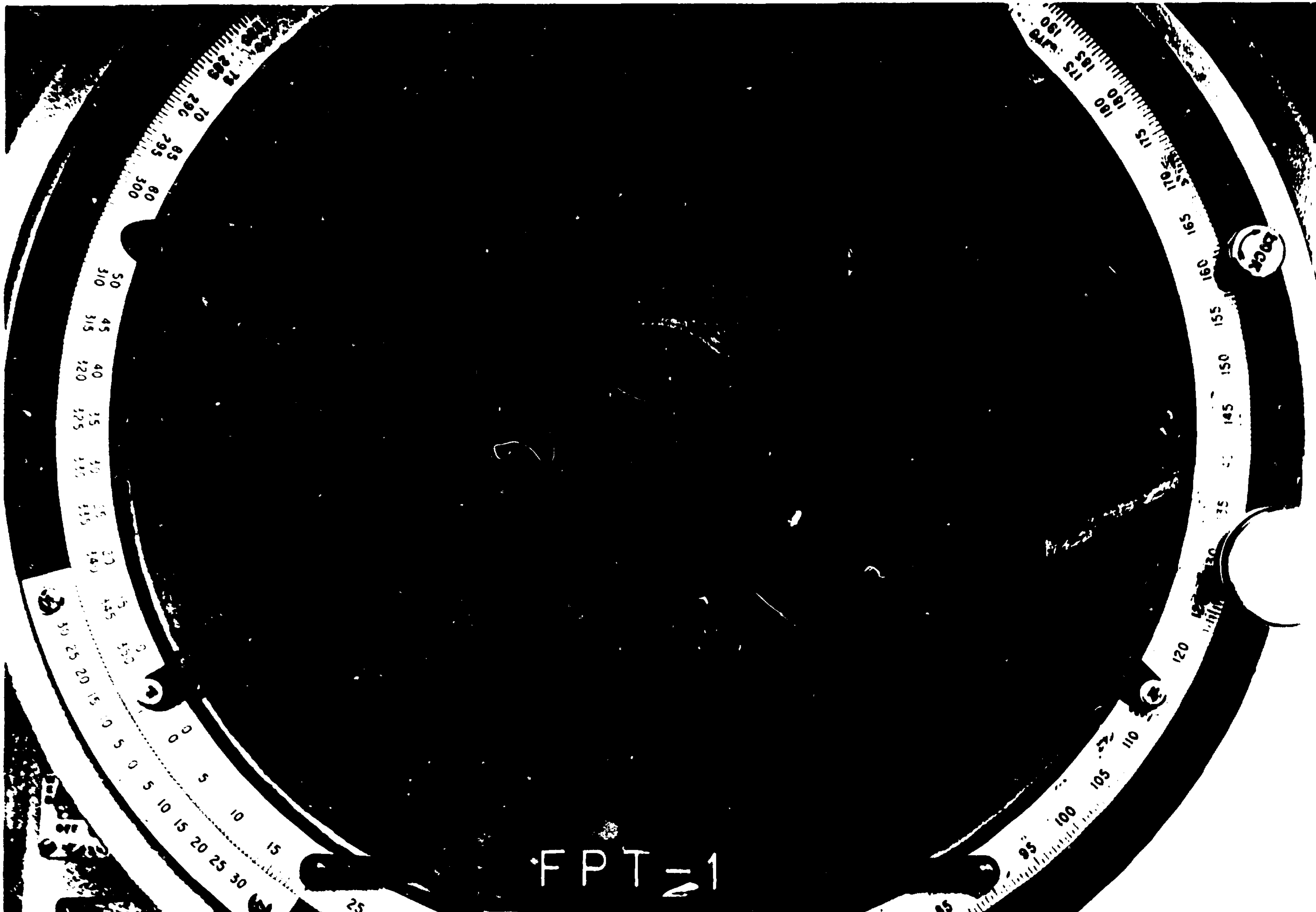

Fig. 64 (a-d). Shadowgraphs of the axial flaws machined in the thin-walled pressurized pipe specimens.

ORNL PHOTO 8163-89

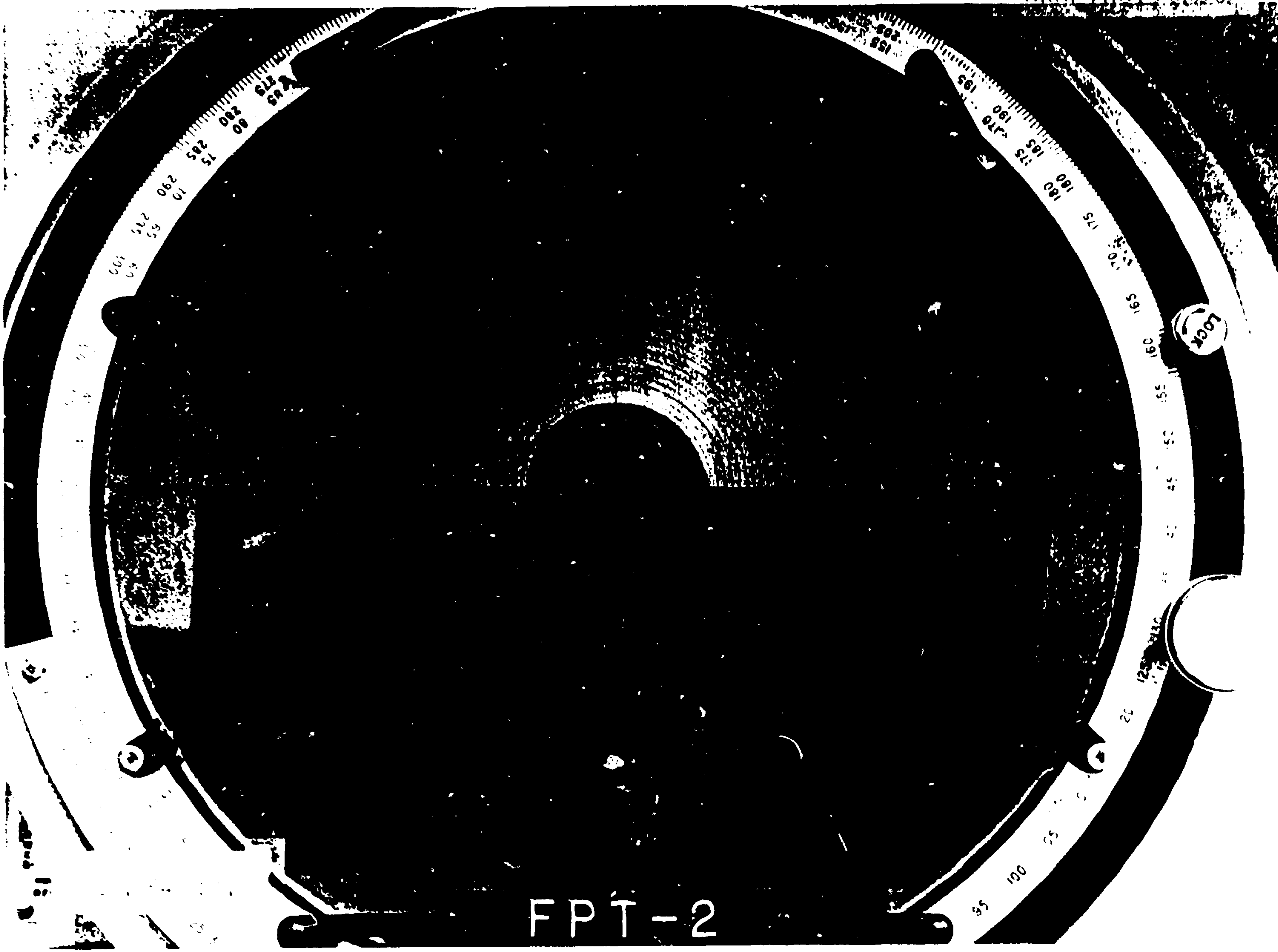

ORNL PHOTO 5164-89

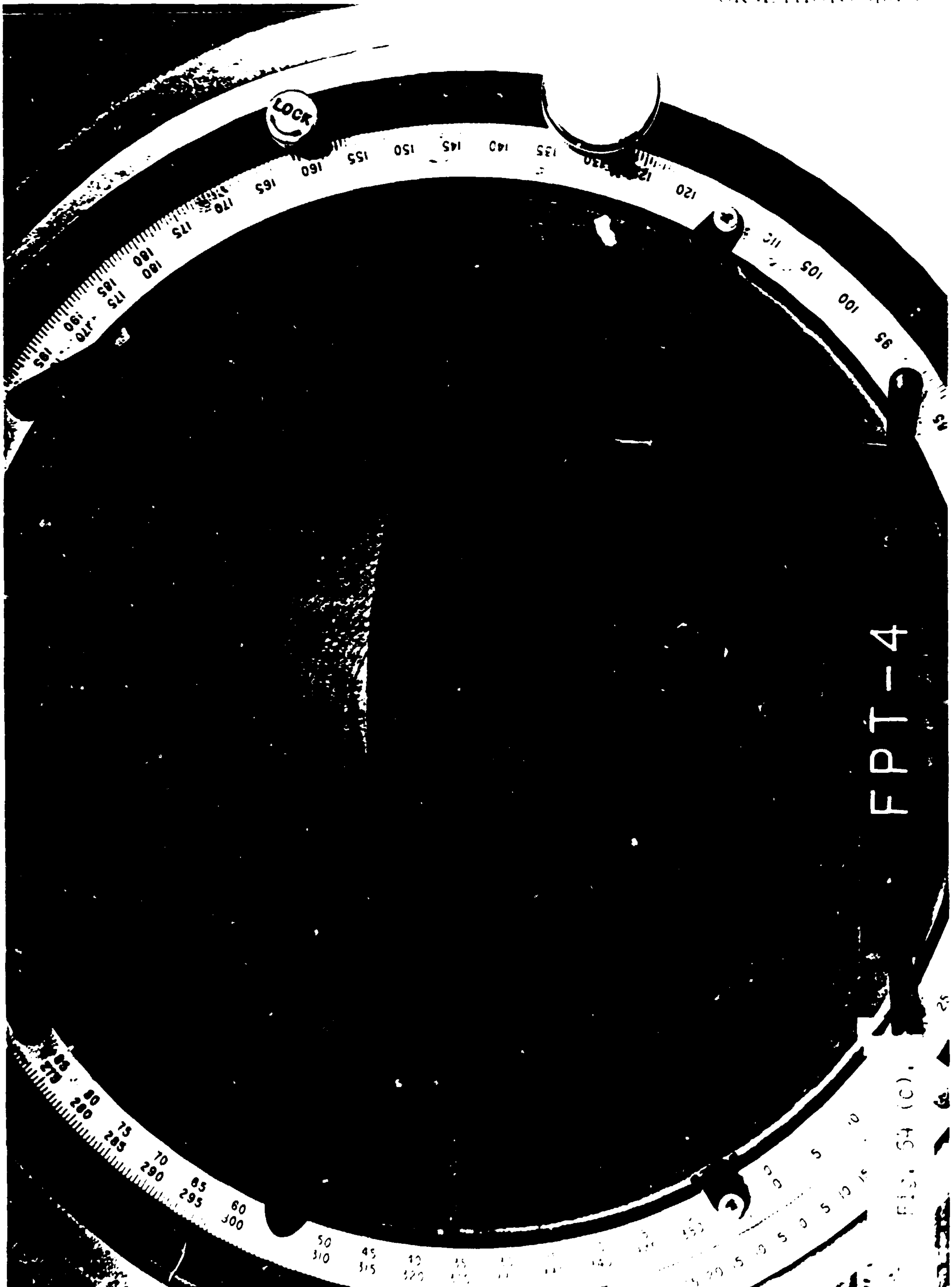

FIG. 54 (C).

ORNL PHOTO

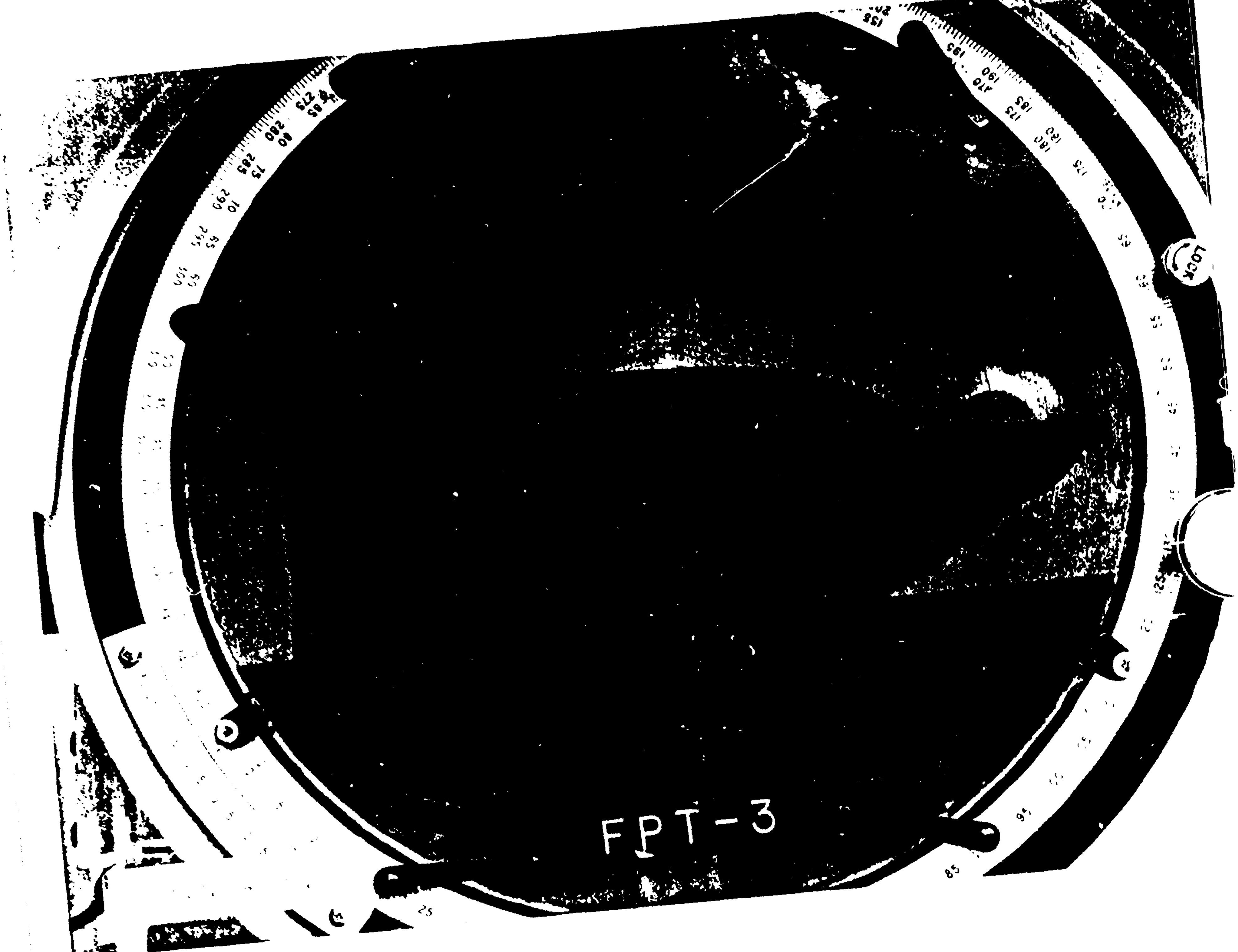

ORNL PHOTO 8157-89

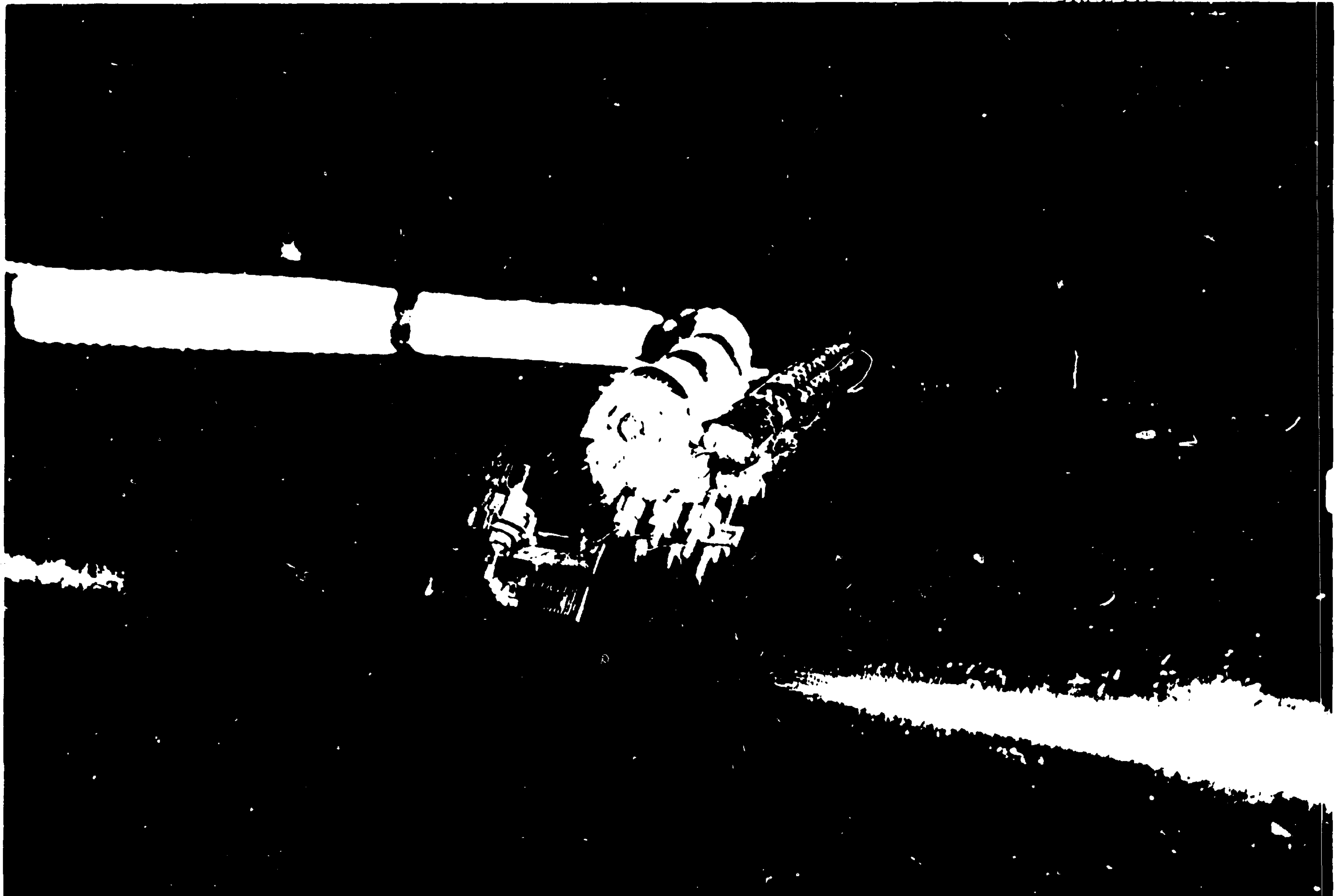

Fig. 65. Detail of the pressurized pipe specimen instrumented with the capacitance strain gage at the flaw.

ORNL-DWG 89-15030

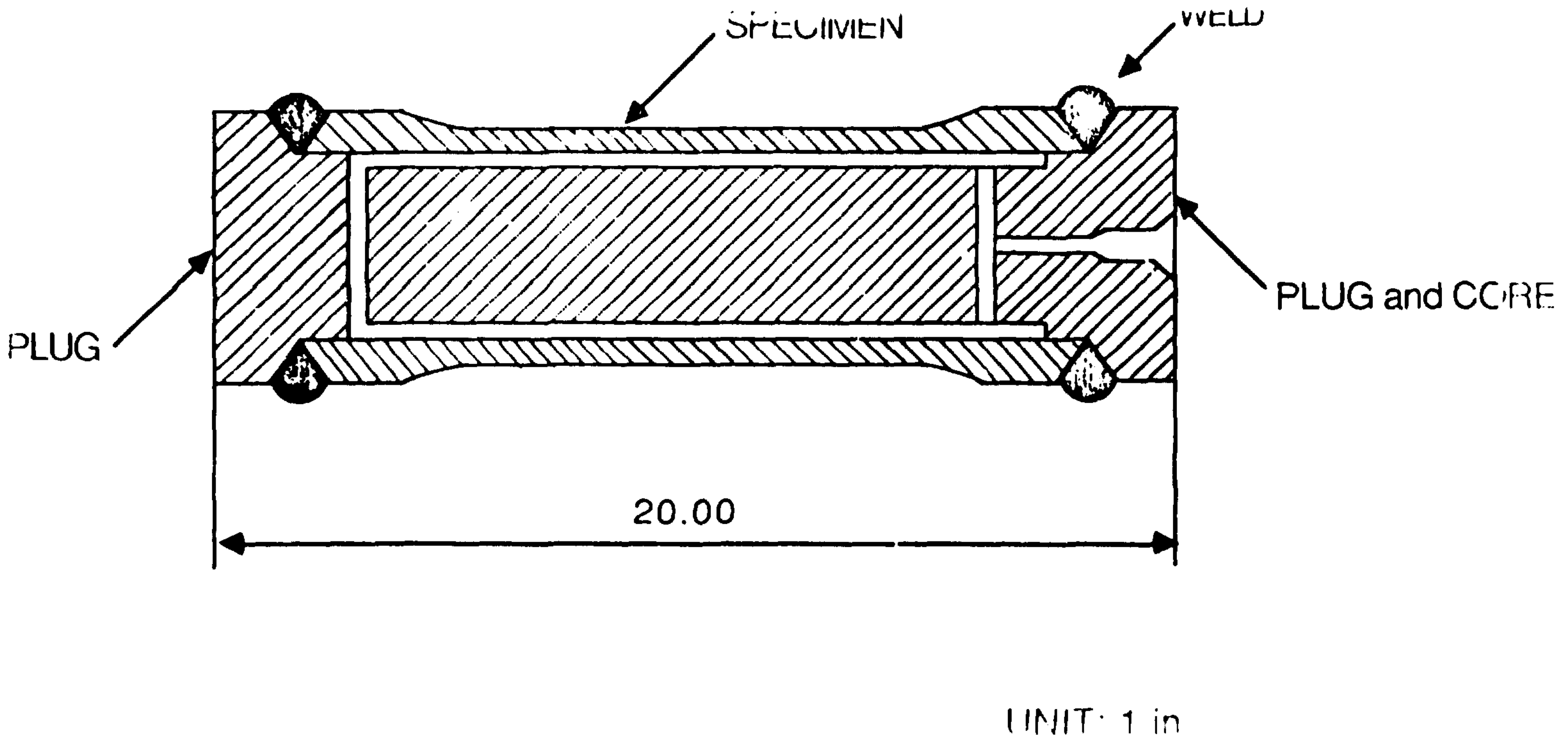

Fig. 66. Schematic of the thin-walled pressurized pipe specimen with the filler plug and core.

ORNL PHOTO 8159-89

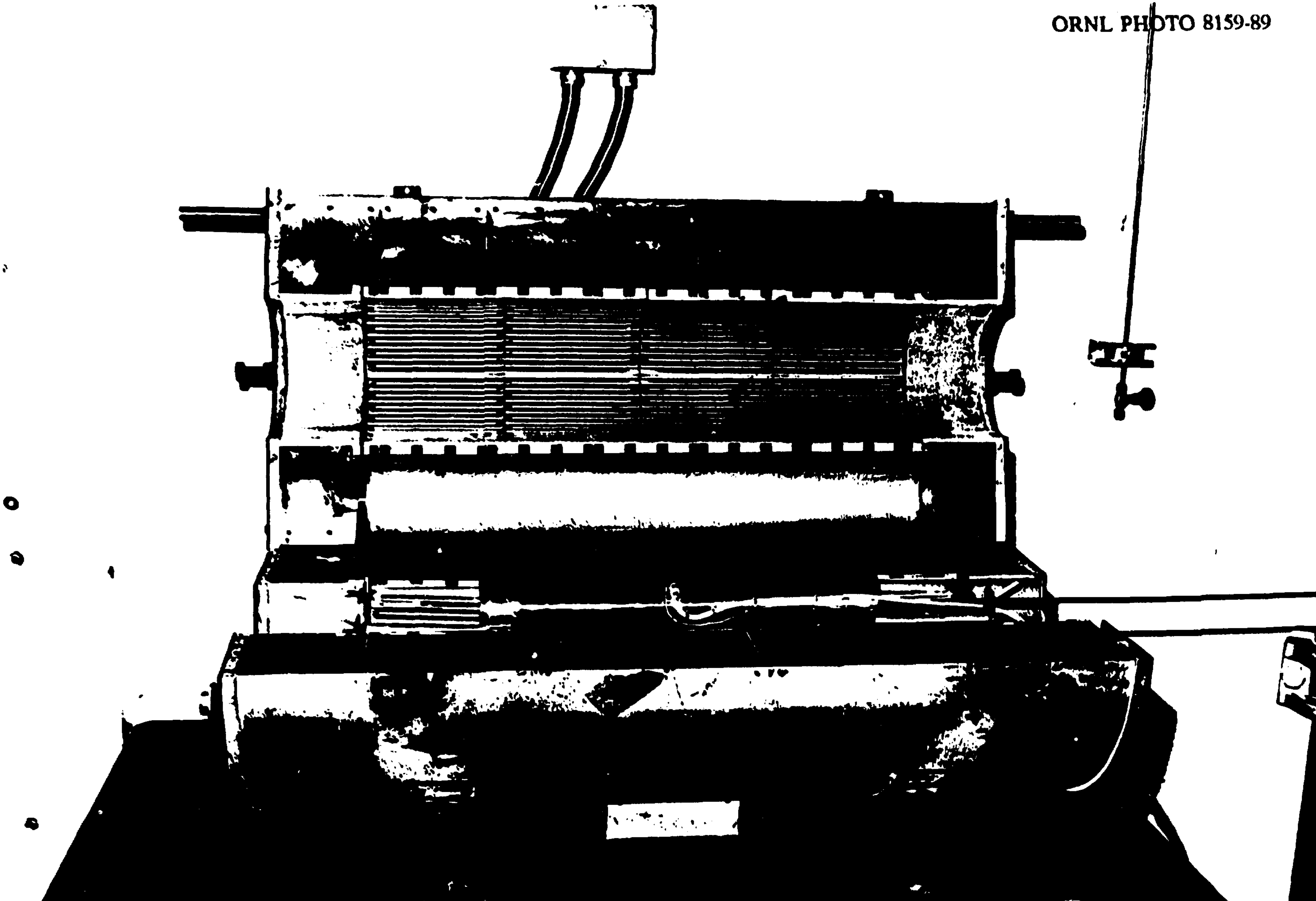

Fig. 67. Furnace used in exploratory tests on thin-walled preflawed pressurized pipes.

ORNL PHOTO 8090-82

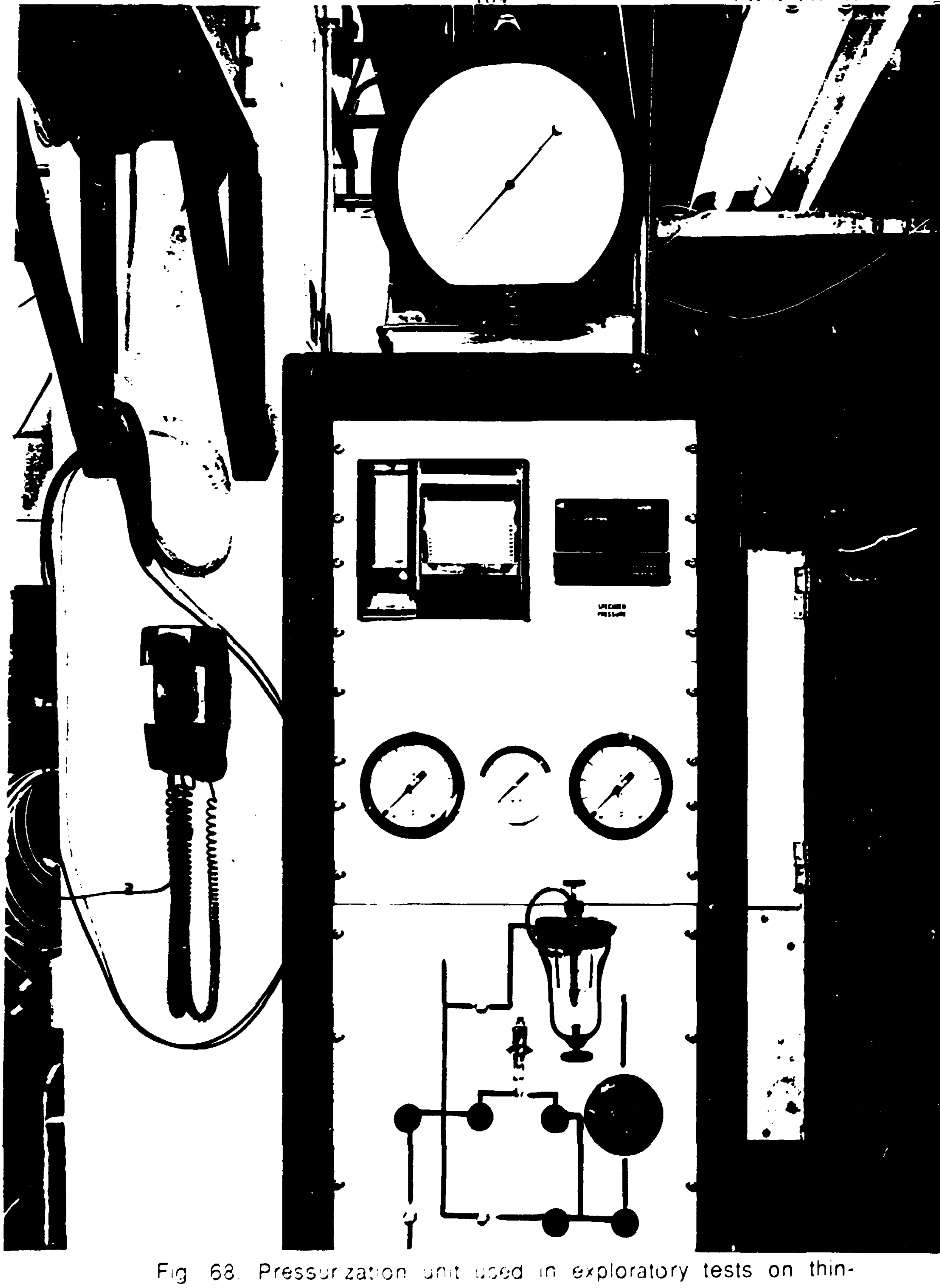

Fig. 68. Pressurization unit used in exploratory tests on thin-walled preflawed pressurized pipes.

ORNL-DWG 89-15031

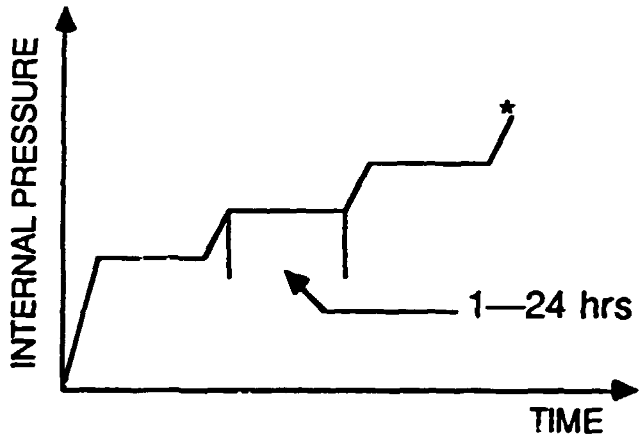

MAXIMUM HOLD TIME = 24 hrs

MAXIMUM INTERNAL PRESSURE = 18 MPa

Fig. 69. Stepwise internal pressure loading.

ORNL-DWG 89-15032

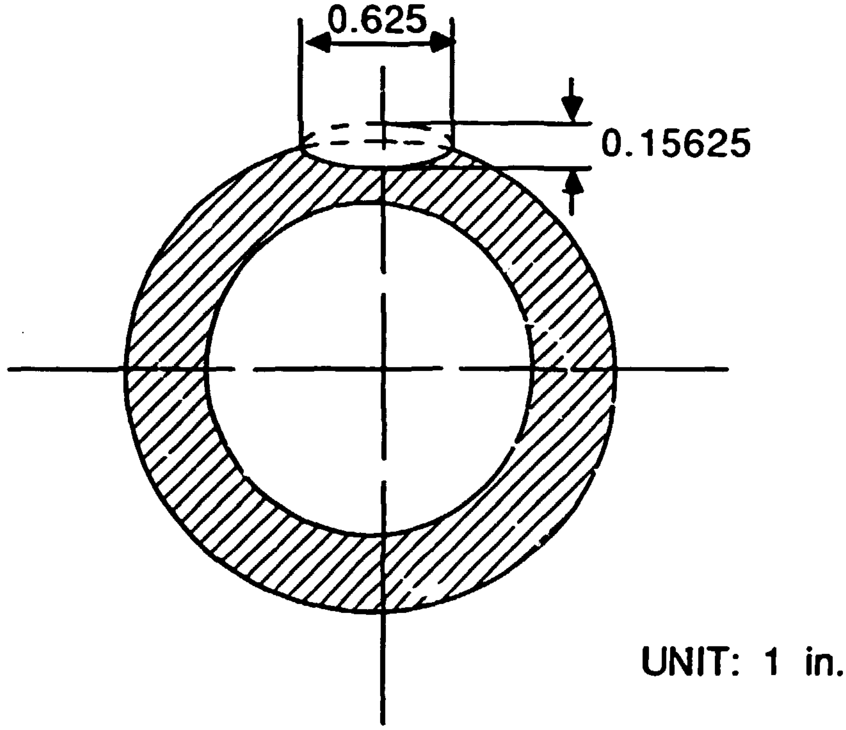

FLAW GEOMETRY

Fig. 70. Schematic of a circumferential flaw used for thin-walled thermal shock specimens.

Internal Distribution

1. R. L. Battiste
2. J. J. Blass
3. C. R. Brinkman
4. S.-J. Chang
5. R. D. Cheverton
6. J. A. Clinard
7-11. J. M. Corum
12. R. C. Gwaltney
13. W. R. Hendrich
14. F. J. Homan
15. R. L. Huddleston
16. J. E. Jones Jr.
17. W. F. Jones
18. W. J. McAfee
19. J. G. Merkle
20. D. G. O'Connor
21. C. R. Richmond
22. P. L. Rittenhouse
23-32. M. B. Ruggles
33. W. K. Sartory
34. G. M. Slaughter
35. G. T. Yahr
36. ORNL Patent Section
37. Central Research Library
38. Document Reference Section
39. Laboratory Records (RC)

External Distribution

40. Office of Assistant Manager for Energy Research and Development, U.S. Department of Energy, ORO, P. O. Box 2001, Oak Ridge, TN 37831
41-42. Office of Scientific and Technical Information, DOE, P. O. Box 62, Oak Ridge, TN 37831
43. C. C. Bigelow, Division of Advanced Technology Development, NE-462, U.S. Department of Energy, Washington, DC 20545
44. M. Gabler, Rocketdyne Division, Rockwell International, 6633 Canoga Avenue, Canoga Park, CA 91303
45. E. L. Gluekler, General Electric Company, Advanced Nuclear Technology, 6835 Via Del Oro/Box 530954, San Jose, CA 95153-5354
46. D. S. Griffin, Westinghouse Electric Corp., Advanced Energy Systems Division, P. O Box 10864, Pittsburgh, PA 15236
47. K. R. Jaquay, Rocketdyne Division, Rockwell International, 6633 Canoga Avenue, Canoga Park, CA 91303
48. R. I. Jetter, Energy Technology Engineering Center, P. O. Box 1449, Canoga Park, CA 91304
49-68. E. Rodwell, Electric Power Research Institute, 3412 Hillview Avenue, P. O. Box 10412, Palo Alto, CA 94303
69. G. Santos-Leon, Energy Programs Division, U.S. Department of Energy, ORO, P. O. Box 2001, Oak Ridge, TN 37831
70. A. Van Echo, Division of Advanced Technology Development, NE-462, U.S. Department of Energy, Washington, DC 20545